Master's thesis

NTNU
Norwegian University of Science and Technology
Faculty of Information Technology and Electrical Engineering
Department of Electric Power Engineering

Kamilla Bakkane Folgerø

Networked Control of Complex Cyber-Physical DC Microgrids

On the Potential of Scalable Stability Features of PI Consensus Estimators

Master's thesis in Energy and Environmental Engineering
Supervisor: Gilbert Bergna-Diaz
June 2023

NTNU
Norwegian University of Science and Technology

Kamilla Bakkane Folgerø

Networked Control of Complex Cyber-Physical DC Microgrids

On the Potential of Scalable Stability Features of PI Consensus Estimators

Master's thesis in Energy and Environmental Engineering
Supervisor: Gilbert Bergna-Diaz
June 2023

Norwegian University of Science and Technology
Faculty of Information Technology and Electrical Engineering
Department of Electric Power Engineering

NTNU
Norwegian University of
Science and Technology

Preface

First of all, I would like to express my gratitude to my supervisor, Professor Gilbert Bergna-Diaz for his patience, insightful discussions and guidance throughout this year, enabling me to gain a deeper understanding of cyber-physical DC microgrids.

I would also like to thank Babak Abdolmaleki for his assistance in enhancing my understanding of the control aspects involved in this research.

Last but certainly not least, I would like to thank my friends and family for the support. My fellow students and friends have made this academic journey memorable and rewarding. I would also like to express my appreciation to the students at The Corner Office for helpful discussions on nonlinear theory, as well as providing a space filled with laughter and support throughout this year.

Abstract

This master's thesis continues the work carried out in the associated specialization project by further investigating a cyber-physical DC microgrid proposed in a research paper. The microgrid is controlled by a suitable controller, which was proposed in another research paper. The electrical network, referred to as the physical layer, consists of distributed generators, converters, transmission lines, capacitors, and constant impedance-current loads. Furthermore, the DC microgrid is challenging the traditional hierarchical network structure by having a distributed communication network called the cyber layer. The distributed generators have only access to their neighbor's data, which allows for distributed communication techniques and consensus optimization to provide the two control objectives of proportional current-sharing and voltage containment.

The control objective of voltage containment is achieved by using hyperbolic nonlinear saturation on the input voltage from the controller. Furthermore, the control objective of proportional current-sharing is achieved by introducing an optimization problem using consensus principles. Consequently, the optimization problem obtains an optimal set point for each generator via Karush-Kuhn-Tucker conditions. The set points of all generators are identical due to the consensus algorithm and the neighbor-to-neighbor communication. The optimization problem forms the Proportional-Integral Dynamic Consensus Estimators that can be implemented in the cyber layer as part of the controller. Furthermore, the distributed optimization problem also considers the second control objective of voltage containment, resulting in sub-optimal set points for the current ratios when the voltages are saturated to avoid integrator wind up. The controller also includes a regulator state responsible for minimizing the distance between the optimal set point and the current ratio. The controller is connected to a case-specific cyber-physical DC microgrid, and simulations are carried out to confirm that the controller satisfies the control objectives.

Moreover, we aim to obtain a *scalable stability certificate* for the cyber-physical DC microgrid. This allows for *plug-and-play* features such that the microgrid can expand without instability risks. *Large-signal stability* and *energy modeling* methods are utilized to obtain the stability certificate. Initially, it is demonstrated that both layers' open-loop systems admit to a port-Hamiltonian representation, and their respective passive outputs are determined, which serves as a beneficial starting point for energy control. However, in the attempt to connect the two layers, an important stumbling block appears that complicates the finding of scalable stability certificates. The thesis identifies that this issue occurs at the interface between the cyber layer and the regulator state. To reduce the system's complexity with the aim of investigating this issue further, voltage saturation is neglected in the energy modeling in this thesis.

Finally, we borrow some ideas from singular perturbation theory to justify using time-scale separation arguments as a potential solution to obtain a scalable stability certificate. This theory implies that the system is divided into fast and slow dynamics. Moreover, a modified controller is proposed based on this theory and the passive output of the cyber layer. In this proposal, the regulator state is considered the slow system, which behaves as a constant in the fast system and reduces the complexity of the equations. With this approach, energy analysis of the fast dynamics results in a stability certificate. However, to complete the stability proof using time-scale separation principles, the slow dynamics should also be analyzed, and only then could we conclude that the system will be robust to stability-related challenges under all circumstances. From a practical perspective, it is possible to disconnect the slow dynamics to maintain stable conditions in situations where unstable behavior begin to appear.

Sammendrag

Denne masteroppgaven bygger videre på arbeidet som ble utført i forbindelse med det tilhørende spesialiseringsprosjektet ved å fortsette på analysen av et cyber-fysisk DC mikronett som ble foreslått i en forskningsartikkel. Mikronettet blir kontrollert av en passende kontroller som ble foreslått i en annen forskingsartikkel. Det elektriske nettverket, som også kalles det fysiske laget, består av distribuerte generatorer, omformere, transmisjons linjer, kondensatorer og konstant-impedans-konstant-strøm laster. DC mikronettet har et kommunikasjonsnettverk, cyber laget, med en distribuert kommunikasjonsstruktur. Denne strukturen utfordrer den tradisjonelle hierarkiske strukturen som typisk brukes i strømnettet. De distribuerte generatorene har bare tilgang til naboens data, noe som legger til rette for distribuerte kommunikasjonsteknikker og en konsensusoptimalisering for å oppfylle de to kontrollmålene om spenningsbegrensning og proporsjonal strøm-fordeling.

Spenningsbegrensning oppnås ved å bruke en hyperbolisk ikke-lineær metningsfunksjon på inngangsspenningen fra kontrolleren. Videre oppnås proporsjonal strøm-fordeling ved å introduser et optimaliseringsproblem basert på konsensusprinsipper. Slik oppnår optimaliseringsproblemet en optimal referanseverdi for hver generator ved hjelp av Karush-Kuhn-Tucker-betingelsene. Referanseverdiene for alle generatorene blir identiske som følger av konsensusalgoritmen og nabo-til-nabo kommunikasjonen. Optimaliseringsproblemet danner de proporsjonale-integrale dynamisk konsensusestimatorene som kan implementeres i cyberlaget som en del av kontrolleren. Det distribuerte optimaliseringsproblemet tar også hensyn til det andre kontrollmålet om spenningsbegrensing, noe som resulterer i suboptimale referanseverdier for utnyttelsesgraden til strømmene når spenningene er mettet. Dermed kan man unngå integrator wind-up. Kontrolleren inkluderer også en regulator-tilstand som har i oppgave å minimere avstanden mellom den optimale referanseverdien og utnyttelsesgraden til strømmene. Kontrolleren kobles til et eksempelssystem, og simuleringer utføres for å bekrefte at kontrolleren oppfyller kontrollmålene.

Videre forsøker vi å oppnå et *skalerbart stabilitetssertifikat* for det cyber-fysiske DC mikronettet. Dette tillater *plug-and-play-funksjoner* slik at mikronettet kan utvides uten at det skal føre til ustabiliteter i nettet. Metoder innenfor stor-signal stabilitet og energi modellering brukes for å oppnå et slikt stabilitetssertifikat. Først vises det at det åpne sløyfesystemet for begge lagene kan representeres ved hjelp av en port-Hamiltonian systemrepresentasjon. Videre bestemmes deres respektive passive utgangsverdier, som er et gunstig startpunkt for energikontroll. Da vi forsøker å koble disse lagene sammen, oppstår det en utfordring som gjør det komplisert å oppnå et skalerbart stabilitetssetifikat. Dette problemet identifiseres ved grensesnittet mellom cyberlaget og regulator-tilstanden. Derfor tas det en beslutning om å neglisjere metningsfunksjonen i de videre analysene av problemet.

Til slutt benytter vi ideer fra teorien om systemer med singulære forstyrrelser, for å underbygge bruken av tidsskala-seperasjon som en mulig løsning for å oppnå et skalerbart stabilitetsertifikat. Denne teorien antyder at systemet kan deles inn i rask og langsom dynamikk. Videre foreslås en modifisert kontroller som baserer seg på denne teorien, i tillegg til de passive utgangsverdiene fra cyberlaget. Her betraktes regulator-tilstanden som det langsomme systemet, som oppfører seg som en konstant i forhold til det raske systemet. Dermed reduserers kompleksiteten i ligningene til det raske systemet. Med denne tilnærmingen oppnår vi et stabilitetssertifikat for den raske dynamikken. For å fullføre stabilitetsbeviset ved bruk av prinsippene om tidsskala-seperasjon, må også den langsomme dynamikken analyseres og tilfredsstille kravene til stabilitet. Først da kan vi konkludere at systemet vil være robust mot stabilitetsrelaterte utfordringer. Til slutt vektlegges det at fra et praktisk perspektiv er det mulig å koble fra den langsomme dynamikken når ustabil oppførsel begynner å oppstå, slik at man kan opprettholde stabile forhold.

Contents

List of Figures

List of Abbreviations

CbI	Control by Interconnection
CP	Cyber-Physical
DC	Direct-Current
DER	Distributed Energy Sources
KCL	Kirchhoff's Current Law
KKT	Karush-Kuhn-Tucker
KVL	Kirchhoff's Voltage Law
MG	Microgrid
PBC	Passivity-Based Controller
pH	port-Hamiltonian
PI	Proportional Integral
PnP	Plug-and-Play
ZI	Constant Impedance (Z), Constant Current (I)
ZIP	Constant Impedance (Z), Constant Current (I), Constant Power (P)

Chapter 1

Introduction

This master's thesis investigates a cyber-physical (CP) DC microgrid (MG) based on the electrical structure proposed by Babak Abdolmaleki and Gilbert Bergna-Diaz in their research work in *Distributed Control and Optimization of DC Microgrids: A Port-Hamiltonian Approach* [1]. The thesis also explores the implementation of a controller proposed by the same authors in *A Nonlinear Control Framework for Optimal Load-sharing and Voltage Containment in DC Networks* [2]. Moreover, this thesis builds upon the previous research conducted by Cornelia Skaga in her master's thesis [3], which examined the electrical network described in [1] managed by a different controller. Furthermore, this chapter aims to establishing the motivation, providing the foundation and outlining the objectives of the thesis.

1.1 Background and Motivation

1.1.1 The World Energy Outlook

The world outlook related to climate change is a crucial and current topic of discussion. It is of significant importance for world leaders and organizations, making it a high priority on the global agenda. According to [4], the percentage of CO_2 in the atmosphere is 50% higher than the pre-industrial levels. The source also states that the burning of fossil fuels is the primary driver of the increase in the atmospheric level of CO_2. The combustion of carbon that has previously been stored in coal and gas contributes to these increasing levels. The increased emission of greenhouse gases into the atmosphere gradually contributes to global warming, meaning that today's emissions will have consequences for the future if not limited [5]. As we know, climate changes have significant consequences of increased temperature, rising sea levels, species extinction, more diseases, forced migration of people, and numerous others. Climate change is affecting everyone on the planet and is happening at this moment. For this reason, the world is in desperate need of collaboration between nations to set and achieve optimistic yet attainable goals.

In 2015, the Paris Agreement was adopted at United Nations (UN) Climate Change Conference, an international treaty on climate change. The goal of the agreement is to *"hold the increase in the global average temperature to well below* $2°C$ *above pre-industrial levels"* and to pursue efforts *"to limit the temperature increase to* $1.5°C$ *above pre-industrial levels"* [6]. Through the Paris Agreement, countries are obliged to do their best to reduce their emission and strengthen their effort every year [7]. Every sector must contribute for countries to achieve these vital goals. According to the International Energy Agency (IEA), the energy sector accounts for more than

two-thirds of the total greenhouse gas emission globally, where fossil fuels represent 80% of the total energy supply globally [8]. In other words, the energy sector has to enhance its effort to transition from fossil fuels to renewable energy sources and contribute to novel net zero solutions. In fact, to become net zero by 2050, almost 90% of the global electricity generation in 2050 has to come from renewable sources, primarily wind and solar [9].

1.1.2 DC Microgrid

The demand for renewable energy sources in a limited amount of time leads to exploring new alternatives. In particular, microgrids facilitate the shift towards renewable distributed energy resources (DERs), which are typically small in scale and located at short distances from the loads [10]. IEEE defines a microgrid as *"a group of interconnected loads and distributed energy resources with clearly defined electrical boundaries. It acts as a single controllable entity with respect to the grid and can connect and disconnect from the grid to enable it to operate in both grid-connected or island modes"* [11]. Incorporating DERs in microgrids reduces the pressure of expanding the traditional power grids, which comes with expenses related to construction and maintenance. Additionally, a microgrid is designed to incorporate variable energy sources, such as solar and wind, and efficiently manage the balance between generation and loads locally. This approach significantly mitigates the stability challenges associated with the large-scale integration of renewable energy sources into the main grid [12]. Moreover, a microgrid can operate isolated from the grid and provide electricity in remote areas, making energy available for developing countries that lack infrastructure.

Historically, the electric power system has been based on AC technology schemes. The AC technology has been favored because the transformation of voltage levels has been easier, and it has been well suited for the generators used in hydropower and fossil fuel power [13]. However, new research in power electronics and modern technologies has recently challenged the traditional approach. DC technology has especially been considered in microgrids, and there are several reasons to use DC rather than AC in these applications. Since most DERs produce DC power and energy storage devices are DC in nature, fewer converters are necessary for DC grids, which reduces the system size and footprint. Additionally, losses and costs are reduced. DC microgrids are also simpler to control, as they do not require frequency and reactive power control. According to [13], these properties beat AC. However, DC microgrids need more system standardizations such that it is harder to implement these applications. If academia and industry collaborate, it will allow for faster standardization of components and expansion of the DC microgrids.

1.1.3 Breaking the Hierarchy with a Distributed Control Structure

DC microgrids that have control methods based on the plug-and-play concept used in the computer industry have a better chance of success, according to [14]. The plug-and-play (PnP) concept allows for almost immediate connection and seamless integration of new energy sources. However, the traditional hierarchical structure of the power grid has poor PnP capability [15]. The investigation of other methods has given promising results in using the distributed control structure [16]. By adopting this control structure, the DC MG mitigates the risk of system failure since it neglects the single central unit that controls the system. Additionally, this control structure is advantageous in terms of cyber-security [17]. According to [17], the distributed control structure is preferred over the decentralized structure since this structure struggles to provide optimal operation. The traditional centralized control structure has three levels of control that operate at different time scales; the primary, secondary, and tertiary level of control. The primary control is responsible for the load

sharing between the DGs, typically by implementing a droop controller. On the other hand, secondary control regulates voltage fluctuation, and tertiary control manages the power flow within the grid [15]. Microgrids with renewable sources have less rotating inertia compared to traditional power grids. Consequently, the primary control needs to be fast and reliable [18]. A distributed control structure is typically based on consensus algorithms to reach the objectives, which breaks this traditional hierarchy by merging the levels of control and provides a fast response to power changes [19]. The consensus-based method finds a globally optimal solution using information from the neighborhood [17]. This master's thesis utilizes such an approach in the cyber-physical MG.

In MGs with a distributed control structure, proportional current-sharing has been in focus to replace the traditional communication-free droop control. Furthermore, the droop control can result in unbalanced output power since it does not provide a proportional sharing of current between the DGs in the MG and is less reliable [15]. The proportional current-sharing, provided by a distributed control structure, resolves this issue, implying that each source provides a share according to the capacity of its converter [20]. The converters with the highest rating provide the most current, such that the total current being generated is proportionally allocated between the different energy sources. According to [2], it is crucial to keep the generator voltages within operational limits in voltage-sensitive applications. However, [21] argues that achieving proportional current-sharing and proper voltage regulation simultaneously has proven to be challenging. This is because the currents and voltages are tightly related. In the controller utilized in this master's thesis, voltage containment is prioritized before accurate proportional current-sharing. In contrast to [3], this thesis investigates a controller that ensures that all generators stay within their operational limits, which differs from the average voltage regulation, which only maintains the average voltage of the entire network [2].

1.1.4 Stability Analysis

Stability requirements have a crucial role in DC microgrids because of the limited inertia in converter-based grids. Consequently, stability analysis takes up a significant portion of this thesis. The literature presents two types of stability analysis: small signal and large signal stability analysis. Small signal stability is a simplified approach that involves linearization around the system's operating point [22]. On the other hand, large signal stability analysis considers nonlinear systems, but is also applicable to linear systems. Lyapunov's stability criteria are widely used to determine the stability conditions of nonlinear systems. This stability analysis requires a Lyapunov candidate to validate the stability conditions. Although there is no standardized method for obtaining a Lyapunov candidate, using the natural port-Hamiltonian representation to obtain a shifted Hamiltonian function serves as an efficient starting point that may yield global asymptotic stability. If a system is proved to be globally asymptotic stable, the system qualifies for a *stability certificate*, which facilitates the PnP approach. Furthermore, the port-Hamiltonian representation of a system exhibits passivity properties strongly connected to the system's stability conditions and can be used in the design of passivity-based controllers [23]. The port-Hamiltonian method of designing controllers uses information on connections and energy as tools to design a controller.

1.2 Scope and Objectives

The primary objective of this master's thesis is to provide an understanding of complex control concepts, emphasizing port-Hamiltonian systems and energy analysis. This objective will be achieved by examining the DC MG presented in Babak Abdolmaleki's and Gilbert Bergna-Diaz's research work in [1], incorporated with a controller proposed by the same authors in [2]. Through an extensive study of this system, the thesis fulfills its first objective as formulated below.

Thesis Objective 1: *Provide a clear and accessible explanation of complex control concepts while demonstrating their application on the cyber-physical DC microgrid of study.*

A formal stability proof has yet to be published for a DC MG incorporating this specific controller proposed in [2]. However, the associated specialization project [24] emphasized challenges in the structure of the cyber-physical DC MG, but the cause remains unresolved. The thesis uses energy analysis and the port-Hamiltonian framework to identify these challenges. Hence, the second objective of this thesis is formulated as below.

Thesis Objective 2: *Investigate and identify the challenges of obtaining a stability certificate when implementing the controller proposed in [2] to the DC MG presented in [1].*

As a final step, the thesis seeks to obtain a stability certificate for the combined network by using time-scale separation principles to modify the controller. Accordingly, the third objective of the master's thesis is formulated below.

Thesis Objective 3: *Modify the controller proposed in [2] to achieve a stability certificate while ensuring the control objective of proportional current-sharing.*

1.2.1 Limitation of Scope

The thesis simplifies the structure of the electrical network in the DC MG proposed in [1] by considering zero-order converters with no inherent dynamics, enabling the implementation of a desired converter in future work. Additionally, the constant-impedance-current-power loads (ZIP) that result in a nonlinear behavior and create stability challenges are replaced by ZI loads to maintain system linearity.

The thesis addresses the complex structure of the proposed controller and identifies the challenges in obtaining a port-Hamiltonian representation of the interconnected system. Consequently, a decision to linearize the controller is made to reduce the system's complexity until the port-Hamiltonian representation of the complex system is obtained. The nonlinearity of the system is removed by neglecting the hyperbolic tangent saturation, which can be reintroduced in future work. Therefore, the nonlinear analysis of the system is a starting point for future studies.

The proposal of the modified controller employs time-scale separation principles to obtain a stability certificate. However, this approach only considers the system's fast dynamics, leaving out an analysis of the slow dynamics by arguing that the slow dynamics can be disconnected in case of the appearance of unstable behavior. Consequently, a robust stability certificate for the system under all circumstances cannot be conclusively established. However, further research could explore the study of the slow dynamics to potentially obtain such a certificate.

Energy modeling, stability analysis, and control objectives have been the primary focus of this thesis. Consequently, the transient control performance is not considered in this thesis. Lastly, the simulation results only depict the system states that are important regarding the control objectives,

leaving out the plots of the transmission line current, load voltages, and the cyber states.

1.3 Thesis Overview

The master's thesis does not follow the standard report structure but instead investigates one topic at a time before moving on to the next one. This approach intends to enhance the understanding of readers who are new to the theory and the complex topics being discussed. The master's thesis builds upon the associated specialization project, which also contains different themes. However, the master's thesis takes each theme a step further. Consequently, the thesis allows for chapters to contain both preliminary information and a new contribution. Furthermore, a paragraph is incorporated at the beginning of each chapter to provide clarity to the reader and distinguish between reproduced information and a new contributions. This paragraph is written in *italic* font and identifies the information reproduced from the associated specialization project.

The remainder of this thesis is organized as follows:

Chapter 1: Introduction: provides an overview of research topics relevant to the cyber-physical DC MG as well as outlining the thesis' objectives.

Chapter 2: Introducing the Cyber-Physical DC Microgrid: introduces the cyber-physical DC microgrid proposed in [1] and provides preliminary theory regarding the structure.

Chapter 3: The Controller: provides a thorough investigation and explanation of the controller proposed in [2].

Chapter 4: Energy Modeling and Analysis: introduces and utilizes advanced energy modeling and stability techniques in the cyber-physical DC MG. Additionally, challenges in the complex structure are identified.

Chapter 5: Proposing a Modified Controller with a Stability Certificate: seeks to obtain a stability certificate for a modified version of the controller proposed in [2].

Chapter 6: Conclusion and Further Work: concludes the thesis and suggests future work.

Appendices: includes supporting materials obtained in the associated specialization project.

Chapter 2

Introducing the Cyber-Physical DC Microgrid

A cyber-physical MG divides into two layers: the physical layer and the cyber layer. The physical layer is the electrical network that includes renewable power sources, converters, transmission lines, and loads. In other words, this is the visible and physical layer responsible for the power flow and the transport of energy. On the other hand, the cyber layer is a digital layer responsible for control and communication between the units in the physical layer. Together, these two layers constitute the cyber-physical microgrid. This chapter aims to describe the structure and mathematical foundations behind the physical and cyber layers. Furthermore, the case-specific DC MG that is used for learning purposes throughout this master's thesis will be introduced in this chapter.

In other words, this chapter aims to describe the preliminary concepts essential to understanding the challenges later emphasized in this master's thesis. As the theory below serves as the foundation for understanding complex concepts discussed later, the information is restated from the associated specialization project [24].

2.1 The Electrical Network

Studying the physical layer before introducing the cyber layer is intuitive, as the physical layer consists of familiar electrical terminologies such as generators, loads, and transmission lines. Therefore, the topic of this section will be to study the structure of the electrical network used in the analysis of this master's thesis.

The structure of the electrical network is based on Abdolmaleki's publication [1]. As explained in the associated specialization project [24], the article studied the control of a DC MG with ZIP loads and presented the structure of a general DC MG. The impedance, G_k^{cte}, current, I_k^{cte}, and power, P_k^{cte}, of the ZIP load at each bus were stated to be constant in this publication [1]. However, in Skaga's master's thesis [3], it was concluded that only the conductance and current of the loads should be kept constant to avoid complications and stability challenges caused by a constant power load. The relationship between a constant power load and a time-varying state variable, i.e., $P_k^{\text{cte}}/V_k^{\mathcal{N}}$, results in a non-linear behavior. In order to avoid this issue, Skaga adjusted Abdolmaleki's network by replacing ZIP loads with ZI loads, preserving the system's linearity. For convenience, this same approach will be adopted in this master's thesis.

Typically, DGs need a converter as an interface to be connected to a bus in a distributed DC MG [25]. In this master's thesis, grid-forming converters will be used to model the DC MG, i.e., voltage-controlled converters, following a given voltage reference [1]. Furthermore, these converters will be modeled as zero-order converters, such that the analysis applies to any other linear converter, *mutatis mutandis*. This also implies that there are no additional internal controller dynamics in the converter, such that the output voltage of the converter can be approximated to a desired reference.

The schematic representation of the DC MG examined in this master's thesis is given in Figure 2.1. The DC MG is almost identical to the DC MG presented in Skaga's master's thesis [3], except for the controller, which has been redesigned to achieve voltage containment. The controller will be explained in further detail in a subsequent chapter. In order to maintain coherence with the material presented in Skaga's master's thesis, notations for quantities and properties will be carried on in this manuscript as well.

Figure 2.1 illustrates a DG and a ZI load at a bus that connects to the rest of the DC MG through a transmission line. The resistance, inductance, and current of the DG at the studied bus in Figure 2.1 are represented by $R_i^{\mathcal{G}}$, $L_i^{\mathcal{G}}$, and $I_i^{\mathcal{G}}$, respectively. The generator voltage, $V_i^{\mathcal{G}}$, is controlled by the variable $u_{i,p}$. This control variable is unknown until the physical network is connected to the distributed communication network in a later section. Furthermore, G_k^{cte} and I_k^L are the constant conductance and current of the ZI-load at the studied bus. While $C_k^{\mathcal{N}}$ and $V_k^{\mathcal{N}}$ represent the capacitor in parallel with the load and the voltage across it, respectively. $R_j^{\mathcal{E}}$, $L_j^{\mathcal{E}}$, and $I_j^{\mathcal{E}}$ are the resistance, inductance and the current of the transmission line that connects the bus to the rest of the DC MG. In the illustration, only one transmission line is connected to the bus of study. However, a bus can have several connections. The rest of the DC MG is illustrated as a *black box*, where the topology in Figure 2.1 applies for each bus.

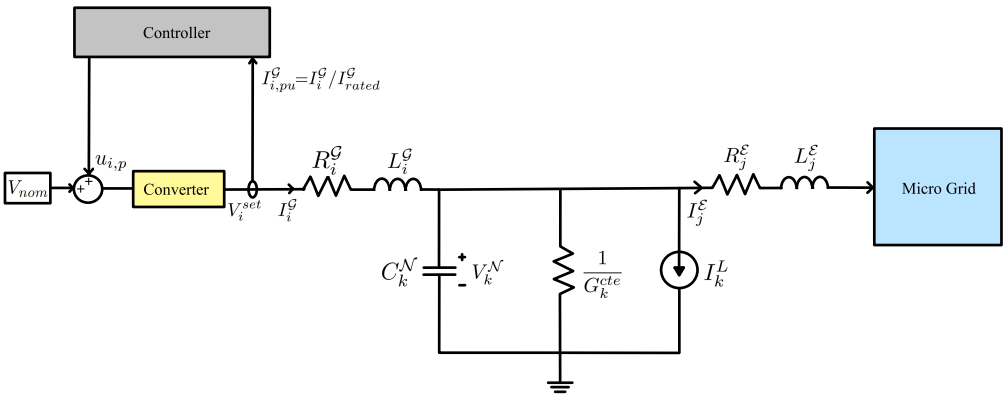

Figure 2.1: Structure of the DC microgrid.

The next step is to introduce graph theory as a method to describe the connections of the DC MG in a general manner. Graph theory is often combined with control theory and streamlines the stability analysis [26]. Furthermore, graph theory is also used in designing the controller for the distributed MG in [2]. Therefore, it is crucial to implement graph theory in the physical layer so it is possible to connect the layers and obtain a model of the entire DC MG.

As in [1] and Skaga's master's thesis [3], two graphs are established to describe the physical DC MG. A graph contains sets of nodes and edges, where an edge connects two nodes. An incidence matrix describes the connections between the nodes and edges. The dimensions of the incidence matrix are as follows: the number of rows is equal to the number of nodes, and the number of

columns is equal to the number of edges [27]. If a connection exists between a node and an edge, the corresponding element of the incidence matrix will be either 1 or -1. If the flow on an edge enters a node, the corresponding element for this pair in the incidence matrix is 1. If the flow on an edge leaves the node, the element in the incidence matrix is -1. If there is no connection between an edge and a node, the element is set to 0.

In the case-specific DC MG *Graph 1* was defined as $\mathcal{M}^{\mathcal{G}} = (\mathcal{N}_k, \mathcal{G}_i, \boldsymbol{\mathcal{B}}^{\mathcal{G}})$ in Skaga's master's thesis [3]. In this case, $\mathcal{N}_k$ is the set of nodes representing the loads, and $\mathcal{G}_i$ is the set of edges representing the generators and their edges. Thus, $k = \{1, ..., n^{\mathcal{N}_k}\}$ and $i = \{1, ..., n^{\mathcal{G}_i}\}$, where $n^{\mathcal{N}_k} = 4$ and $n^{\mathcal{G}_i} = 4$, which are equal to the number of loads and generators in the case-specific MG, respectively. The incidence matrix $\boldsymbol{\mathcal{B}}^{\mathcal{G}} \in \mathbb{R}^{n^{\mathcal{N}_k} \times n^{\mathcal{G}_i}}$ with elements, $b^{\mathcal{G}}_{ki}$, can be found by applying the above definition. As shown in Figure 2.2, the flow is from the generator edges to the load, as the generators are assumed only to inject and not absorb power in [1]. Consequently, the incidence matrix of *Graph 1* consists of only positive elements. By adopting the structure from [1] as in Figure 2.1, the generator edges are connected to only one load each. The incidence matrix of *Graph 1* is constructed based on the structure from Figure 2.2 and presented below.

$$\boldsymbol{\mathcal{B}}^{\mathcal{G}} = \begin{bmatrix} 1 & 0 & 0 & 0 \\ 0 & 1 & 0 & 0 \\ 0 & 0 & 1 & 0 \\ 0 & 0 & 0 & 1 \end{bmatrix} \tag{2.1.1}$$

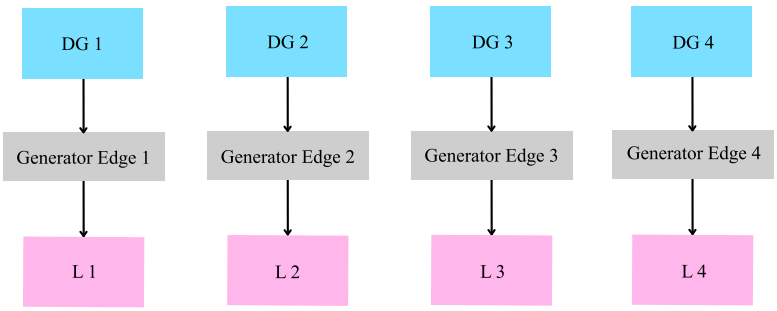

Figure 2.2: Graph 1.

Graph 2 was defined as $\mathcal{M}^{\mathcal{E}} = (\mathcal{N}_k, \mathcal{E}_j, \boldsymbol{\mathcal{B}}^{\mathcal{E}})$ in Skaga's master's thesis [3]. The set of loads, $\mathcal{N}_k$, is as defined above, representing the nodes of *Graph 2*. The set of edges, $\mathcal{E}_j$, in the graph are defined as the transmission lines. Thus, $j = \{1, ..., n^{\mathcal{E}_j}\}$, where $n^{\mathcal{E}_j} = 5$, which is equal to the number of transmission lines in the case-specific MG. The direction of flow between the loads is not defined, and the corresponding incidence matrix, $\boldsymbol{\mathcal{B}}^{\mathcal{E}} \in \mathbb{R}^{n^{\mathcal{N}_k} \times n^{\mathcal{E}_j}}$ with elements, $b^{\mathcal{E}}_{kj}$, is undirected. However, in Abdolmaleki's [1], it was decided to establish an arbitrary flow direction to obtain the incidence matrix. The incidence matrix of *Graph 2* from Skaga's master's thesis is constructed based on the structure from Figure 2.3 and reproduced below.

$$\boldsymbol{\mathcal{B}}^{\mathcal{E}} = \begin{bmatrix} -1 & 0 & 0 & -1 & 1 \\ 1 & -1 & 0 & 0 & 0 \\ 0 & 1 & 1 & 0 & -1 \\ 0 & 0 & -1 & 1 & 0 \end{bmatrix} \tag{2.1.2}$$

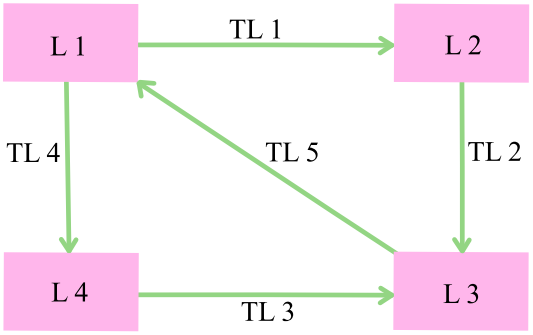

Figure 2.3: Graph 2.

Furthermore, it is possible to use the graph representation of the DC MG, combined with principles from Kirchhoff's Voltage Law (KVL) and Kirchhoff's Current Law (KCL), to analyze and understand the dynamics of the MG. The incidence matrices of each graph are used in the equations describing the DC MG below in (2.1.3), as presented in [1] and [3]. This way, the equations interconnect the three subsystems consisting of generators, loads, and transmission lines. The ordinary differential equations (ODEs) in (2.1.3) are general, meaning they can be applied to the case-specific DC MG and an arbitrary DC MG with a different number of DGs and interconnections. This is because we aim to model a CP MG and a controller that guarantees a plug-and-play design, as explained in the introduction in chapter 1.

$$L_i^{\mathcal{G}} \dot{I}_i^{\mathcal{G}} = V_i^{\mathcal{G}} - \sum_k b_{ki}^{\mathcal{G}} V_k^{\mathcal{N}} - R_i^{\mathcal{G}} I_i^{\mathcal{G}} \tag{2.1.3a}$$

$$L_j^{\mathcal{E}} \dot{I}_j^{\mathcal{E}} = -\sum_k b_{kj}^{\mathcal{E}} V_k^{\mathcal{N}} - R_j^{\mathcal{E}} I_j^{\mathcal{E}} \tag{2.1.3b}$$

$$C_k^{\mathcal{N}} \dot{V}_k^{\mathcal{N}} = \sum_j b_{kj}^{\mathcal{E}} I_j^{\mathcal{E}} + \sum_i b_{ki}^{\mathcal{G}} I_i^{\mathcal{G}} - I_k^L \tag{2.1.3c}$$

$$I_k^L = G_k^{cte} V_k^{\mathcal{N}} + I_k^{cte} \tag{2.1.3d}$$

$$V_i^{\mathcal{G}} = V_i^{\text{set}} = V_{\text{nom}} + u_{i,p} \tag{2.1.3e}$$

2.2 The Distributed Control Network

The physical network presented above will be connected to a distributed control network, i.e., the cyber layer, to provide communication in a distributed manner. Figure 2.4 shows the cyber layer for the case-specific CP MG. In this layer, data is exchanged solely between neighboring nodes through communication links following a distributed system topology.

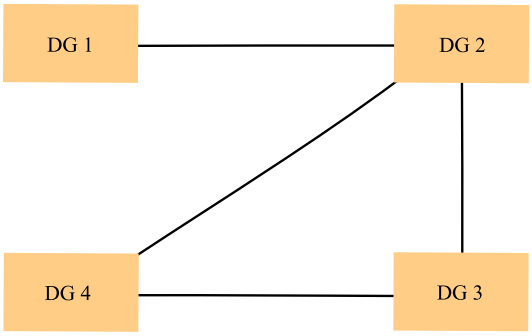

Figure 2.4: Connection of the cyber layer.

The case-specific system is a so-called multi-agent system where agents, in this case, DGs, work together to satisfy the objectives of the system [28]. Graph theory is often combined with control theory and can explain the agents' connection scheme and interactions [29]. As in Skaga's master's thesis [3], the interconnections between the DGs in the cyber layer are represented by *Graph 3*, which is defined as $\mathcal{M}_c = (\mathcal{N}_c, \mathcal{E}_c, \boldsymbol{\mathcal{A}})$. Where the nodes $\mathcal{N}_c$ represent the DGs, and the edges $\mathcal{E}_c$ represent the communication links between pairs of neighboring DGs. As shown in Figure 2.4, the graph corresponding to the case-specific CP MG has $n^{\mathcal{N}_c} = 4$ nodes and $n^{\mathcal{E}_c} = 4$ edges.

The communication links in the distributed control network have no defined flow direction. As a result, the graph representing the cyber layer, denoted as $\mathcal{M}_c$, is undirected. This implies that the corresponding adjacency matrix, $\boldsymbol{\mathcal{A}}$, is symmetric, meaning that $\boldsymbol{\mathcal{A}} = \boldsymbol{\mathcal{A}}^\top$. The elements of the symmetric adjacency matrix, denoted as a_{ij}, represent the communication weights between pairs of DGs, referred to as nodes i and j. If there is a communication link between two DGs in the cyber layer, then $a_{ij} = a_{ji} = 1$. If there is no communication link between two DGs in the cyber layer, then $a_{ij} = a_{ji} = 0$ [29].

The $\boldsymbol{\mathcal{A}}$-matrix of the case-specific CP MG have dimensions $\{n^{\mathcal{N}_c}, n^{\mathcal{N}_c}\}$ and is presented in (2.2.1) as in Skaga's master thesis [3].

$$\boldsymbol{\mathcal{A}} = \begin{bmatrix} a_{11} & a_{12} & a_{13} & a_{14} \\ a_{21} & a_{22} & a_{23} & a_{24} \\ a_{31} & a_{32} & a_{33} & a_{34} \\ a_{41} & a_{42} & a_{43} & a_{44} \end{bmatrix} = \begin{bmatrix} 0 & 1 & 0 & 0 \\ 1 & 0 & 1 & 1 \\ 0 & 1 & 0 & 1 \\ 0 & 1 & 1 & 0 \end{bmatrix} \tag{2.2.1}$$

The degree matrix, $\boldsymbol{\mathcal{D}}$, is a diagonal matrix, i.e. $\boldsymbol{\mathcal{D}} = \boldsymbol{\mathcal{D}}^\top$. The elements of the degree matrix contain the summation of each row in the adjacency matrix, which provides information on the number of edges connected to each node. The matrix is defined as $d_{ii} = \sum_{j=1}^{n^{\mathcal{N}_c}} a_{ij}$, which results in (2.2.2) for the case-specific MG.

$$\boldsymbol{\mathcal{D}} = \begin{bmatrix} d_{11} & 0 & 0 & 0 \\ 0 & d_{22} & 0 & 0 \\ 0 & 0 & d_{33} & 0 \\ 0 & 0 & 0 & d_{44} \end{bmatrix} = \begin{bmatrix} 1 & 0 & 0 & 0 \\ 0 & 3 & 0 & 0 \\ 0 & 0 & 2 & 0 \\ 0 & 0 & 0 & 2 \end{bmatrix} \tag{2.2.2}$$

The Laplacian matrix $\boldsymbol{\mathcal{L}}$ is defined as $\boldsymbol{\mathcal{L}} := \boldsymbol{\mathcal{D}} - \boldsymbol{\mathcal{A}}$ and presented in (2.2.3) for the case-specific MG.

$$\boldsymbol{\mathcal{L}} = \begin{bmatrix} 1 & -1 & 0 & 0 \\ -1 & 3 & -1 & -1 \\ 0 & -1 & 2 & -1 \\ 0 & -1 & -1 & 2 \end{bmatrix} \tag{2.2.3}$$

The Laplacian matrix has important properties, as explained in Appendix A.1, that will be utilized later in the master's thesis. As previously mentioned, the controller is also a part of the cyber layer. However, given the complexity of the controller, the next chapter is specifically dedicated to the controller.

Chapter 3

The Controller

This chapter aims to explore several aspects of the controller proposed in [2] to get a comprehensive understanding before the stability analysis is applied in the subsequent chapter 4. In control theory, it is common to formulate an optimization problem and further design a controller based on the corresponding optimal solution. Therefore, this chapter takes us on a path, starting from the optimization problem leading us towards the construction of the controller and how it satisfies the control objectives of voltage containment and proportional current-sharing. Eventually, the DC MG is implemented in Simulink to evaluate if the controller satisfies the control objectives when incorporated with the case-specific DC MG.

The first section of this chapter contains reproduced information from the associated specialization project [24], describing the optimization problem and the controller equations. However, this chapter offers a more comprehensive explanation of the controller and provides deeper insights into the different elements of the controller. Additionally, this chapter introduces an analysis of the steady state conditions and simulation results of the combined system.

3.1 Control Objectives

As stated in the introduction in chapter 1, the control objectives are to ensure voltage containment and proportional current-sharing. These objectives implies that $V_{\min} \leq \bar{V}_i^{\mathcal{G}} \leq V_{\max}$ and $\bar{I}_{i,\text{pu}}^{\mathcal{G}} = \bar{I}_{j,\text{pu}}^{\mathcal{G}}$ are maintained in steady state, where $\bar{x}$ denotes the variables at steady state. Abdolmaleki's publication [2] proposes an optimization problem and a controller which fulfills these objectives. The optimization problem is first formulated and used to design a controller that achieves the objectives.

The voltage and current in an electrical system are interrelated, meaning that the current naturally gets affected when the voltage is controlled. Consequently, the voltage containment will also limit the current as long as the voltage is bounded. With this information, optimizing with an optimal set point, $\bar{\lambda}$, as the optimization variable when providing proportional current-sharing is convenient. Thus, in the optimization problem, the output of the electrical network, $\bar{I}_{i,pu}^{\mathcal{G}}$, is only considered an external measurement. This approach simplifies the optimization problem compared to the case where $\bar{I}_{i,\text{pu}}^{\mathcal{G}}$ is selected as an optimization variable.

3.1.1 The Centralized Optimization Problem

First, the single-variable convex optimization problem from Abdolmaleki's publication [2] is formulated and studied to take it one step at a time. In this problem, the set point is $\bar{\lambda}$ and equal for all generators, and the communication between units is based on a centralized topology. The aim of the optimization problem is to find an optimal set point that can later be implemented in the controller to drive the current ratios equal to this optimal value. For the set point to be optimal with respect to every current ratio, it has to be the average of all the current ratios. Consequently, the sum of the differences between the optimal $\bar{\lambda}$ and $\bar{I}^{\mathcal{G}}_{i,\mathrm{pu}}$ needs to be minimized as in (3.1.1a). In this problem, it is evident that the optimal solution is when the objective function is zero, and the set point is equal to the current ratio.

$$\min_{\bar{\lambda}} \quad \frac{1}{2}\sum_{i=1}^{n^{\mathcal{G}_i}} (\bar{\lambda} - \bar{I}^{\mathcal{G}}_{i,\mathrm{pu}})^2 \tag{3.1.1a}$$

The Lagrangian function for the problem is as given in (3.1.2).

$$\mathbb{L}(\bar{\lambda}) = \frac{1}{2}\sum_{i=1}^{n^{\mathcal{G}_i}} (\bar{\lambda} - \bar{I}^{\mathcal{G}}_{i,\mathrm{pu}})^2 \tag{3.1.2}$$

The minimum of the Lagrangian function is derived in (3.1.3). Following the Karush-Kuhn-Tucker (KKT) conditions, (3.1.3c) will be the optimal solution to (3.1.1a). This occurs when the set point is equal to the average of all the generator currents, as desired. However, it should be noted that the currents are not changed in this optimization problem since it is optimized with respect to $\bar{\lambda}$ and not $\bar{I}^{\mathcal{G}}_{i,\mathrm{pu}}$.

$$\frac{\partial \mathbb{L}(\bar{\lambda})}{\partial \bar{\lambda}} = \sum_{i=1}^{n^{\mathcal{G}_i}} (\bar{\lambda} - \bar{I}^{\mathcal{G}}_{i,\mathrm{pu}}) = 0 \tag{3.1.3a}$$

$$n^{\mathcal{G}_i}\bar{\lambda} - \sum_{i=1}^{n^{\mathcal{G}_i}} \bar{I}^{\mathcal{G}}_{i,\mathrm{pu}} = 0 \tag{3.1.3b}$$

$$\bar{\lambda} = \frac{1}{n^{\mathcal{G}_i}}\sum_{i=1}^{n^{\mathcal{G}_i}} \bar{I}^{\mathcal{G}}_{i,\mathrm{pu}} \tag{3.1.3c}$$

3.1.2 The Distributed Optimization Problem

The case-specific CP MG has a distributed topology, where each DG only has information about its neighboring units. This implies that each DG has its own set point for the parameter $\bar{\lambda}$ and has no information on the set points of DGs that are not their neighboring units. Consequently, the equality constraint (3.1.4b) based on the distributed consensus algorithm explained in Appendix A.1 adds to the problem and set points, $\bar{\lambda}_i$, for each DG replace the common set point $\bar{\lambda}$ from (3.1.1a), as stated in [2]. The distributed cyber network has been modeled with an undirected communication graph, as demonstrated in section 2.2, where the communication weight between generator i and j is $a_{ij} = a_{ji}$ obtained from the adjacency matrix in (2.2.1). The undirected communication graph results in advantageous properties for the Laplacian matrix, which makes it possible for the set points given in (3.1.4b) to converge to a common consensus value as explained in Appendix A.1.

$$\min_{\bar{\lambda}_1,\ldots,\bar{\lambda}_{n^{\mathcal{G}_i}}} \quad \frac{1}{2}\sum_{i=1}^{n^{\mathcal{G}_i}}(\bar{\lambda}_i - \bar{I}^{\mathcal{G}}_{i,\mathrm{pu}})^2 \tag{3.1.4a}$$

$$\text{s.t.} \quad \bar{z}_i = \sum_{j\in N_{\mathcal{G}_i}} a_{ij}(\bar{\lambda}_j - \bar{\lambda}_i) = 0 \tag{3.1.4b}$$

$N_{\mathcal{G}_i}$ in (3.1.4b) is the neighbor-set of generator i, which contains the generators j that are communicating with generator i. The neighbor-set of each generator will be listed to give a clear understanding. In Figure 2.4, it can be seen that DG 4 is a neighbor of DG 2 and DG 3. Consequently, the neighbor-set of DG 4 is $N_{\mathcal{G}_4} = \{2, 3\}$. The sets corresponding to the case-specific CP MG are presented below.

$$\begin{aligned} N_{\mathcal{G}_1} &= \{2\} \\ N_{\mathcal{G}_2} &= \{1, 3, 4\} \\ N_{\mathcal{G}_3} &= \{2, 4\} \\ N_{\mathcal{G}_4} &= \{2, 3\} \end{aligned}$$

The Lagrangian function for the problem is as given in (3.1.5), where $\bar{\zeta}_i$ is the Lagrange multiplier of equality constraint (3.1.4b).

$$\mathbb{L}(\bar{\lambda}_i, \bar{\zeta}_i) = \frac{1}{2}\sum_{i=1}^{n^{\mathcal{G}_i}}(\bar{\lambda}_i - \bar{I}^{\mathcal{G}}_{i,\mathrm{pu}})^2 + \sum_{i=1}^{n^{\mathcal{G}_i}}\bar{\zeta}_i \underbrace{\sum_{j\in N_{\mathcal{G}_i}} a_{ij}(\bar{\lambda}_j - \bar{\lambda}_i)}_{\bar{z}_i} \tag{3.1.5}$$

In the publication, [2], it is stated that the optimal shapes of $\bar{\lambda}_i$ and $\bar{z}_i$ are as given in (3.1.7b) and (3.1.4b) respectively, as long as they satisfy the KKT conditions. The derivative of the Lagrangian function with respect to the Lagrange multiplier $\bar{\zeta}_i$, i.e., the relation in (3.1.4b) is first obtained and proven below in (3.1.6). This is in accordance with the KKT conditions of a convex problem with equality constraints [30].

$$\frac{\partial \mathbb{L}(\bar{\lambda}_i, \bar{\zeta}_i)}{\partial \bar{\zeta}_i} = \sum_{j\in N_{\mathcal{G}_i}} a_{ij}(\bar{\lambda}_j - \bar{\lambda}_i) = 0 \tag{3.1.6a}$$

$$\Rightarrow (\bar{\lambda}_j - \bar{\lambda}_i) = 0 \tag{3.1.6b}$$

$$\bar{\lambda}_i = \bar{\lambda}_j \tag{3.1.6c}$$

The optimal solution is given in (3.1.6c), where the set points are identical because of the properties of the Laplacian matrix described in Appendix A.1. However, it is essential to notice that even though $\bar{\lambda}_i = \bar{\lambda}_j$ it does not necessarily imply that the current ratio, $\bar{I}^{\mathcal{G}}_{i,\mathrm{pu}}$, is equal for all generators.

In Appendix A.2, the optimal shape of $\bar{\lambda}_i$ is derived from the derivative of the Lagrangian function with respect to each set point following the KKT conditions to provide a deeper comprehension. The result of the derivation is as given below in (3.1.7b).

$$\frac{\partial \mathbb{L}(\bar{\lambda}_i, \bar{\zeta}_i)}{\partial \bar{\lambda}_i} = \bar{\lambda}_i - \bar{I}^{\mathcal{G}}_{i,\mathrm{pu}} + \sum_{j \in N_{\mathcal{G}_i}} a_{ij} \left(\bar{\zeta}_j - \bar{\zeta}_i\right) = 0 \tag{3.1.7a}$$

$$\Rightarrow \bar{\lambda}_i = \bar{I}^{\mathcal{G}}_{i,\mathrm{pu}} + \sum_{j \in N_{\mathcal{G}_i}} a_{ij} \left(\bar{\zeta}_i - \bar{\zeta}_j\right) \tag{3.1.7b}$$

In conclusion, the optimal shape for each set point in the case-specific CP MG is given below in (3.1.8).

$$\bar{\lambda}_1 = \bar{\lambda}_2 = \bar{\lambda}_3 = \bar{\lambda}_4 \tag{3.1.8a}$$

$$\bar{\lambda}_i = \bar{I}^{\mathcal{G}}_{i,\mathrm{pu}} + \sum_{j \in N_{\mathcal{G}_i}} a_{ij} \left(\bar{\zeta}_i - \bar{\zeta}_j\right) \rightarrow \begin{cases} \bar{\lambda}_1 & = \bar{I}^{\mathcal{G}}_{1,\mathrm{pu}} + a_{12}(\bar{\zeta}_1 - \bar{\zeta}_2) \\ \bar{\lambda}_2 & = \bar{I}^{\mathcal{G}}_{2,\mathrm{pu}} + a_{21}(\bar{\zeta}_2 - \bar{\zeta}_1) + a_{23}(\bar{\zeta}_2 - \bar{\zeta}_3) + a_{24}(\bar{\zeta}_2 - \bar{\zeta}_4) \\ \bar{\lambda}_3 & = \bar{I}^{\mathcal{G}}_{3,\mathrm{pu}} + a_{32}(\bar{\zeta}_3 - \bar{\zeta}_2) + a_{34}(\bar{\zeta}_3 - \bar{\zeta}_4) \\ \bar{\lambda}_4 & = \bar{I}^{\mathcal{G}}_{4,\mathrm{pu}} + a_{42}(\bar{\zeta}_4 - \bar{\zeta}_2) + a_{43}(\bar{\zeta}_4 - \bar{\zeta}_3) \end{cases} \tag{3.1.8b}$$

Note that the optimal shape of $\bar{\lambda}_i$ above does not correspond to the definition of proportional current-sharing. However, it is worth noting that in situations where the voltages at the generators are within their operating limits and do not need to be saturated, the relation $\bar{\lambda}_i = \bar{I}^{\mathcal{G}}_{i,\mathrm{pu}}$ is valid for the distributed topology. This is because the last term of (3.1.7b) is linked to voltage saturation and will only be present when the voltages are saturated, as we will show in section 3.2. Therefore, proportional current-sharing is provided as long as the voltages are within operating limits. During saturation, the controller provides the optimal shape in (3.1.7b), per the optimization problem. However, this shape is only a sub-optimal shape in an operated MG. Nevertheless, with the information from the optimization problem, we know that this is the best shape during the saturation of the voltages. This will be explained in further detail in the subsequent section 3.2.

3.2 The Nonlinear Controller

A nonlinear controller that maintains voltage containment and proportional current-sharing in a DC MG is designed in Babak Abdolmaleki's and Gilbert Bergna-Diaz's publication of *A Nonlinear Control Framework for Optimal Load-sharing and Voltage Containment in DC Networks* [2]. The controller is based on the optimization problem in section 3.1, and its goal is to provide voltage containment and proportional current-sharing. The controller should also provide the optimal value of $\bar{z}_i$ in (3.1.4b), such that all set points in the DC MG are equal, i.e., $\bar{\lambda}_i = \bar{\lambda}_j$ as in (3.1.6c). If proportional current-sharing is not possible, the controller should provide the sub-optimal shape of $\bar{\lambda}_i$ in (3.1.7b). This also implies that the voltages are kept within limits and that the difference, $(\bar{\lambda}_i - \bar{I}^{\mathcal{G}}_{i,\mathrm{pu}})$, is minimized. Therefore, the load-ratio output $I^{\mathcal{G}}_{i,\mathrm{pu}}{=}I^{\mathcal{G}}_i/I^{\mathcal{G}}_{\mathrm{rated}}$ of the DC MG modeled in section 2.1 will go to a value that is optimal according to the present operating conditions in steady state. As stated by Ohm's law, voltage saturation will also constrain the currents, ensuring that both the voltage and current do not go to undesirable high values. This is why voltage containment can be prioritized over proportional current-sharing in the controller. The electrical network's proposed controller in [2] is as follows in (3.2.1).

$$u_{i,p} = \Delta \tanh\left(\frac{v_i}{\Delta}\right) \tag{3.2.1a}$$

$$\tau \dot{v}_i = -\rho(v_i) v_i + V_{\text{nom}}(\lambda_i - I^{\mathcal{G}}_{i,\text{pu}}) \tag{3.2.1b}$$

$$\rho(v_i) = \begin{cases} \left|\frac{v_i}{\Delta}\right| - 3 & \text{if } |v_i| > 3\Delta \\ 0 & \text{otherwise} \end{cases} \tag{3.2.1c}$$

$$V_{\text{nom}} = \frac{1}{2}(V_{\min} + V_{\max}) \tag{3.2.1d}$$

$$\Delta = \frac{1}{2}(V_{\max} - V_{\min}) \tag{3.2.1e}$$

In (3.2.1), v_i is the regulator state, which is the voltage that possibly needs to be saturated, τ is the time constant, and $\rho(v_i) \geq 0$ is a nonlinear leakage coefficient [2]. V_{nom} in (3.2.1d) is the nominal voltage of the DGs, which is in the middle of the DGs rated voltage operating region. In contrast, Δ in (3.2.1e) expresses how much v_i is allowed to deviate from V_{nom} before the voltage constraints are reached. In combination with the fact that $-1 < \tanh(\cdot) < 1$, this ensures that the controller in (3.2.1a) provides voltage containment.

Under normal conditions the leakage coefficient $\rho(v_i)$ is equal to zero and $\tau \dot{v}_i = V_{\text{nom}}(\lambda_i - I^{\mathcal{G}}_{i,\text{pu}})$ in (3.2.1b). Accordingly, $I^{\mathcal{G}}_{i,\text{pu}}$ follows the reference value of λ_i and the desirable operation condition in steady state is achieved: $\tau \dot{\bar{v}}_i = V_{\text{nom}}(\bar{\lambda}_i - \bar{I}^{\mathcal{G}}_{i,\text{pu}}) = 0 \Rightarrow \bar{\lambda}_i = \bar{I}^{\mathcal{G}}_{i,\text{pu}}$. However, suppose the voltage set point, V_i^{set}, reaches the operational limits of the generator. In that case, the regulator voltage, v_i, needs to be saturated, and the leakage coefficient is activated. Consequently, $\bar{\lambda}_i$ and $\bar{I}^{\mathcal{G}}_{i,\text{pu}}$ will not be equal.

The saturation of the regulator state happens when the voltage reaches the minimum or maximum allowed limits. The integral term in (3.2.1b) continuously adjusts the regulator state to reduce the error until the generator currents reach the set point. However, during saturation of the regulator state, this state can no longer affect the generator currents. As a result, the integral term continues to accumulate the constant error during saturation, and the regulator state struggles to ensure an equilibrium $\dot{\bar{v}}_i = 0$ in steady state. This is a direct consequence of the nonlinear saturation, a phenomenon known as integrator wind up, which commonly occurs in controllers with integral terms, such as the controller in (3.2.1b) — resulting in a delay in error tracking and an increase in settling time when the system recovers from the saturation. Slow response times, overshoot, and that it takes longer for the controller to return to steady state conditions are the consequences of the nonlinear saturation [31].

An anti-wind up technique is used by introducing the leakage coefficient $\rho(v_i)$ from (3.2.1c) to prevent the wind up. This leakage coefficient will be activated in (3.2.1b) when the voltage v_i reaches the saturation point and $|v_i| > 3\Delta$. The activation of the leakage coefficient should ensure the steady state equilibrium of the regulator state, even under circumstances where there exists an error between the set point and the generator current. Hence, the leakage coefficient increases until the following relationship is obtained in steady state: $\dot{\bar{v}}_i = 0 \Rightarrow \rho(\bar{v}_i)\bar{v}_i = V_{\text{nom}}(\bar{\lambda} - \bar{I}^{\mathcal{G}}_{i,\text{pu}})$ and the accumulation of the error is prevented.

In other words, the leakage coefficient can be regarded as a *safety vault* to prevent integrator wind up and to ensure an equilibrium in steady state. To guarantee a stable operation, it implies that $\bar{I}^{\mathcal{G}}_{i,\text{pu}}$ is forced to be shaped like in (3.2.2) and not the desired shape of $\bar{I}^{\mathcal{G}}_{i,\text{pu}} = \bar{\lambda}_i$.

$$\bar{I}^{\mathcal{G}}_{i,\mathrm{pu}} = \bar{\lambda}_i - \frac{1}{V_{\mathrm{nom}}}\rho(\bar{v}_i)\bar{v}_i \tag{3.2.2}$$

However, as demonstrated in (3.1.7b) and section 3.1, this shape is optimal considering that the voltage reaches the operating limits. The controller is focusing on keeping the voltages within limits while doing its best to provide proportional current sharing, meaning this is the closest $\bar{I}^{\mathcal{G}}_{i,\mathrm{pu}}$ can be to $\bar{\lambda}_i$ when the voltage set point is close to the operating limits. It also follows that the current ratios of the generators are not equal to each other during saturation, i.e., $\bar{I}^{\mathcal{G}}_{i,\mathrm{pu}} \neq \bar{I}^{\mathcal{G}}_{j,\mathrm{pu}}$. More significant deviations in the current ratios will occur as the voltage reaches saturation and the leakage coefficient increases in size. However, this approach is preferred because it provides stable conditions in steady state, while limiting deviations.

Note that the condition $|v_i| > 3\Delta$ in (3.2.1c) is chosen based on the correlation $\tanh(3) \approx 1$. For even greater values, $\tanh(\cdot)$ gets even closer to unity. If this is the case, the generator voltage in (2.1.3e) yields $V_i^{\mathcal{G}} \approx V_{\mathrm{nom}} \pm \Delta$, where $V_i^{\mathcal{G}}$ approaches the limits in the voltage operating region due to the definitions of V_{nom} and Δ. However, the design of the controller ensures that the voltage set point will never wholly reach the limits in this case. Thus, the controller provides an acceptable level of accuracy for the voltage set point [2].

So far, several shapes of $\bar{\lambda}_i$ have been derived. It can be observed that the shape of $\bar{\lambda}_i$ in Equation (3.2.2) is equivalent to the shape of $\bar{\lambda}_i$ in (3.1.7b) imposed by the equality from the optimizing problem. By setting the two equations equal to each other, the following correlation in (3.2.3b) is obtained.

$$\bar{I}^{\mathcal{G}}_{i,\mathrm{pu}} + \sum_{j \in N_{\mathcal{G}_i}} a_{ij}\left(\bar{\zeta}_i - \bar{\zeta}_j\right) = \bar{I}^{\mathcal{G}}_{i,\mathrm{pu}} + \frac{1}{V_{nom}}\rho(\bar{v}_i)\bar{v}_i \tag{3.2.3a}$$

$$\sum_{j \in N_{\mathcal{G}_i}} a_{ij}\left(\bar{\zeta}_i - \bar{\zeta}_j\right) = \frac{1}{V_{nom}}\rho(\bar{v}_i)\bar{v}_i \tag{3.2.3b}$$

It is clear that both of these expressions are related to the leakage coefficient and the saturation of the voltage set point. Therefore, it is deduced that the term $\sum_{j \in N_{\mathcal{G}_i}} a_{ij}\left(\bar{\zeta}_i - \bar{\zeta}_j\right)$ in (3.1.7) obtained through the optimizing problem will be zero as long as the voltage set point is within limits and v_i is not close to being saturated. This is in line with the previously stated characteristics of the leakage coefficient. These saturation terms provide stable performance under different operating conditions.

3.2.1 The Cyber Controller

To find the optimal $\bar{\lambda}_i$ to be used in the local controller in (3.2.1), Proportional-Integral (PI) Dynamic Consensus Estimators can be implemented at each DG and are defined in Abdolmaleki's [2] as presented in (3.2.4), where k_P, k_I, and k_y are positive gains. These estimators were based on an algorithm presented in [32]. The estimators consist of the internal estimator states, ζ_i and λ_i, which are received as input from neighboring generators [32]. Thus, these states are exchanged in a distributed manner and can be considered the *cyber states* of the CP MG. *Cyber state* is an expression introduced in Skaga's master's thesis [3] and was used to name the states in the distributed control network, i.e., the cyber layer.

$$\dot{\zeta}_i = k_I \sum_{j \in N_{\mathcal{G}_i}} a_{ij}(\lambda_j - \lambda_i) \tag{3.2.4a}$$

$$\dot{\lambda}_i = k_y(I^{\mathcal{G}}_{i,\text{pu}} - \lambda_i) + k_y \sum_{j \in N_{\mathcal{G}_i}} a_{ij}(\zeta_i - \zeta_j) + k_P \sum_{j \in N_{\mathcal{G}_i}} a_{ij}(\lambda_j - \lambda_i) \tag{3.2.4b}$$

3.3 Steady State Conditions in the Cyber Layer

The steady state conditions are of interest because we eventually want the system to operate at the optimal steady state operating point. Therefore, the following sections investigate the steady state conditions of the cyber layer, including the estimator states and the regulator state.

3.3.1 Steady State Conditions in the Distributed Control Network

As long as communication is present and the adjacency matrix of the control network's communication graph is connected, the steady state behavior of the estimators will satisfy the KKT conditions [2]. This can be proven by considering the steady state conditions of (3.2.4a) and (3.2.4b) in vector form as presented in (3.3.1a) and (3.3.1b), respectively. Each generator in the network has two corresponding cyber states, such that $\boldsymbol{\zeta} \in \mathbb{R}^{n_i^{\mathcal{G}}}, \boldsymbol{\lambda} \in \mathbb{R}^{n_i^{\mathcal{G}}}$. Furthermore, $\boldsymbol{K}_P$, $\boldsymbol{K}_I$ and $\boldsymbol{K}_y$ are diagonal matrices that contains the positive gains and have the following dimension $\mathbb{R}^{n_i^{\mathcal{G}} \times n_i^{\mathcal{G}}}$.

$$\dot{\boldsymbol{\zeta}} = -\boldsymbol{K}_I \boldsymbol{\mathcal{L}} \boldsymbol{\lambda} \tag{3.3.1a}$$

$$\dot{\boldsymbol{\lambda}} = \boldsymbol{K}_y(\boldsymbol{I}^{\mathcal{G}}_{\text{pu}} - \boldsymbol{\lambda}) + \boldsymbol{K}_y \boldsymbol{\mathcal{L}} \boldsymbol{\zeta} - \boldsymbol{K}_P \boldsymbol{\mathcal{L}} \boldsymbol{\lambda} \tag{3.3.1b}$$

Solving (3.3.1a) in steady state, results in the following relationship: $-\boldsymbol{K}_I \boldsymbol{\mathcal{L}} \bar{\boldsymbol{\lambda}} = \boldsymbol{0} \Rightarrow \boldsymbol{\mathcal{L}} \bar{\boldsymbol{\lambda}} = \boldsymbol{0}$. From the properties of the Laplacian-matrix explained in Appendix A.1, this relationship implies that $\bar{\boldsymbol{\lambda}}$ consists of identical elements and that all generators share the same $\bar{\lambda}_i$, i.e., $\boldsymbol{\mathcal{L}} \bar{\boldsymbol{\lambda}} = 0$, where $\bar{\boldsymbol{\lambda}} = [\bar{\lambda}_i, \bar{\lambda}_i, ..., \bar{\lambda}_i]^\top = \bar{\lambda}[1, 1, \ldots, 1]^\top$. Due to this relationship, the term $\boldsymbol{K}_P \boldsymbol{\mathcal{L}} \bar{\boldsymbol{\lambda}} = \boldsymbol{0}$ in (3.3.1b) is removed, which implies

$$\begin{aligned} \boldsymbol{K}_y(\bar{\boldsymbol{I}}^{\mathcal{G}}_{\text{pu}} - \bar{\boldsymbol{\lambda}}) + \boldsymbol{K}_y \boldsymbol{\mathcal{L}} \bar{\boldsymbol{\zeta}} &= \boldsymbol{0} \\ \Rightarrow \bar{\boldsymbol{I}}^{\mathcal{G}}_{\text{pu}} - \bar{\boldsymbol{\lambda}} + \boldsymbol{\mathcal{L}} \bar{\boldsymbol{\zeta}} &= \boldsymbol{0} \\ \Rightarrow \bar{\boldsymbol{\lambda}} = \bar{\boldsymbol{I}}^{\mathcal{G}}_{\text{pu}} + \boldsymbol{\mathcal{L}} \bar{\boldsymbol{\zeta}} & \end{aligned} \tag{3.3.2}$$

The shape of $\bar{\boldsymbol{\lambda}}$ is identical to the previously derived optimal shape of $\bar{\lambda}_i$ from the optimization problem in section 3.1.2. Since the expression contains the Laplacian matrix, it is possible to take advantage of the properties of this unique matrix. As explained in Appendix A.1, $\boldsymbol{1}^\top \boldsymbol{\mathcal{L}} = \boldsymbol{0}$. To better illustrate the derivations below, an example is conducted on a vector $\boldsymbol{x}$ of n equal elements: $\boldsymbol{1}^\top \boldsymbol{x} = \sum_{i=1}^{n} x_i = n x_i$. Furthermore, multiplying each term by $\boldsymbol{1}^\top$ gives an expression of the set points in steady state as shown in (3.3.3).

$$\begin{aligned} \mathbf{1}^\top \bar{\boldsymbol{\lambda}} &= \mathbf{1}^\top \bar{\boldsymbol{I}}_{\text{pu}}^{\mathcal{G}} + \mathbf{1}^\top \boldsymbol{\mathcal{L}} \bar{\boldsymbol{\zeta}} \\ \Rightarrow n^{\mathcal{G}_i} \lambda_i &= \mathbf{1}^\top \bar{\boldsymbol{I}}_{\text{pu}}^{\mathcal{G}} \\ \Rightarrow \bar{\lambda}_i &= \frac{1}{n^{\mathcal{G}_i}} \sum_{i=1}^{n^{\mathcal{G}_i}} \bar{I}_{i,\text{pu}}^{\mathcal{G}} \end{aligned} \tag{3.3.3}$$

The derivations above demonstrate that the set points, $\bar{\lambda}_i$, are of optimal shape according to the optimization problem. Furthermore, these set points are equal to the average of all the generator current ratios in the network, which is the optimal solution of the centralized case, as explained in section 3.1.1 and expressed in (3.1.3). Consequently, the set points converge to a value that minimizes the difference between the currents and the set points. It can be beneficial to express the set points in vector notation for a later stage. Therefore, the expression is multiplied by the vector of ones, $\mathbf{1}$, on both sides in (3.3.4).

$$\bar{\boldsymbol{\lambda}} = \frac{\mathbf{1} \cdot \mathbf{1}^\top \bar{\boldsymbol{I}}_{\text{pu}}^{\mathcal{G}}}{n^{\mathcal{G}_i}} \tag{3.3.4}$$

In conclusion, it has been proven that the expressions for the estimator states, i.e., the cyber states, are formulated such that they satisfy the optimal shape of $\bar{\lambda}_i$ in steady state, as derived from the optimization problem.

3.3.2 Steady State Conditions in the Regulator State

The steady state conditions of the regulator state (3.2.1b) were expressed in (3.2.2). And can also be examined in vector notation, resulting in (3.3.5). The vector elements in $\boldsymbol{\rho}(\bar{\boldsymbol{v}})$ are either zero or non-zero depending on whether the corresponding generator is saturating its voltage or not, respectively. Consequently, the current ratio corresponding to a DG that is not saturating its voltage will be equal to the set point obtained by consensus, while the current ratio corresponding to a DG that is saturating its voltage will take on the sub-optimal shape as explained in section 3.2.

$$\begin{aligned} \tau \dot{\bar{\boldsymbol{v}}} &= -\rho(\bar{\boldsymbol{v}})\bar{\boldsymbol{v}} + V_{\text{nom}}(\bar{\boldsymbol{\lambda}} - \bar{\boldsymbol{I}}_{\text{pu}}^{\mathcal{G}}) = \mathbf{0} \\ \Rightarrow \bar{\boldsymbol{I}}_{\text{pu}}^{\mathcal{G}} &= \bar{\boldsymbol{\lambda}} - \frac{1}{V_{\text{nom}}} \rho(\bar{\boldsymbol{v}})\bar{\boldsymbol{v}} \end{aligned} \tag{3.3.5}$$

3.4 Simulations of the Nonlinear Controller

This section aims to give a proper understanding of the controller by exploring the function of its elements – the regulator, the hyperbolic tangent function, and the leakage coefficient. It will be explained why these elements are included in the controller, and it will be demonstrated how they work together to achieve the desired objectives in the DC MG. This will be done by implementing the model of the physical DC MG in Simulink and by including the different elements of the controller step by step.

The DC MG is implemented in Simulink following the structure as given in Figure 2.1. The parameters for the first two simulations are presented below in Table 3.1, 3.2, and 3.3, providing

the data of all the generators, transmission lines, and loads in the DC MG. However, in subsequent simulations, the load and transmission line data will be modified to illustrate the controller's working better. The time constant of the controller is set to $\tau = 3$, and the gains are set to $k_I = 1.3$, $k_y = 10$, and $k_p = 50$.

Table 3.1: Generator (DG) Specifications.

Parameters	**DG 1**	**DG 2**	**DG 3**	**DG 4**
$I_{i,\text{rated}}$ [A]	12	4	8	6
V_{nom} [V]	48	48	48	48
Δ [V]	0.48	0.48	0.48	0.48
$R_i^{\mathcal{G}}$ [Ω]	0.075	0.06	0.0825	0.0675
$L_i^{\mathcal{G}}$ [mH]	0.15	0.12	0.165	0.135

Table 3.2: Transmission Line (TL) Specifications.

Parameters	**TL 1**	**TL 2**	**TL 3**	**TL 4**	**TL 5**
$R_j^{\mathcal{E}}$ [Ω]	0.3	0.6	0.6	0.3	0.3
$L_j^{\mathcal{E}}$ [mH]	0.6	1.2	1.2	0.6	0.6

Table 3.3: Load (L) Specifications.

Parameters	**L 1**	**L 2**	**L 3**	**L 4**
$C_k^{\mathcal{N}}$ [mF]	22	22	22	22
$1/G_k^{\text{cte}}$ [Ω]	40	30	30	20
I_k^{cte} [A]	2	2.1	1.9	2

Four graphs are obtained for each simulation, displaying the behavior of three crucial states in the system – The generator's current ratio ($\boldsymbol{I}^{\mathcal{G}}$), the generator voltages ($\boldsymbol{V}^{\mathcal{G}}$), and the regulator states ($\boldsymbol{v}$), as well as the leakage coefficients ($\rho(\boldsymbol{v})$). The information obtained from these states is essential in understanding the DC MG's stability, the controller's performance, and if the control objectives are satisfied.

In all the simulations presented below, the DC MG is achieving steady state conditions before the controller is activated at $t = 10s$. Furthermore, the DC MG is achieving new steady state conditions before a load change is applied at $t = 20s$ and removed at $t = 30s$. The load change is implemented as a 50% increase in current consumption at each load in the DC MG by introducing a step block in the Simulink model. The events are summarized in Table 3.4 below.

Table 3.4: Events implemented in the simulations.

Time Interval [s]	**Event**
$[0, 10]$	The DC MG is uncontrolled
$[10, 50]$	The controller is activated
$[20, 30]$	50% increased current consumption at the loads

3.4.1 Neglecting the Controller

The initial 10 seconds of the simulations in the figures below illustrate the DC MG without the controller; the currents are not proportionally shared between the generators, and the generator

voltages are equal to the nominal voltage. Moreover, the regulator states and leakage coefficients are equal to zero since they are part of the inactivated controller, and their values have not yet been assigned.

3.4.2 Neglecting the Leakage Coefficient

The simulation results illustrated in Figure 3.1 represent the DC MG with parameters identical to those specified in Table 3.1, 3.2, and 3.3. In this simulation, the controller gets activated at $t = 10$. However, the leakage coefficient from (3.2.1c) is disregarded to investigate why this element is needed in the controller. The voltage band is set to the strict interval of $[V_{\min}, V_{\max}] = [0.99\text{pu}, 1.01\text{pu}]$ to examine the functioning of the controller under heavily constrained conditions. As observed after the activation of the controller, the current ratios are going toward identical per unit values, while the generator voltages are kept within their limit. It is clear that DG 2 is approaching the minimum voltage limit of 0.99pu and is forced not to exceed this limit because of the hyperbolic tangent function that is saturating the voltage. The regulator state corresponding to DG 2 has a slight decrease because of this saturation, but it reaches a stable equilibrium in steady state. Thus, the controller manages sufficiently and achieves the control objectives without the leakage coefficient.

However, when the current consumption at the loads is increased during the time interval of $[20, 30]$ seconds, all the current ratios increase, making it harder for the generator voltages to be kept within limits. As a result, the voltages at DG 1 and DG 3 also approach the voltage limit. Due to the size of the load change and the strict saturation term, the two generators experiencing the greatest saturation, i.e., DG 2 and DG 3, are not able to achieve proportional current-sharing. For the same reason, their corresponding regulator states experience wind up, as seen in the sharp change of the corresponding regulator states. The change in the regulator state implies that the distance between the set point and the current ratio is nonzero, i.e., $\tau\dot{v}_i \neq 0 \Rightarrow \lambda_i \neq I^{\mathcal{G}}_{i,\text{pu}}$ meaning that an error exists. The error accumulates, and the regulator states do not reach a steady state equilibrium, as explained in section 3.2. Note that the two generators that experience the least saturation, i.e., DG 1 and DG 4, have approximately equal currents throughout the simulation period – implying that these DGs converge to a common set point. As seen by the simulation, these two DGs' currents are in between the two other DGs' current ratios, resulting in a consensus equal to the average of all the generator currents as proved in (3.3.3).

The step in load is removed after 30 seconds, and the system attempts to return to its original state and achieve proportional current-sharing. However, this process is slow and takes about 10 seconds because of the significant error accumulation in the regulators of the saturated DGs. The error has to decrease before the regulator can drive the current ratios equal to the set point decided by consensus. When the error has decreased sufficiently, the currents eventually get equal, and the control objectives are achieved. The slow and inefficient behavior of this recovery period is why it is advantageous to include the leakage coefficient, and will be explained in the subsequent section.

3.4.3 Including the Leakage Coefficient

The leakage coefficient is included in the second simulation with results presented in Figure 3.2. The load and transmission line parameters are unchanged, and the simulation follows the same events as described in Table 3.4. It can be observed that the DGs achieve proportional current-sharing and that the generator voltages are contained after the activation of the controller. In other words, there exists a remarkable similarity in the first time interval between the first and second simulation results of the generator currents and voltages.

During the time interval $[20, 30]$ seconds, the system is heavily loaded, and the leakage coefficients corresponding to DG 2 and DG 3 increase because of the saturation of the corresponding regulator voltages and the fact that $\{v_2, v_3\} > 3\Delta$ as described in (3.2.1c). From the simulations, it can be confirmed that these leakage coefficients increase until the regulator states find an equilibrium, as explained in the previous section 3.2. The leakage coefficients compensate for the error in the regulator states and prevent integrator wind up. Thus, the system and all its states achieve steady state operation when the load is changed. This is different from the previous simulation without the leakage coefficients, where the two regulator states were not achieving steady state operation.

When the load step is removed at $t = 30$ seconds, the voltages of the regulator states return to the closest equilibrium. Consequently, the regulator states get closer to zero, followed by a drop in the leakage coefficients. Furthermore, the generator currents quickly go back to proportional current-sharing, and the recovery period of 10 seconds from the last simulation is drastically improved by including the leakage coefficient. The simulations demonstrate the efficiency of the leakage coefficient and why this is included in the controller.

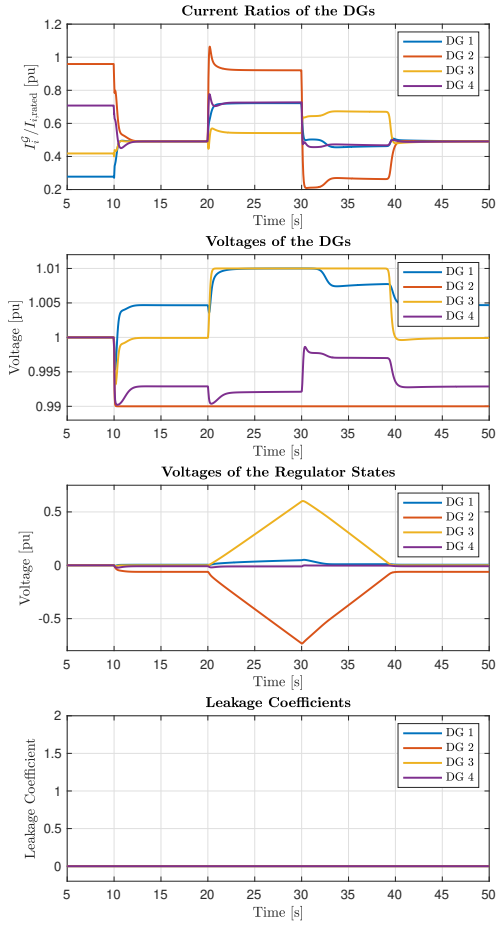

Figure 3.1: $[V_{\min}, V_{\max}] = [0.99 \text{ pu}, 1.01 \text{ pu}]$. The leakage coefficient is not included.

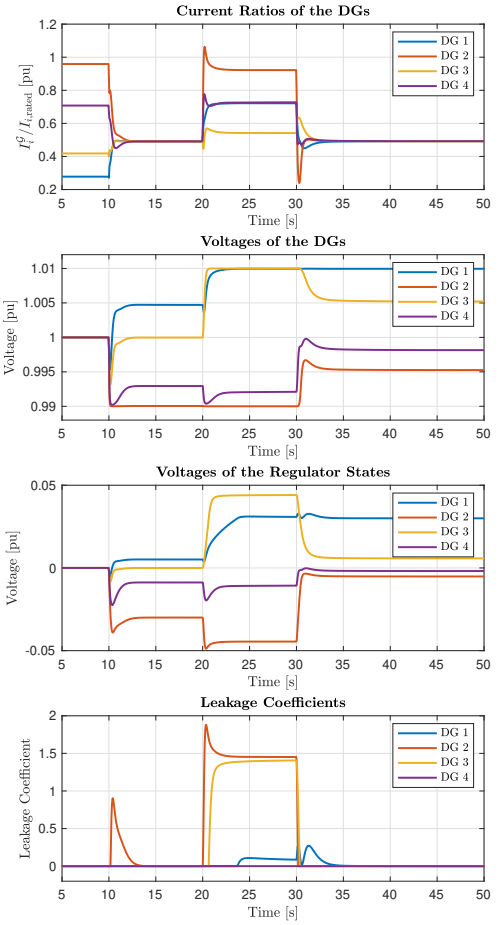

Figure 3.2: $[V_{\min}, V_{\max}] = [0.99 \text{ pu}, 1.01 \text{ pu}]$. The leakage coefficient is included.

3.4.4 Adjusting the Voltage Limits

In Figure 3.3, the voltage limits are adjusted to the more realistic interval, $[V_{\min}, V_{\max}] = [0.95\text{pu}, 1.05\text{pu}]$, while the load and transmission line parameters are unchanged. As reflected by the simulations, these limits are not strict for this specific system since all the generator voltages are within the voltage bands in every time interval. Thus, the leakage coefficients are zero, the regulator voltages are not saturated, and wind up is not an issue. Furthermore, due to the unproblematic behavior of the voltages, the DGs perfectly achieve proportional current-sharing during the whole simulation period.

3.4.5 Modyfing the Load and Transmission Line Parameters

The system described in Figure 3.3 works perfectly and does not illustrate the saturation of voltages or activation of the leakage coefficients. Therefore, the system parameters are modified to illustrate better the controller's working in a more realistic system. The load current and transmission line parameters from Table 3.2 and 3.3 are modified by doing the following multiplication: $2 \cdot I_k^{\text{cte}}$, $2.25 \cdot R_j^{\mathcal{E}}$ and $2.25 \cdot L_j^{\mathcal{E}}$. The simulation results are depicted in Figure 3.4 and exhibit similarities to the results presented in Abdolmaleki's publication [2], where accurate proportional current-sharing is quickly achieved outside the load change. During the load change, the generator voltages at DG 2 and DG 3 are saturated to the extent that the corresponding leakage coefficients are activated. This results in the current ratios of DG 2 and DG 3 going towards the sub-optimal value in (3.2.2) in steady state. However, the voltages are kept within limits, and the controller is doing its best to maintain proportional current-sharing. When the load change is removed, the system is smoothly recovering in a few seconds.

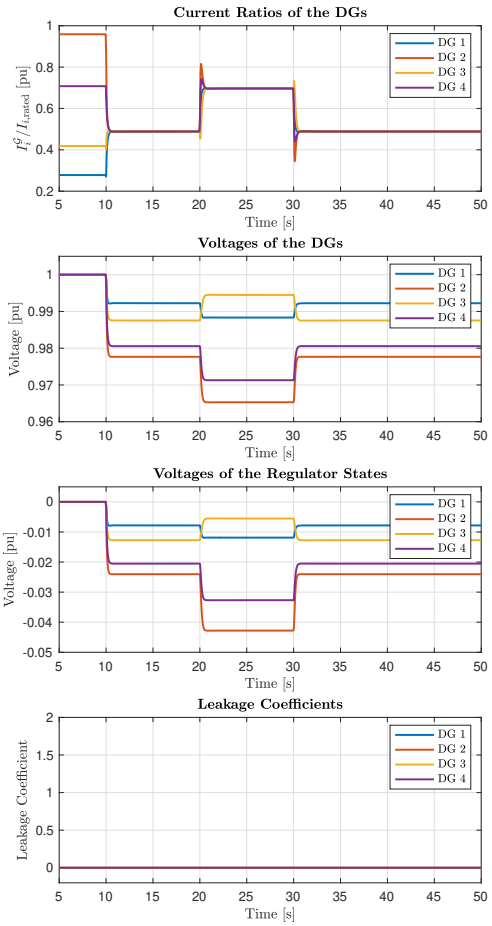

Figure 3.3: The voltage limits are adjusted to $[V_{\min}, V_{\max}] = [0.95 \text{ pu}, 1.05 \text{ pu}]$.

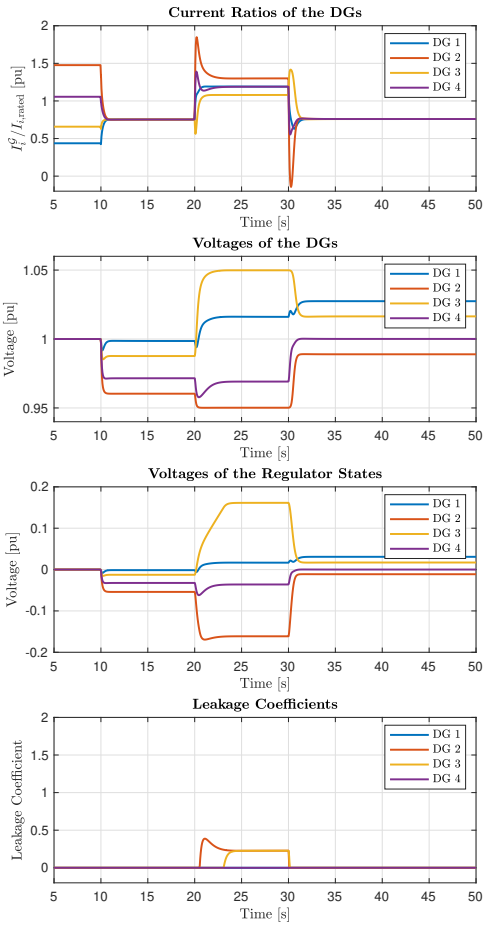

Figure 3.4: $[V_{\min}, V_{\max}] = [0.95 \text{ pu}, 1.05 \text{ pu}]$. Parameters from Table 3.1 and updated TL and load parameters.

The period where the system experiences a change, i.e., when the controller is activated or when the step in load is applied, describes the system's transient behavior. The simulation results presented in these sections show short transients containing overshoots and inadequate responses. However, the performance is not the primary focus of this thesis, as emphasized in Limitation of Scope in section 1.2.1. Additionally, the case-specific DC MG is of small size and, consequently, it is low inertia in the system, resulting in reduced resilience against changes. Contrary to this limitation, the controller behaved as expected in all simulations, successfully achieving the control objectives and ensuring steady state operation. In conclusion, the controller is well-suited for managing the DC MG presented in Figure 2.1.

Chapter 4

Energy Modeling and Analysis

In the previous chapter, the controller proposed in [2] was implemented in the case-specific DC microgrid, and simulations were conducted in Simulink. It was demonstrated that the controller successfully satisfies the two control objectives as presented in [2]. Although it was not discovered any instability issues in the simulations, it cannot be guaranteed that the system will remain stable if it scales up in size. Following the principles discussed in the introduction in chapter 1, obtaining a stability proof applicable to all DC MG configurations is desired. The thorough elaboration of the controller from the previous chapter 3 offers insight into the responsibilities of the different elements in the controller. This understanding is essential information before entering the stability analysis, as it will be necessary to do simplifications regarding the controller. By doing so, we can make informed decisions about the necessary simplifications.

In this chapter, the theory on port-Hamiltonian systems and Lyapunov's stability criteria are reproduced from the associated specialization project [24]. Additionally, the specialization project presented the energy modeling of the electrical and distributed control networks. This information is also reproduced in this chapter and serves as important preliminary information prior to the new contribution of the clarification about why the current ratio needs to be included in the mathematical equations, identifying the passive outputs, interconnecting the two layers and identifying the challenges in the connection. The new analysis also contains mathematical proofs and validation of the results using simulations in Simulink.

4.1 Introducing Port-Hamiltonian System Theory and Lyapunov Stability Criteria

In the next sections, an investigation will be conducted to determine whether the open-loop electrical network and control network admits to a port-Hamiltonian (pH) representation. In order to accomplish this, it will be necessary to introduce the theoretical foundations of pH systems and Lyapunov's Stability Criteria. These frameworks are primarily used to investigate nonlinear systems but are also applicable to linear systems [33]. As stated in the introduction in chapter 1, disregarding the nonlinearities in the controller has been necessary due to the complex structure of the combined network. However, the next step for the specific system is to consider the nonlinearities, which is why a nonlinear stability analysis is utilized in this master's thesis. However, due to the relative complexity of the controller, the next chapter is dedicated to breaking it down.

4.1.1 Port-Hamiltonian System Theory

A port-Hamiltonian representation of a system is a way of rewriting a system of differential equations, where the system's energy-dissipating elements and the interconnection in the system are emphasized. For example, in the DC MG, *Graph 1* and *Graph 2* function as interconnections between the three subsystems; the sets of generators, loads, and transmission lines. Port-Hamiltonian representations of systems also allow for connecting and analyzing interconnected subsystems from different domains [34]. This makes it possible to interconnect a distributed cyber layer to the physical network layer described above, which also allows for analyzing the stability of the combined cyber-physical system. The port-Hamiltonian representation is also a valuable tool in designing a passivity-based controller (PBC), which can ensure the stability of a closed-loop system.

The systems introduced in this master's thesis belong to a subclass of pH systems, *input-state-output* port-Hamiltonian systems. These pH systems occur if *1. There are no algebraic constraints between the state variables, 2. The external port variables can be split into input and output variables, and 3. The resistive structure is linear and of input-output form* [34]. This type of pH system is well-established in the control theory community. Equation (4.1.1a) shows the state space representation of $\sum_{u,y}$, an input-state-output pH system.

$$\sum_{u,y} \begin{cases} \dot{\boldsymbol{x}} = [\boldsymbol{J}(\boldsymbol{x}) - \boldsymbol{R}(\boldsymbol{x})]\boldsymbol{\nabla} H(\boldsymbol{x}) + \boldsymbol{g}(\boldsymbol{x})\boldsymbol{u} + \boldsymbol{E} \\ \boldsymbol{y} = \boldsymbol{g}^\top(\boldsymbol{x})\boldsymbol{\nabla} H(\boldsymbol{x}) \end{cases} \tag{4.1.1a}$$

$$H(\boldsymbol{x}) = \frac{1}{2}\boldsymbol{x}^\top \boldsymbol{Q}\boldsymbol{x} \tag{4.1.1b}$$

All energy variables of the system are represented by the state vector $\boldsymbol{x} \in \mathbb{R}^n$. The input-port of the system is $\boldsymbol{u} \in \mathbb{R}^m$. The output of the system is $\boldsymbol{y} \in \mathbb{R}^m$. The input matrix, $\boldsymbol{g} \in \mathbb{R}^{n\times m}$, is the matrix describing the relation between the inputs and the outputs in the system. $\boldsymbol{E} \in \mathbb{R}^n$ represents the constant source vector, if any. For the derivations below, this term is neglected for illustration purposes. The interconnections related to power conservation are represented by the interconnection matrix $\boldsymbol{J} \in \mathbb{R}^{n\times n}$. This matrix is skew-symmetric, which implies that $\boldsymbol{J} = -\boldsymbol{J}^\top$. The damping and dissipation of the system are represented by the dissipation matrix $\boldsymbol{R} \in \mathbb{R}^{n\times n}$. This is a symmetric matrix, which implies that $\boldsymbol{R} = \boldsymbol{R}^\top$. It also has positive semi-definite properties, such as $\boldsymbol{R} \geq 0$. The term $[\boldsymbol{J} - \boldsymbol{R}]$ is often denoted as $\boldsymbol{F}$, i.e. $\boldsymbol{F} = [\boldsymbol{J} - \boldsymbol{R}]$. The scalar, $H(\boldsymbol{x})$, in Equation (4.1.1b) is referred to as the Hamiltonian or the stored energy in the system. $\boldsymbol{Q} \in \mathbb{R}^{n\times n}$ describes the energy storage and is a symmetric positive definite matrix: $\boldsymbol{Q} = \boldsymbol{Q}^\top > 0$. This relationship ensures $H(\boldsymbol{x}) \geq 0$. $\boldsymbol{Q}$ also occurs in the expression of the co-energy variables, $\boldsymbol{\nabla} H(\boldsymbol{x})$, where $\boldsymbol{\nabla} H(\boldsymbol{x}) = \boldsymbol{Q}\boldsymbol{x}$. The mentioned definitions of the matrices in (4.1.1) result in $\dot{H}(\boldsymbol{x}) \leq \boldsymbol{y}^\top \boldsymbol{u}$, which also is the definition of passive systems [34].

The latter point can be proven by deriving an expression for $\dot{H}(\boldsymbol{x})$. The derivative of the storage function can be written like this:

$$\dot{H}(\boldsymbol{x}) = \frac{\partial^\top H(\boldsymbol{x})}{dt} = \frac{\partial^\top H(\boldsymbol{x})}{d\boldsymbol{x}} \frac{d\boldsymbol{x}}{dt} = \boldsymbol{\nabla}^\top H(\boldsymbol{x}) \cdot \dot{\boldsymbol{x}}$$

The expression for $\dot{\boldsymbol{x}}$ from (4.1.1a) is inserted:

$$\dot{H}(\boldsymbol{x}) = \boldsymbol{\nabla}^\top H(\boldsymbol{x}) \cdot ([\boldsymbol{J}(\boldsymbol{x}) - \boldsymbol{R}(\boldsymbol{x})]\boldsymbol{\nabla} H(\boldsymbol{x}) + \boldsymbol{g}(\boldsymbol{x})\boldsymbol{u})$$

This results in the following:

$$\dot{H}(\boldsymbol{x}) = \underbrace{\boldsymbol{\nabla}^\top H(\boldsymbol{x})\boldsymbol{J}(\boldsymbol{x})\boldsymbol{\nabla}H(\boldsymbol{x})}_{\text{power preservation: } 0} \underbrace{-\boldsymbol{\nabla}^\top H(\boldsymbol{x})\boldsymbol{R}(\boldsymbol{x})\boldsymbol{\nabla}H(\boldsymbol{x})}_{\text{power dissipation: } \leq 0} + \underbrace{\boldsymbol{\nabla}^\top H(\boldsymbol{x})\boldsymbol{g}(\boldsymbol{x})}_{\text{passive output: } \boldsymbol{y}^\top} \cdot \boldsymbol{u}$$

As a skew-symmetric matrix satisfies the condition $\boldsymbol{z}^\top \boldsymbol{J}\boldsymbol{z} = 0$, the final expression for $\dot{H}(\boldsymbol{x})$ is given as follows:

$$\dot{H}(\boldsymbol{x}) = \underbrace{-\boldsymbol{\nabla}^\top H(\boldsymbol{x})\boldsymbol{R}(\boldsymbol{x})\boldsymbol{\nabla}H(\boldsymbol{x})}_{\leq 0} + \boldsymbol{y}^\top \boldsymbol{u}$$

As the positive semi-definite symmetric, $\boldsymbol{R}$, matrix satisfy the condition $\boldsymbol{z}^\top \boldsymbol{R}\boldsymbol{z} \geq 0$. As a result, the first term in the given expression is non-positive, meaning it is either negative or equal to zero. Thus, $\dot{H}(\boldsymbol{x})$ will not be any greater than the latter term $\boldsymbol{y}^\top \boldsymbol{u}$ and the following relationship is valid:

$$\dot{H}(\boldsymbol{x}) \leq \boldsymbol{y}^\top \boldsymbol{u}$$

The above point illustrates that port-Hamiltonian systems are passive and that not every system can adopt a port-Hamiltonian representation since not all systems have skew-symmetric and symmetric positive semi-definite properties in their respective interconnection and dissipation matrices [35]. This critical point will be emphasized later in this master's thesis. However, pH and passive systems can be stabilized by appropriately designing a controller based on passivity arguments. In addition, to study and prove asymptotic stability in a system, the shifted Hamiltonian function can be used as a Lyapunov candidate to evaluate if it satisfies the requirements of a Lyapunov function.

4.1.2 Lyapunov's Stability Criteria

Lyapunov's method is a mathematical approach to study the stability of a system. A *Lyapunov function* is a scalar function that often describes the total energy in a system, similar to a Hamiltonian function. However, a function, $V(x)$, is a Lyapunov function if it is continuously differentiable, if it is defined in a region that contains the origin and if it satisfies the requirements below [36]. A Lyapunov function is a powerful tool to determine the stability of a system, as it can always be associated with a stable system. Thus, if a Lyapunov function exists for a system, the system is stable. [37]

$$\underbrace{\begin{matrix} V(\bar{x}) = 0; \quad V(x) > 0 \in \mathbb{R}^n \backslash \{\bar{x}\} \\ \dot{V}(\bar{x}) = 0; \quad \dot{V}(x) < 0 \in \mathbb{R}^n \backslash \{\bar{x}\} \end{matrix}}_{\text{Global asymptotic stability}} \qquad \underbrace{\begin{matrix} V(\bar{x}) = 0; \quad V(x) > 0 \in \mathbb{R}^n \backslash \{\bar{x}\} \\ \dot{V}(\bar{x}) = 0; \quad \dot{V}(x) \leq 0 \in \mathbb{R}^n \backslash \{\bar{x}\} \end{matrix}}_{\text{Global stability}}$$

Energy will dissipate in a system when it is in motion. Thus, the derivative of the function that describes the system will be non-positive along the trajectories of the system, i.e., $\dot{V}(x) \leq 0$ [36]. This implies that the storage function $V(x)$ is non-increasing over time, and it may eventually reach the origin, which is considered the equilibrium point $\bar{\boldsymbol{x}}$ in Lyapunov's theory. If $\dot{V}(x) \leq 0 \; \forall \; x \neq \bar{x}$, it is possible that the trajectory of the system stops before it reaches the origin. However,

the origin is still considered stable [36]. The other relationship, $\dot{V}(x) < 0 \; \forall \; x \neq \bar{x}$, implies that the trajectory eventually will reach the origin; thus the equilibrium point is located at the minimum of the energy function. This is desirable since this implies that the origin is asymptotically stable and that the system converges to the equilibrium point. As noticed from the sections above, a Hamiltonian function, $H(x)$, shares some properties with a Lyapunov function. This makes it convenient to use a Hamiltonian function as a Lyapunov candidate as a starting point for finding a Lyapunov function. If the Hamiltonian function satisfies the requirements from above, it can be proven to be a Lyapunov function, which can be used to prove asymptotic stability in the system.

4.1.3 Incremental Model

The abovementioned theory implies that Lyapunov's theory can be applied to a Hamiltonian function. Thus, it is possible to analyze if the case-specific DC MG in the master's thesis is stable. However, Lyapunov's method considers the origin as the equilibrium point, i.e., $\bar{x} = 0$. This is not the desired operation point for a DC MG, as it will be out of operation. However, by shifting the system and using incremental states, Lyapunov's theory can still be applied while ensuring that the equilibrium point corresponds to the minimum of the energy function. This approach involves using the modified state variables $\tilde{x} = x - \bar{x}$, where $\bar{x}$ is the state at the minimum equilibrium point, while x is the state of the actual operating point. Since $\tilde{x} = 0$ when the actual operating point and the minimum equilibrium point correspond, i.e., $x = \bar{x}$, Lyapunov's method can be used to analyze the stability of the DC MG while ensuring that it is operating at its desired equilibrium point [38]. In this master's thesis, $\boldsymbol{J}$, $\boldsymbol{R}$ and $\boldsymbol{g}$ are constant matrices such the incremental pH representation of $\sum_{u,y}$ from (4.1.1) can be presented as in (4.1.3).

$$\tilde{\sum_{u,y}} \begin{cases} \dot{\tilde{\boldsymbol{x}}} = [\boldsymbol{J} - \boldsymbol{R}]\boldsymbol{\nabla} V(\tilde{\boldsymbol{x}}) + \boldsymbol{g}\tilde{\boldsymbol{u}} \\ \tilde{\boldsymbol{y}} = \boldsymbol{g}^\top \boldsymbol{\nabla} V(\tilde{\boldsymbol{x}}) \end{cases} \tag{4.1.3a}$$

$$V(\tilde{\boldsymbol{x}}) = \frac{1}{2}\tilde{\boldsymbol{x}}^\top \boldsymbol{Q}\tilde{\boldsymbol{x}} \tag{4.1.3b}$$

It should be noted that the constant source vector, $\boldsymbol{E}$, from (4.1.1a) disappear due to the following relationship $\tilde{\boldsymbol{x}} = \dot{\boldsymbol{x}} - \dot{\bar{\boldsymbol{x}}} = (\boldsymbol{a}\boldsymbol{x} + \boldsymbol{b}) - (\boldsymbol{a}\bar{\boldsymbol{x}} + \boldsymbol{b}) = \boldsymbol{a}\tilde{\boldsymbol{x}}$.

4.2 Energy Modeling of the Electrical Network

As previously mentioned, a system must satisfy specific criteria to qualify as a port-Hamiltonian system. In particular, the system must be passive with respect to both the input-output mapping and the output. This implies that the matrices in (4.1.1a) need to have specific properties as described above.

When the port-Hamiltonian representation of the case-specific electrical network, $\sum_p$, is obtained, the ODEs from (2.1.3) needs to be rewritten in matrix notation. These equations were expressed in actual values with dimensions. However, in order to incorporate the controller and verify proportional current-sharing, it is necessary to express the current in its utilization ratio. This ratio is the current ratio in per-unit, denoted as $I^{\mathcal{G}}_{i,\text{pu}}$ in this thesis. The ratio describes how much each generator contributes to the current in the system relative to its maximum capacity. Accordingly, the state variable representing the current is expressed in per-unit values, while the remaining state variables in the physical system are expressed in actual values. This approach facilitates accurate

modeling of the physical behavior of the DC MG and enables the implementation of control in the cyber layer. The relationship between the actual value and the rated current of each converter is given by $I^{\mathcal{G}}_{i,\text{pu}} = I^{\mathcal{G}}_{i} / I^{\mathcal{G}}_{i,\text{rated}}$.

In matrix notation, this results in $\boldsymbol{I}^{\mathcal{G}}_{\text{pu}} = \text{blockdiag}^{-1}\{\boldsymbol{I}^{\mathcal{G}}_{\text{rated}}\}\boldsymbol{I}^{\mathcal{G}}$. Furthermore, the actual value of the current can be represented as $\boldsymbol{I}^{\mathcal{G}} = \text{blockdiag}\{\boldsymbol{I}^{\mathcal{G}}_{\text{rated}}\}\boldsymbol{I}^{\mathcal{G}}_{\text{pu}}$. This expression will be substituted into the system of equations in (2.1.3). To reduce the complexity of the equations, vectors and matrices that were previously multiplied by the actual generator current will now be multiplied by $\text{blockdiag}\{\boldsymbol{I}^{\mathcal{G}}_{\text{rated}}\}$. This results in $\boldsymbol{L}^{\mathcal{G}}_{*} = \boldsymbol{L}^{\mathcal{G}} \cdot \text{blockdiag}\{\boldsymbol{I}^{\mathcal{G}}_{\text{rated}}\}$, $\boldsymbol{R}^{\mathcal{G}}_{*} = \boldsymbol{R}^{\mathcal{G}} \cdot \text{blockdiag}\{\boldsymbol{I}^{\mathcal{G}}_{\text{rated}}\}$ and $\boldsymbol{\mathcal{B}}^{\mathcal{G}}_{*} = \boldsymbol{\mathcal{B}}^{\mathcal{G}} \cdot \text{blockdiag}\{\boldsymbol{I}^{\mathcal{G}}_{\text{rated}}\}$. It can be noted that the adjusted incidence matrix is a block diagonal matrix of the rated currents, i.e., $\boldsymbol{\mathcal{B}}^{\mathcal{G}}_{*} = \text{blockdiag}\{\boldsymbol{I}^{\mathcal{G}}_{\text{rated}}\}$. This relation can be derived from the fact that the original incidence matrix is a diagonal matrix with all its elements equal to one. These substitutions result in (4.2.1), which is the updated representation of the differential equations from (2.1.3) written on matrix notation. Furthermore, V_{nom} is multiplied by the column vector of ones, $\mathbf{1} = \text{col}(1) \in \mathbb{R}^{n^{\mathcal{G}_i}}$, since it is a constant that appears in every vector element. Introducing the system equations in matrix notation is an advantage when analyzing the stability and steady state conditions of the system. It can also be seen that the incidence matrices obtained with graph theory, $\boldsymbol{\mathcal{B}}^{\mathcal{G}}$ and $\boldsymbol{\mathcal{B}}^{\mathcal{E}}$ can be directly incorporated in the representation of the system.

$$\boldsymbol{L}^{\mathcal{G}}_{*}\dot{\boldsymbol{I}}^{\mathcal{G}}_{\text{pu}} = \mathbf{1}V_{\text{nom}} + \boldsymbol{u}_p - \boldsymbol{\mathcal{B}}^{\mathcal{G}^\top}\boldsymbol{V}^{\mathcal{N}} - \boldsymbol{R}^{\mathcal{G}}_{*}\boldsymbol{I}^{\mathcal{G}}_{\text{pu}} \tag{4.2.1a}$$

$$\boldsymbol{L}^{\mathcal{E}}\dot{\boldsymbol{I}}^{\mathcal{E}} = -\boldsymbol{\mathcal{B}}^{\mathcal{E}^\top}\boldsymbol{V}^{\mathcal{N}} - \boldsymbol{R}^{\mathcal{E}}\boldsymbol{I}^{\mathcal{E}} \tag{4.2.1b}$$

$$\boldsymbol{C}^{\mathcal{N}}\dot{\boldsymbol{V}}^{\mathcal{N}} = \boldsymbol{\mathcal{B}}^{\mathcal{E}}\boldsymbol{I}^{\mathcal{E}} + \boldsymbol{\mathcal{B}}^{\mathcal{G}}_{*}\boldsymbol{I}^{\mathcal{G}}_{\text{pu}} - \boldsymbol{G}^{\mathcal{N}}_{\text{cte}}\boldsymbol{V}^{\mathcal{N}} - \boldsymbol{I}_{\text{cte}} \tag{4.2.1c}$$

However, the substitution in (4.2.1) removes the skew-symmetric properties of the system, because $\boldsymbol{\mathcal{B}}^{\mathcal{G}}_{*} \neq \boldsymbol{\mathcal{B}}^{\mathcal{G}}$. To provide the skew-symmetry, equations (4.2.1b) and (4.2.1c) are multiplied by $\text{blockdiag}^{-1}\{\boldsymbol{I}^{\mathcal{G}}_{\text{rated}}\}$ such that the term multiplied by $\boldsymbol{I}^{\mathcal{G}}_{\text{pu}}$ in (4.2.1c) gets back to being $\boldsymbol{\mathcal{B}}^{\mathcal{G}}$. This results in $\boldsymbol{L}^{\mathcal{E}}_{*} = \boldsymbol{L}^{\mathcal{E}} \cdot \text{blockdiag}^{-1}\{\boldsymbol{I}^{\mathcal{G}}_{\text{rated}}\}$, $\boldsymbol{\mathcal{B}}^{\mathcal{E}^\top}_{*} = \boldsymbol{\mathcal{B}}^{\mathcal{E}^\top} \cdot \text{blockdiag}^{-1}\{\boldsymbol{I}^{\mathcal{G}}_{\text{rated}}\}$, $\boldsymbol{R}^{\mathcal{E}}_{*} = \boldsymbol{R}^{\mathcal{E}} \cdot \text{blockdiag}^{-1}\{\boldsymbol{I}^{\mathcal{G}}_{\text{rated}}\}$, $\boldsymbol{C}^{\mathcal{N}}_{*} = \boldsymbol{C}^{\mathcal{N}} \cdot \text{blockdiag}^{-1}\{\boldsymbol{I}^{\mathcal{G}}_{\text{rated}}\}$, $\boldsymbol{\mathcal{B}}^{\mathcal{E}}_{*} = \boldsymbol{\mathcal{B}}^{\mathcal{E}} \cdot \text{blockdiag}^{-1}\{\boldsymbol{I}^{\mathcal{G}}_{\text{rated}}\}$, $\boldsymbol{G}^{\mathcal{N}}_{*,\text{cte}} = \boldsymbol{G}^{\mathcal{N}}_{\text{cte}} \cdot \text{blockdiag}^{-1}\{\boldsymbol{I}^{\mathcal{G}}_{\text{rated}}\}$ and $\boldsymbol{I}_{*,\text{cte}} = \boldsymbol{I}_{\text{cte}} \cdot \text{blockdiag}^{-1}\{\boldsymbol{I}^{\mathcal{G}}_{\text{rated}}\}$ as shown below in (4.2.2). Consequently, the skew-symmetry in this representation is provided by $\boldsymbol{\mathcal{B}}^{\mathcal{E}}_{*} = -\boldsymbol{\mathcal{B}}^{\mathcal{E}^\top}_{*}$ and $\boldsymbol{\mathcal{B}}^{\mathcal{G}} = -\boldsymbol{\mathcal{B}}^{\mathcal{G}^\top}$.

$$\boldsymbol{L}^{\mathcal{G}}_{*}\dot{\boldsymbol{I}}^{\mathcal{G}}_{\text{pu}} = \mathbf{1}V_{\text{nom}} + \boldsymbol{u}_p - \boldsymbol{\mathcal{B}}^{\mathcal{G}^\top}\boldsymbol{V}^{\mathcal{N}} - \boldsymbol{R}^{\mathcal{G}}_{*}\boldsymbol{I}^{\mathcal{G}}_{\text{pu}} \tag{4.2.2a}$$

$$\boldsymbol{L}^{\mathcal{E}}_{*}\dot{\boldsymbol{I}}^{\mathcal{E}} = -\boldsymbol{\mathcal{B}}^{\mathcal{E}^\top}_{*}\boldsymbol{V}^{\mathcal{N}} - \boldsymbol{R}^{\mathcal{E}}_{*}\boldsymbol{I}^{\mathcal{E}} \tag{4.2.2b}$$

$$\boldsymbol{C}^{\mathcal{N}}_{*}\dot{\boldsymbol{V}}^{\mathcal{N}} = \boldsymbol{\mathcal{B}}^{\mathcal{E}}_{*}\boldsymbol{I}^{\mathcal{E}} + \boldsymbol{\mathcal{B}}^{\mathcal{G}}\boldsymbol{I}^{\mathcal{G}}_{\text{pu}} - \boldsymbol{G}^{\mathcal{N}}_{*,\text{cte}}\boldsymbol{V}^{\mathcal{N}} - \boldsymbol{I}_{*,\text{cte}} \tag{4.2.2c}$$

Eventually, the pH representation of the electrical network can be expressed as below in (4.2.3).

$$\underbrace{\begin{bmatrix} \boldsymbol{L}^{\mathcal{G}}_{*}\dot{\boldsymbol{I}}^{\mathcal{G}}_{\text{pu}} \\ \boldsymbol{L}^{\mathcal{E}}_{*}\dot{\boldsymbol{I}}^{\mathcal{E}} \\ \boldsymbol{C}^{\mathcal{N}}_{*}\dot{\boldsymbol{V}}^{\mathcal{N}} \end{bmatrix}}_{\dot{\boldsymbol{x}}_p} = \underbrace{\begin{bmatrix} -\boldsymbol{R}^{\mathcal{G}}_{*} & \mathbf{0} & -\boldsymbol{\mathcal{B}}^{\mathcal{G}^\top} \\ \mathbf{0} & -\boldsymbol{R}^{\mathcal{E}}_{*} & -\boldsymbol{\mathcal{B}}^{\mathcal{E}^\top}_{*} \\ \boldsymbol{\mathcal{B}}^{\mathcal{G}} & \boldsymbol{\mathcal{B}}^{\mathcal{E}}_{*} & -\boldsymbol{G}^{\mathcal{N}}_{*,\text{cte}} \end{bmatrix}}_{\boldsymbol{F}_p} \underbrace{\begin{bmatrix} \boldsymbol{I}^{\mathcal{G}}_{\text{pu}} \\ \boldsymbol{I}^{\mathcal{E}} \\ \boldsymbol{V}^{\mathcal{N}} \end{bmatrix}}_{\nabla H_p(\boldsymbol{x}_p)} + \underbrace{\begin{bmatrix} \boldsymbol{\mathcal{I}}^{\mathcal{G}} \\ \mathbf{0} \\ \mathbf{0} \end{bmatrix}}_{\boldsymbol{g}_p} \boldsymbol{u}_p + \underbrace{\begin{bmatrix} \mathbf{1}V_{\text{nom}} \\ \mathbf{0} \\ -\boldsymbol{I}_{*,\text{cte}} \end{bmatrix}}_{\boldsymbol{E}_p} \tag{4.2.3}$$

The state vector containing the energy variables is defined as the column vector, $\boldsymbol{x}_p \in \mathbb{R}^{n^{\mathcal{G}}_i + n^{\mathcal{E}}_j + n^{\mathcal{N}}_k}$,

i.e. $\boldsymbol{x}_p \in \mathbb{R}^{13} : \boldsymbol{\Phi}_*^{\mathcal{G}} \in \mathbb{R}^4, \boldsymbol{\Phi}_*^{\mathcal{E}} \in \mathbb{R}^5, \boldsymbol{q}_*^{\mathcal{N}} \in \mathbb{R}^4$ for the case-specific DC MG. $\boldsymbol{x}_p$ consists of the flux linkages in the generators and transmission lines, as well as the charges of the loads, due to the correlations of $\Phi = LI$ and $q = CV$:

$$\boldsymbol{x}_p := \begin{bmatrix} \boldsymbol{\Phi}_*^{\mathcal{G}} \\ \boldsymbol{\Phi}_*^{\mathcal{E}} \\ \boldsymbol{q}_*^{\mathcal{N}} \end{bmatrix}$$

The input matrix $\boldsymbol{g}_p \in \mathbb{R}^{\left(n_i^{\mathcal{G}} + n_j^{\mathcal{E}} + n_k^{\mathcal{N}}\right) \times n_i^{\mathcal{G}}}$ is structured such that the upper portion consists of the identity matrix, $\boldsymbol{\mathcal{I}}^{\mathcal{G}} \in \mathbb{R}^{n^{\mathcal{G}_i} \times n^{\mathcal{G}_i}}$, and the remaining entries are zeros, $\mathbf{0} \in \mathbb{R}^{n_j^{\mathcal{E}} \times n_i^{\mathcal{G}}}$ and $\mathbf{0} \in \mathbb{R}^{n_k^{\mathcal{N}} \times n_i^{\mathcal{G}}}$. This is because the control input is only present in the equations corresponding to the voltages of the DGs. To ensure the dimensions in the equations add up, $\boldsymbol{u}_p$ is multiplied by the identity matrix. The input matrix is in the form presented below:

$$\boldsymbol{g}_p := \begin{bmatrix} \boldsymbol{\mathcal{I}}^{\mathcal{G}} \\ \mathbf{0} \\ \mathbf{0} \end{bmatrix}$$

$\boldsymbol{E}_p \in \mathbb{R}^{n_i^{\mathcal{G}} + n_j^{\mathcal{E}} + n_k^{\mathcal{N}}}$ contains the constant terms and is defined below, where $\mathbf{1} \in \mathbb{R}^4, \mathbf{0} \in \mathbb{R}^5, \boldsymbol{I}_{*,\text{cte}} \in \mathbb{R}^4$:

$$\boldsymbol{E}_p := \begin{bmatrix} \mathbf{1} V_{\text{nom}} \\ \mathbf{0} \\ -\boldsymbol{I}_{*,\text{cte}} \end{bmatrix}$$

The interconnection matrix $\boldsymbol{J}_p \in \mathbb{R}^{13 \times 13}$ describes how the three subsystems are interconnected and contain the incidence matrices of *Graph 1* and *Graph 2*. The dissipation matrix $\boldsymbol{R}_p \in \mathbb{R}^{13 \times 13}$ consists of the electrical dissipation. $\boldsymbol{F}_p$ has the same dimensions as the two other matrices:

$$\boldsymbol{J}_p := \begin{bmatrix} \mathbf{0} & \mathbf{0} & -\boldsymbol{\mathcal{B}}^{\mathcal{G}\top} \\ \mathbf{0} & \mathbf{0} & -\boldsymbol{\mathcal{B}}_*^{\mathcal{E}\top} \\ \boldsymbol{\mathcal{B}}^{\mathcal{G}} & \boldsymbol{\mathcal{B}}_*^{\mathcal{E}} & \mathbf{0} \end{bmatrix} \qquad \boldsymbol{R}_p := \begin{bmatrix} \boldsymbol{R}_*^{\mathcal{G}} & \mathbf{0} & \mathbf{0} \\ \mathbf{0} & \boldsymbol{R}_*^{\mathcal{E}} & \mathbf{0} \\ \mathbf{0} & \mathbf{0} & \boldsymbol{G}_{*,\text{cte}}^{\mathcal{N}} \end{bmatrix} \qquad \boldsymbol{F}_p := \begin{bmatrix} -\boldsymbol{R}_*^{\mathcal{G}} & \mathbf{0} & -\boldsymbol{\mathcal{B}}^{\mathcal{G}\top} \\ \mathbf{0} & -\boldsymbol{R}_*^{\mathcal{E}} & -\boldsymbol{\mathcal{B}}_*^{\mathcal{E}\top} \\ \boldsymbol{\mathcal{B}}^{\mathcal{G}} & \boldsymbol{\mathcal{B}}_*^{\mathcal{E}} & -\boldsymbol{G}_{*,\text{cte}}^{\mathcal{N}} \end{bmatrix}$$

$\boldsymbol{\nabla} H_p(\boldsymbol{x}_p) \in \mathbb{R}^{13}$ is the co-energy variables consisting of the currents in the DGs and transmission lines respectively, and the voltages at the loads. $\boldsymbol{Q}_p \in \mathbb{R}^{13 \times 13}$ consist of the inverse of the inductance in the DGs and transmission lines and the inverse of the capacitance of the loads.

$$\boldsymbol{\nabla} H_p(\boldsymbol{x}) := \begin{bmatrix} \boldsymbol{I}_{\text{pu}}^{\mathcal{G}} \\ \boldsymbol{I}^{\mathcal{E}} \\ \boldsymbol{V}^{\mathcal{N}} \end{bmatrix} \qquad \boldsymbol{Q}_p := \begin{bmatrix} (\boldsymbol{L}_*^{\mathcal{G}})^{-1} & \mathbf{0} & \mathbf{0} \\ \mathbf{0} & (\boldsymbol{L}_*^{\mathcal{E}})^{-1} & \mathbf{0} \\ \mathbf{0} & \mathbf{0} & (\boldsymbol{C}_*^{\mathcal{N}})^{-1} \end{bmatrix}$$

The definitions above clearly show that the physical DC MG admits to a pH representation. This is due to the skew-symmetry of $\boldsymbol{J}_p = -\boldsymbol{J}_p^\top$, and the symmetrical positive definiteness of $\boldsymbol{R}_p = \boldsymbol{R}_p^\top$, which also ensures $\dot{H}_p(\boldsymbol{x}_p) \leq \boldsymbol{y}_p^\top \boldsymbol{u}_p$ and the definition of a passive system. To summarize, the port-Hamiltonian representation, $\sum_p$, together with the Hamiltonian function, $H_p(\boldsymbol{x}_p)$, of the physical system can be expressed as follows in (4.2.4a).

$$\sum_p \begin{cases} \dot{\boldsymbol{x}}_p = \boldsymbol{F}_p \boldsymbol{\nabla} H_p(\boldsymbol{x}_p) + \boldsymbol{g}_p \boldsymbol{u}_p + \boldsymbol{E}_p \\ \boldsymbol{y}_p = \boldsymbol{g}_p^\top \boldsymbol{\nabla} H_p(\boldsymbol{x}_p) \end{cases} \tag{4.2.4a}$$

$$H_p(\boldsymbol{x}_p) = \frac{1}{2} {\boldsymbol{x}_p}^\top \boldsymbol{Q}_p \boldsymbol{x}_p \tag{4.2.4b}$$

The passive output is defined as $\boldsymbol{y} = \boldsymbol{g}^\top \boldsymbol{\nabla} H = \boldsymbol{g}^\top \boldsymbol{Q} \boldsymbol{x}$, from the definition of a pH system given in section 4.1.1. In the physical network, the output port is proven to be $\boldsymbol{y}_p = \boldsymbol{I}^{\mathcal{G}}_{\text{pu}}$ as in (4.2.5) below.

$$\begin{aligned} \boldsymbol{y}_p &= \boldsymbol{g}_p^\top \boldsymbol{Q}_p \boldsymbol{x}_p \\ &= \begin{bmatrix} \boldsymbol{\mathcal{I}}^{\mathcal{G}} & \boldsymbol{0} & \boldsymbol{0} \end{bmatrix} \begin{bmatrix} (\boldsymbol{L}^{\mathcal{G}}_*)^{-1} & \boldsymbol{0} & \boldsymbol{0} \\ \boldsymbol{0} & (\boldsymbol{L}^{\mathcal{E}}{}_*)^{-1} & \boldsymbol{0} \\ \boldsymbol{0} & \boldsymbol{0} & (\boldsymbol{C}^{\mathcal{N}}{}_*)^{-1} \end{bmatrix} \begin{bmatrix} \boldsymbol{L}^{\mathcal{G}}_* \boldsymbol{I}^{\mathcal{G}}_{\text{pu}} \\ \boldsymbol{L}^{\mathcal{E}}_* \boldsymbol{I}^{\mathcal{E}} \\ \boldsymbol{C}^{\mathcal{N}}_* \boldsymbol{V}^{\mathcal{N}} \end{bmatrix} \\ &= \begin{bmatrix} \boldsymbol{\mathcal{I}}^{\mathcal{G}}_{\text{pu}} (\boldsymbol{L}^{\mathcal{G}}_*)^{-1} & \boldsymbol{0} & \boldsymbol{0} \end{bmatrix} \begin{bmatrix} \boldsymbol{L}^{\mathcal{G}}_* \boldsymbol{I}^{\mathcal{G}}_{\text{pu}} \\ \boldsymbol{L}^{\mathcal{E}}_* \boldsymbol{I}^{\mathcal{E}} \\ \boldsymbol{C}^{\mathcal{N}}_* \boldsymbol{V}^{\mathcal{N}} \end{bmatrix} \\ &= \boldsymbol{\mathcal{I}}^{\mathcal{G}} \boldsymbol{I}^{\mathcal{G}}_{\text{pu}} = \boldsymbol{I}^{\mathcal{G}}_{\text{pu}} \end{aligned} \tag{4.2.5}$$

Furthermore, the incremental Hamiltonian function can be used as a Lyapunov candidate to analyze if the system is asymptotically stable, as explained in section 4.1.2. The incremental pH representation of the system is given as below in (4.2.6) where $V_p(\tilde{\boldsymbol{x}}_p) = H_p(\tilde{\boldsymbol{x}}_p)$ represents the Hamiltonian function of the incremental model of the physical layer. $\tilde{\boldsymbol{u}}_p$ is the unknown input, and $\tilde{\boldsymbol{y}}_p = \tilde{\mathbf{I}}^{\mathcal{G}}_{\text{pu}}$ is the passive output of the incremental model.

$$\tilde{\sum_p} \begin{cases} \dot{\tilde{\boldsymbol{x}}}_p = \boldsymbol{F}_p \boldsymbol{\nabla} V_p(\tilde{\boldsymbol{x}}_p) + \boldsymbol{g}_p \tilde{\boldsymbol{u}}_p \\ \tilde{\boldsymbol{y}}_p = \boldsymbol{g}_p^\top \boldsymbol{\nabla} V_p(\tilde{\boldsymbol{x}}_p) \end{cases} \tag{4.2.6a}$$

$$V_p(\tilde{\boldsymbol{x}}_p) = \frac{1}{2} \tilde{\boldsymbol{x}}_p^\top \boldsymbol{Q}_p \tilde{\boldsymbol{x}}_p \tag{4.2.6b}$$

The following relationship is valid: $V_p(\tilde{\boldsymbol{x}}) > 0$, since $\boldsymbol{Q}_p$ is proven to be a positive definite matrix consisting of only the inverse of stored inductance and capacitance. As explained in section 4.1.1, the derivative of the storage function is on the shape given below because the physical network admits to a pH representation.

$$\begin{aligned} \dot{V}_p(\tilde{\boldsymbol{x}}_p) =& \underbrace{-\boldsymbol{\nabla}^\top V_p(\boldsymbol{x}_p) \boldsymbol{R}_p \boldsymbol{\nabla} V_p(\boldsymbol{x}_p) + \boldsymbol{y}_p^\top \boldsymbol{u}_p + \boldsymbol{\nabla}^\top V_p(\boldsymbol{x}_p) \boldsymbol{E}_p}_{\dot{V}_p(\boldsymbol{x}_p)} \\ & - \underbrace{\left(-\boldsymbol{\nabla}^\top V_p(\bar{\boldsymbol{x}}_p) \boldsymbol{R}_p \boldsymbol{\nabla} V_p(\bar{\boldsymbol{x}}_p) + \bar{\boldsymbol{y}}_p^\top \bar{\boldsymbol{u}}_p + \boldsymbol{\nabla}^\top V_p(\bar{\boldsymbol{x}}_p) \boldsymbol{E}_p \right)}_{\dot{V}_p(\bar{\boldsymbol{x}}_p)} \\ =& - \boldsymbol{\nabla}^\top V_p(\tilde{\boldsymbol{x}}_p) \boldsymbol{R}_p \boldsymbol{\nabla} V(\tilde{\boldsymbol{x}}_p) + \tilde{\boldsymbol{y}}_p^\top \tilde{\boldsymbol{u}}_p \end{aligned} \tag{4.2.7a}$$

The constant terms disappear in the incremental model, and it is evident that $\dot{V}_p(\tilde{\boldsymbol{x}}_p) \leq \tilde{\boldsymbol{y}}_p^\top \tilde{\boldsymbol{u}}_p$ and that the incremental model of the system is passive. Thus, the physical network is ready to be connected to a suitable controller.

4.3 Energy Modeling of the Distributed Control Network

As mentioned in the previous section 3.2, the states of the distributed network are $\boldsymbol{x}_c = [\boldsymbol{\zeta}, \boldsymbol{\lambda}]^\top$. According to the equations (3.2.4) presented in [1], the input of the cyber layer has to be the load-ratio at each DG, i.e., $\boldsymbol{u}_c = \boldsymbol{y}_p = \boldsymbol{I}_{\text{pu}}^{\mathcal{G}}$. This relation will also be derived in the subsequent section 4.4.1. The equations in (3.3.1) can be rewritten as below in (4.3.1) to illustrate that the distributed control network can admit to a pH representation.

$$\dot{\boldsymbol{\zeta}} = -\boldsymbol{\mathcal{L}}\boldsymbol{K}_I\boldsymbol{\lambda} \tag{4.3.1a}$$

$$\dot{\boldsymbol{\lambda}} = \boldsymbol{\mathcal{L}}\boldsymbol{K}_y\boldsymbol{\zeta} - \boldsymbol{K}_y\boldsymbol{K}_I^{-1}\boldsymbol{K}_I\boldsymbol{\lambda} - \boldsymbol{\mathcal{L}}\boldsymbol{K}_P\boldsymbol{K}_I^{-1}\boldsymbol{K}_I\boldsymbol{\lambda} + \boldsymbol{K}_y\boldsymbol{u}_c \tag{4.3.1b}$$

Furthermore, this can be represented in matrix notation as in (4.3.2), where $\boldsymbol{x}_c \in \mathbb{R}^{n_i^{\mathcal{G}}+n_i^{\mathcal{G}}}$, i.e. $\boldsymbol{x}_c \in \mathbb{R}^8 : \boldsymbol{\zeta} \in \mathbb{R}^4, \boldsymbol{\lambda} \in \mathbb{R}^4$ for the case-spesific DC MG. The Laplacian matrix and the matrices corresponding to the gains are as mentioned earlier in section 2.2 and section 3.3.

$$\underbrace{\begin{bmatrix}\dot{\boldsymbol{\zeta}}\\ \dot{\boldsymbol{\lambda}}\end{bmatrix}}_{\dot{\boldsymbol{x}}_c} = \underbrace{\begin{bmatrix}\boldsymbol{0} & -\boldsymbol{\mathcal{L}}\\ \boldsymbol{\mathcal{L}} & -\left(\boldsymbol{K}_y + \boldsymbol{\mathcal{L}}\boldsymbol{K}_P\right)\boldsymbol{K}_I^{-1}\end{bmatrix}}_{\boldsymbol{F}_c} \underbrace{\begin{bmatrix}\boldsymbol{K}_y\boldsymbol{\zeta}\\ \boldsymbol{K}_I\boldsymbol{\lambda}\end{bmatrix}}_{\boldsymbol{\nabla}H_c(\boldsymbol{x}_c)} + \underbrace{\begin{bmatrix}\boldsymbol{0}\\ \boldsymbol{K}_y\end{bmatrix}}_{\boldsymbol{g}_c}\boldsymbol{u}_c \tag{4.3.2}$$

When equation (4.3.2) is represented like this, it is convenient to check if the distributed control network admits to a pH representation. As seen in the underbraces of (4.3.2), the ODEs of (4.3.1) are represented using pH formalism. In this representation, it can be stated that there are no constant sources in the system since $\boldsymbol{E}_c$ is not represented. It can also be stated that $\boldsymbol{J}_c$ is given by the Laplacian matrix of the distributed network and that $\boldsymbol{R}_c$ is represented by the positive gains and the Laplacian matrix.

$$\boldsymbol{J}_c := \begin{bmatrix}\boldsymbol{0} & -\boldsymbol{\mathcal{L}}\\ \boldsymbol{\mathcal{L}} & \boldsymbol{0}\end{bmatrix} \qquad \boldsymbol{R}_c := \begin{bmatrix}\boldsymbol{0} & \boldsymbol{0}\\ \boldsymbol{0} & -\left(\boldsymbol{K}_y + \boldsymbol{\mathcal{L}}\boldsymbol{K}_P\right)\boldsymbol{K}_I^{-1}\end{bmatrix}$$

As seen by the shape of these matrices, $\boldsymbol{J}_c$ is a skew-symmetric matrix, and $\boldsymbol{R}_c$ is a symmetrical positive semi-definite matrix, which agrees with the definitions of these matrices from the pH formalism. $\boldsymbol{\nabla}H_c(\boldsymbol{x}_c) = \boldsymbol{Q}_c\boldsymbol{x}_c$, thus it is noticeable from (4.3.2) that $\boldsymbol{Q}_c$ given below is a symmetric positive matrix consisting of the positive gains.

$$\boldsymbol{Q}_c := \begin{bmatrix}\boldsymbol{K}_y & \boldsymbol{0}\\ \boldsymbol{0} & \boldsymbol{K}_I\end{bmatrix}$$

As explained above, the distributed control network admits to a pH formulation. Thus, the matrices above ensures $\dot{H}_c(\boldsymbol{x}_c) \leq \boldsymbol{y}_c^\top\boldsymbol{u}_c$ and the definition of a passive system. To summarize, the port-Hamiltonian representation, $\sum_c$, together with the Hamiltonian function, $H_c(\boldsymbol{x}_c)$, of the physical system can be expressed as follows in (4.3.3a).

$$\sum_c \begin{cases}\dot{\boldsymbol{x}}_c = \boldsymbol{F}_c\boldsymbol{\nabla}H_c(\boldsymbol{x}_c) + \boldsymbol{g}_c\boldsymbol{u}_c\\ \boldsymbol{y}_c = \boldsymbol{g}_c^\top\boldsymbol{\nabla}H_c(\boldsymbol{x}_c)\end{cases} \tag{4.3.3a}$$

$$H_c(\boldsymbol{x}_c) = \frac{1}{2}\boldsymbol{x}_c{}^\top\boldsymbol{Q}_c\boldsymbol{x}_c \tag{4.3.3b}$$

In the physical network, the output port is proven to be $\boldsymbol{y}_c = \boldsymbol{K}_y \boldsymbol{K}_I \boldsymbol{\lambda}$ as in (4.3.4) below.

$$\begin{aligned} \boldsymbol{y}_c &= \boldsymbol{g}_c^\top \boldsymbol{Q}_c \, \boldsymbol{x}_c \\ &= \begin{bmatrix} \boldsymbol{0} & \boldsymbol{K}_y \end{bmatrix} \begin{bmatrix} \boldsymbol{K}_y & \boldsymbol{0} \\ \boldsymbol{0} & \boldsymbol{K}_I \end{bmatrix} \begin{bmatrix} \boldsymbol{\zeta} \\ \boldsymbol{\lambda} \end{bmatrix} \\ &= \begin{bmatrix} \boldsymbol{0} & \boldsymbol{K}_y \boldsymbol{K}_I \end{bmatrix} \begin{bmatrix} \boldsymbol{\zeta} \\ \boldsymbol{\lambda} \end{bmatrix} \\ &= \boldsymbol{K}_y \boldsymbol{K}_I \boldsymbol{\lambda} \end{aligned} \tag{4.3.4}$$

The incremental pH representation of the distributed control network is obtained below in (4.3.5b), where $V_c(\tilde{\boldsymbol{x}}_c) = H_c(\tilde{\boldsymbol{x}}_c)$ is chosen as the Lyapunov candidate. The input and the passive output of the incremental model of the system are $\tilde{\boldsymbol{u}}_c = \boldsymbol{\mathcal{I}}^{\mathcal{G}} \tilde{\mathbf{I}}_{\text{pu}}^{\mathcal{G}}$ and $\tilde{\boldsymbol{y}}_c = \boldsymbol{K}_y \boldsymbol{K}_I \tilde{\boldsymbol{\lambda}}$ respectively.

$$\sum_{\tilde{c}} \begin{cases} \dot{\tilde{\boldsymbol{x}}}_c = \boldsymbol{F}_c \boldsymbol{\nabla} V_c(\tilde{\boldsymbol{x}}_c) + \boldsymbol{g}_c \tilde{\boldsymbol{u}}_c \\ \tilde{\boldsymbol{y}}_c = \boldsymbol{g}_c^\top \boldsymbol{\nabla} V_c(\tilde{\boldsymbol{x}}_c) \end{cases} \tag{4.3.5a}$$

$$V_c(\tilde{\boldsymbol{x}}_c) = \frac{1}{2} \tilde{\boldsymbol{x}}_c^\top \boldsymbol{Q}_c \tilde{\boldsymbol{x}}_c \tag{4.3.5b}$$

Furthermore, the incremental Hamiltonian function can be used as a Lyapunov candidate, as explained for the physical system in section 4.2.

$$\dot{V}_c(\tilde{\boldsymbol{x}}_c) = -\boldsymbol{\nabla}^\top V_c(\tilde{\boldsymbol{x}}_c) \boldsymbol{R}_c \boldsymbol{\nabla} V(\tilde{\boldsymbol{x}}_c) + \tilde{\boldsymbol{y}}_c^\top \tilde{\boldsymbol{u}}_c \tag{4.3.6}$$

Since $\boldsymbol{Q}_c$ is proven to be a positive definite matrix and $V_c(\tilde{\boldsymbol{x}}_c) > 0$. It is also evident that $\dot{V}_c(\tilde{\boldsymbol{x}}_c) \leq \tilde{\boldsymbol{y}}_c^\top \tilde{\boldsymbol{u}}_c$ and that the incremental model of the system is passive. Thus, the distributed control network is ready to be connected to the physical layer.

4.4 Analyzing the Structure of the Combined Network

As previously mentioned, the cyber-physical DC MG consists of two layers - the physical layer and the cyber layer. The sections above demonstrated that the physical and cyber layers admitted to a pH representation when analyzed separately. However, when conducting an energy analysis of the entire system, it is convenient to partition the system into one additional part. In this approach, the regulator state, $\boldsymbol{v}$, from (3.2.1b) constitutes the third part of the system. The regulator state is an expression of both a physical state, $\boldsymbol{I}_{\text{pu}}^{\mathcal{G}}$, and a cyber state, $\boldsymbol{\lambda}$. Thus, the regulator state is at the interface of the two layers with the primary objective of driving the current ratios equal to the set point. The equations that constitute the cyber-physical MG are summarized in Figure 4.1 to provide an understanding of the combined system. As depicted in the figure, the physical layer calculates the current ratios, which are then employed in the equations of the regulator and cyber layer. Conversely, the set points are calculated in the cyber layer and utilized in the regulator. Lastly, the regulator state is calculated within the regulator equation and serves as input in the physical layer, where $\omega(\boldsymbol{v})$ represents the passive input either with or without the hyperbolic tangent function.

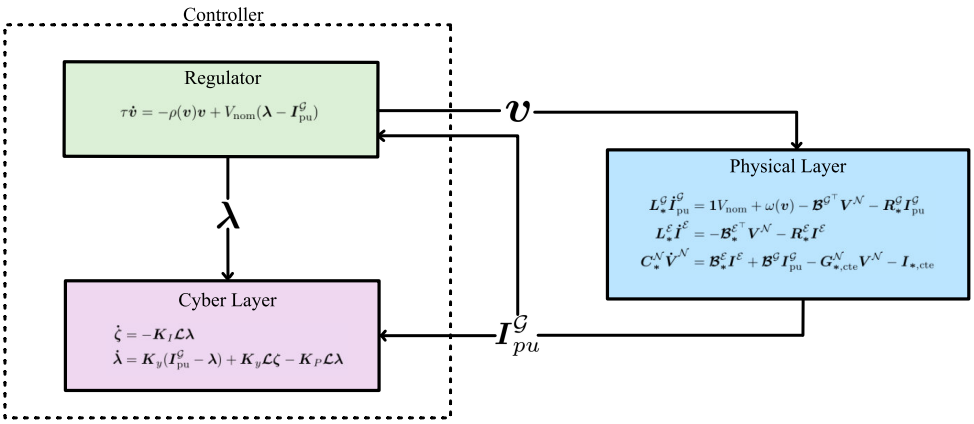

Figure 4.1: Structured representation of the system equations.

Furthermore, as addressed in the specialization project [24] and Appendix A.3, obtaining a pH representation of the CP DC MG with the regulator state and both layers connected is a complex procedure. These challenges arise even in the linear system, i.e., in the absence of the non-linearities in the controller. For this reason, the voltage saturation and leakage coefficient will be neglected in the energy analysis in this master's thesis. The presence of a state variable that is a function of a hyperbolic tangent function makes it even more challenging to obtain a pH representation of the system. Consequently, the initial and apparent step is to exclude these non-linearities and identify what specific elements of the total cyber-physical DC MG contribute to the challenges in obtaining the pH representation.

4.4.1 Analyzing the Interconnection of the Cyber and Physical Layers

Initially, an attempt to interconnect the cyber and physical layers will be made. When two pH systems are interconnected by a power preserving interconnection, they exhibit the property of being another pH system [34]. This property is due to the specific geometric structure of pH systems, discussed in section 4.1.1. Therefore, it is possible to interconnect the two layers that were proved to admit to a pH representation in section 4.2 and section 4.3. The two layers are interconnected using the control by interconnection (CbI) technique. The power preserving skew-symmetric interconnection matrix is the subsystem $\sum_I$ given below in (4.4.1). It should be noted that this part of the analysis neglects the regulator state.

$$\sum_I : \left\{ \begin{bmatrix} \boldsymbol{u}_p \\ \boldsymbol{u}_c \end{bmatrix} = \begin{bmatrix} \mathbf{0} & -\mathbf{1} \\ \mathbf{1} & \mathbf{0} \end{bmatrix} \begin{bmatrix} \boldsymbol{y}_p \\ \boldsymbol{y}_c \end{bmatrix} \right. \tag{4.4.1}$$

The following result in the relation $\boldsymbol{u}_p = -\boldsymbol{y}_c$ and $\boldsymbol{u}_c = \boldsymbol{y}_p$. The output ports of each system were previously obtained in (4.2.5) and (4.3.4) from the definition of the passive output. This implies that $\boldsymbol{u}_c = \boldsymbol{y}_p = \boldsymbol{\mathcal{I}}^{\mathcal{G}}\boldsymbol{I}^{\mathcal{G}}_{\text{pu}}$ and $\boldsymbol{u}_p = -\boldsymbol{y}_c = -\boldsymbol{K}_y\boldsymbol{K}_I\boldsymbol{\lambda}$, i.e., the voltage input in the physical layer takes the shape of gains and the set point. The Hamiltonian function of a combined system is obtained by the sum of the Hamiltonian functions of its port-Hamiltonian subsystems and as given below in (4.4.2) [34].

$$H_T(\boldsymbol{x}_T) = H_p(\boldsymbol{x}_p) + H_c(\boldsymbol{x}_c) = \frac{1}{2}\boldsymbol{x}_p^\top\boldsymbol{Q}_p\boldsymbol{x}_p + \frac{1}{2}\boldsymbol{x}_c^\top\boldsymbol{Q}_c\boldsymbol{x}_c \tag{4.4.2}$$

The above expression results in the pH representation of the interconnected system as given in (4.4.3b) and in matrix notation in (4.4.4). $\boldsymbol{Q}_T$ is a block diagonal matrix consisting of the elements of $\boldsymbol{Q}_p$ and $\boldsymbol{Q}_c$ in the diagonal, i.e., $\boldsymbol{Q}_T = \text{blockdiag}\{(\boldsymbol{L}_*^{\mathcal{G}})^{-1}, (\boldsymbol{L}^{\mathcal{E}})^{-1}, (\boldsymbol{C}^{\mathcal{N}})^{-1}, \boldsymbol{K}_y, \boldsymbol{K}_I\}$.

$$\sum_T \begin{cases} \dot{\boldsymbol{x}}_T = \boldsymbol{F}_T \boldsymbol{\nabla} H_T(\boldsymbol{x}_T) + \boldsymbol{E}_T \\ \boldsymbol{y}_T = \boldsymbol{g}_T^\top \boldsymbol{\nabla} H_T(\boldsymbol{x}_T) \end{cases} \tag{4.4.3a}$$

$$H_T(\boldsymbol{x}_T) = \frac{1}{2} {\boldsymbol{x}_T}^\top \boldsymbol{Q}_T \boldsymbol{x}_T \tag{4.4.3b}$$

$$\underbrace{\begin{bmatrix} \boldsymbol{L}_*^{\mathcal{G}} \dot{\boldsymbol{I}}_{\text{pu}}^{\mathcal{G}} \\ \boldsymbol{L}_*^{\mathcal{E}} \dot{\boldsymbol{I}}^{\mathcal{E}} \\ \boldsymbol{C}_*^{\mathcal{N}} \dot{\boldsymbol{V}}^{\mathcal{N}} \\ \dot{\boldsymbol{\zeta}} \\ \dot{\boldsymbol{\lambda}} \end{bmatrix}}_{\dot{\boldsymbol{x}}_T} = \underbrace{\begin{bmatrix} -\boldsymbol{R}_*^{\mathcal{G}} & \boldsymbol{0} & -\boldsymbol{\mathcal{B}}^{\mathcal{G}^\top} & \boldsymbol{0} & -\boldsymbol{K}_y \\ \boldsymbol{0} & -\boldsymbol{R}_*^{\mathcal{E}} & -\boldsymbol{\mathcal{B}}_*^{\mathcal{E}^\top} & \boldsymbol{0} & \boldsymbol{0} \\ \boldsymbol{\mathcal{B}}^{\mathcal{G}} & \boldsymbol{\mathcal{B}}_*^{\mathcal{E}} & -\boldsymbol{G}_{*,cte}^{\mathcal{N}} & \boldsymbol{0} & \boldsymbol{0} \\ \boldsymbol{0} & \boldsymbol{0} & \boldsymbol{0} & \boldsymbol{0} & -\boldsymbol{\mathcal{L}} \\ \boldsymbol{K}_y & \boldsymbol{0} & \boldsymbol{0} & \boldsymbol{\mathcal{L}} & -\left(\boldsymbol{K}_y + \boldsymbol{\mathcal{L}} \boldsymbol{K}_P\right) \boldsymbol{K}_I^{-1} \end{bmatrix}}_{\boldsymbol{F}_T} \underbrace{\begin{bmatrix} \boldsymbol{I}_{\text{pu}}^{\mathcal{G}} \\ \boldsymbol{I}^{\mathcal{E}} \\ \boldsymbol{V}^{\mathcal{N}} \\ \boldsymbol{K}_y \boldsymbol{\zeta} \\ \boldsymbol{K}_I \boldsymbol{\lambda} \end{bmatrix}}_{\boldsymbol{\nabla} H_T(\boldsymbol{x}_T)} + \underbrace{\begin{bmatrix} \boldsymbol{1} V_{\text{nom}} \\ \boldsymbol{0} \\ -\boldsymbol{I}_{*,\text{cte}} \\ \boldsymbol{0} \\ \boldsymbol{0} \end{bmatrix}}_{\boldsymbol{E}_T} \tag{4.4.4}$$

From (4.4.2), it can be noted that the time derivative of the stored energy in a combined system is equal to the sum of the time derivatives of the stored energy in each of its subsystems, as presented in (4.4.5a) below. In the previous sections, it has been demonstrated that both the physical and cyber layers can be represented as pH systems. As a result, the time derivative of the corresponding Hamiltonian functions, $\dot{H}_p$ and $\dot{H}_c$ presented in (4.4.5b), take on the pH form discussed in section 4.1.1. Consequently, the skew-symmetric parts of the system cancel out, resulting in a simplified form. In (4.4.5c), the input ports are substituted by the output ports, and energy stored in the cyber layer cancels out energy stored in the physical layer. This proves that the interconnection is power preserving and $\dot{H}_T(\boldsymbol{x}_T) \leq \boldsymbol{\nabla}^\top H_p(\boldsymbol{x}_p) \boldsymbol{E}_p$ as shown in (4.4.5d). Additionally, it is proved that a power preserving interconnection of two pH systems results in another pH system.

$$\dot{H}_T(\boldsymbol{x}_T) = \dot{H}_p(\boldsymbol{x}_p) + \dot{H}_c(\boldsymbol{x}_c) \tag{4.4.5a}$$

$$= \underbrace{-\boldsymbol{\nabla}^\top H_p(\boldsymbol{x}_p) \boldsymbol{R}_p \boldsymbol{\nabla} H_p(\boldsymbol{x}_p) + \boldsymbol{y}_p^\top \boldsymbol{u}_p + \boldsymbol{\nabla}^\top H_p(\boldsymbol{x}_p) \boldsymbol{E}_p}_{\dot{\boldsymbol{H}}_p} \quad \underbrace{-\boldsymbol{\nabla}^\top H_c(\boldsymbol{x}_c) \boldsymbol{R}_c \boldsymbol{\nabla} H_c(\boldsymbol{x}_c) + \boldsymbol{y}_c^\top \boldsymbol{u}_c}_{\dot{\boldsymbol{H}}_c} \tag{4.4.5b}$$

$$= -\boldsymbol{\nabla}^\top H_p(\boldsymbol{x}_p) \boldsymbol{R}_p \boldsymbol{\nabla} H_p(\boldsymbol{x}_p) - \boldsymbol{\nabla}^\top H_c(\boldsymbol{x}_c) \boldsymbol{R}_c \boldsymbol{\nabla} H_c(\boldsymbol{x}_c) \quad \underbrace{-\boldsymbol{y}_p^\top \boldsymbol{y}_c + \boldsymbol{y}_c^\top \boldsymbol{y}_p}_{0} + \boldsymbol{\nabla}^\top H_p(\boldsymbol{x}_p) \boldsymbol{E}_p \tag{4.4.5c}$$

$$= -\boldsymbol{\nabla}^\top H_T(\boldsymbol{x}_T) \boldsymbol{R}_T \boldsymbol{\nabla} H_T(\boldsymbol{x}_T) + \boldsymbol{\nabla}^\top H_p(\boldsymbol{x}_p) \boldsymbol{E}_p \tag{4.4.5d}$$

As earlier, the Hamiltonian function of the incremental model is used as a Lyapunov candidate to analyze the stability of the system. The incremental model of the combined system that is used in the energy analysis is given below in (4.4.6).

$$\tilde{\sum_T} \begin{cases} \dot{\tilde{\boldsymbol{x}}}_T = \boldsymbol{F}_T \boldsymbol{\nabla} V_T(\tilde{\boldsymbol{x}}_T) + \boldsymbol{g}_T \tilde{\boldsymbol{u}}_T \\ \tilde{\boldsymbol{y}}_T = \boldsymbol{g}_T^\top \boldsymbol{\nabla} V_T(\tilde{\boldsymbol{x}}_T) \end{cases} \tag{4.4.6a}$$

$$V_T(\tilde{\boldsymbol{x}}_T) = \frac{1}{2} \tilde{\boldsymbol{x}}_T^\top \boldsymbol{Q}_T \tilde{\boldsymbol{x}}_T \tag{4.4.6b}$$

$$\dot{V}_T(\tilde{\boldsymbol{x}}_T) = -\boldsymbol{\nabla}^\top V_T(\tilde{\boldsymbol{x}}_T) \boldsymbol{R}_T \boldsymbol{\nabla} V_T(\tilde{\boldsymbol{x}}_T) \leq 0 \tag{4.4.6c}$$

The following relationship $V_T(\tilde{\boldsymbol{x}}_T) > 0$ is valid since $\boldsymbol{Q}_T$ is proven to be a positive definite matrix consisting of only the inverse of stored inductance and capacitance and some positive gains. As $\boldsymbol{R}_T \geq \boldsymbol{0}$ has semi-definite properties, Equation (4.4.6c) implies that $\dot{V}_T(\tilde{\boldsymbol{x}}_T) \leq 0$ meaning the rate of change of the energy stored in the system is non-increasing and that the system is stable. By applying LaSalle's invariance principle on the system equations, it can be stated that $\dot{V}_T(\tilde{\boldsymbol{x}}_T) < 0$ and the system is globally asymptotically stable [36]. In conclusion, the interconnection solely between the physical layer and the cyber layer admits to a pH representation without any challenges.

Steady State Conditions

As previously discussed, the primary function of the regulator is to ensure that the current ratios $\bar{I}^{\mathcal{G}}_{i,\text{pu}}$ converge to the set point, which is the average of all the generator currents as derived in (3.3.3). When the regulator is neglected, the controller loses its ability to control the currents, failing to achieve the goal of proportional current sharing. Additionally, the initial analysis neglects the voltage saturation, which causes the controller to lose both of its objectives. However, (2.1.3e) gets equal to $\bar{\boldsymbol{V}}^{\mathcal{G}} = \boldsymbol{1}V_{\text{nom}} + \bar{\boldsymbol{u}}_p = \boldsymbol{1}V_{\text{nom}} - \boldsymbol{K}_y\boldsymbol{K}_I\bar{\boldsymbol{\lambda}}$ when the steady state conditions are achieved. Since the last term in the equation is negative, the voltages will remain within their limit and not exceed the voltage bound as long as $\boldsymbol{K}_y\boldsymbol{K}_I\bar{\boldsymbol{\lambda}} < \boldsymbol{\Delta}$.

Furthermore, note that when consensus is reached on the set points under nominal conditions, the parameters in the equation are identical for all generators, resulting in identical voltages at each generator. This observation implies that proportional voltage-sharing is achieved in steady state, which is the opposite of the intended objective of proportional current-sharing. Therefore, it is possible in further research to explore the consequences of flipping the current and voltage in the system such that proportional current-sharing gets achieved instead.

Simulation of the Interconnected System

The mathematical findings discussed above can be validated by implementing the closed-loop system in Simulink. The Simulink model has the parameters for the generators, transmission lines, and loads as previously listed in Table 3.1, 3.2, and 3.3, respectively. The gains of the controller are chosen as $k_I = 0.7$, $k_y = 0.4$ and $k_p = 2$. Furthermore, the control variable, $\boldsymbol{u}_p$, is activated at $t = 10$ seconds, and the 50% step in load is applied at $t = 80$ seconds to study the behavior of the DC MG after the DC MG has reached steady state conditions. The load change is removed after an additional 40 seconds. The long simulation period is a result of the relatively simple controller that excludes the regulator and time constants.

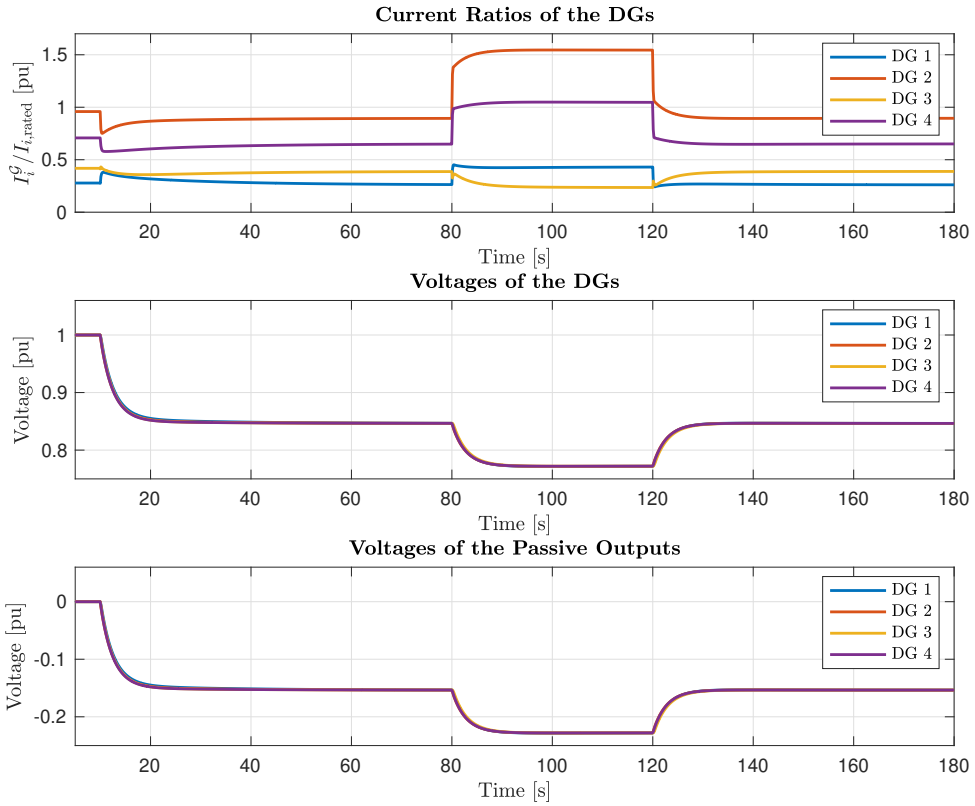

Figure 4.2: Simulation of the interconnected CP MG disregarding the regulator state.

As depicted in Figure 4.2, the voltages converge to an identical value, assuring proportional voltage-sharing throughout the simulation period instead of proportional current-sharing. However, there are no signs of instabilities in the system, which makes sense because of the previous proof stating the asymptotic stability of the system. It should be noted that this is the opposite of the desired control objectives. This leaves room for exploring a flipped version of the system, where the currents and voltages are interchanged; i.e., modeling converters as controlled current sources instead of voltage sources.

4.4.2 Analyzing the Physical Layer With the Regulator State Included

In this section, the regulator state is included in the dynamics of the physical layer, while the cyber layer is neglected. Since the regulator state is not considered another layer, introducing an interconnection matrix is irrelevant.

In the cyber-physical DC MG, the cyber layer provides information about the set point to the physical layer. However, in the absence of the cyber layer, the set point is treated as a constant reference, denoted by $\mathbf{1}\lambda_{\text{ref}}$ in (3.2.1b). Note that the leakage function, $\rho(\boldsymbol{v})$, is neglected in this equation. Furthermore, to ensure a valid pH representation, another modification is required. The challenge occurs because V_{nom} is multiplied by the generator current in (3.2.1b), but not with the regulator state in (4.2.2a). As a result, the system loses its skew-symmetry. To solve this, V_{nom} can be considered a constant gain set to one, ensuring a valid pH representation. However, eliminating V_{nom} does not impact the system since this parameter is already defined as 1pu in the regulator

equation. The modifications result in the differential equation for the regulator state as depicted below in (4.4.7).

$$\boldsymbol{\tau}\dot{\boldsymbol{v}} = \mathbf{1}\lambda_{\text{ref}} - \boldsymbol{I}_{\text{pu}}^{\mathcal{G}} \tag{4.4.7}$$

With these adjustments, the regulator equation can be incorporated into the pH representation of the physical system as seen below in (4.4.8). The identity matrix, $\boldsymbol{\mathcal{I}}^{\mathcal{G}}$, is added to ensure that the dimensions in the equations add up as earlier explained in section 4.2.

$$\underbrace{\begin{bmatrix} \boldsymbol{L}_*^{\mathcal{G}}\dot{\boldsymbol{I}}_{\text{pu}}^{\mathcal{G}} \\ \boldsymbol{L}_*^{\mathcal{E}}\dot{\boldsymbol{I}}^{\mathcal{E}} \\ \boldsymbol{C}_*^{\mathcal{N}}\dot{\boldsymbol{V}}^{\mathcal{N}} \\ \boldsymbol{\tau}\dot{\boldsymbol{v}} \end{bmatrix}}_{\dot{\boldsymbol{x}}_{pr}} = \underbrace{\begin{bmatrix} -\boldsymbol{R}_*^{\mathcal{G}} & \mathbf{0} & -\boldsymbol{\mathcal{B}}^{\mathcal{G}^\top} & \boldsymbol{\mathcal{I}}^{\mathcal{G}} \\ \mathbf{0} & -\boldsymbol{R}_*^{\mathcal{E}} & -\boldsymbol{\mathcal{B}}_*^{\mathcal{E}^\top} & \mathbf{0} \\ \boldsymbol{\mathcal{B}}^{\mathcal{G}} & \boldsymbol{\mathcal{B}}_*^{\mathcal{E}} & -\boldsymbol{G}_{*,cte}^{\mathcal{N}} & \mathbf{0} \\ -\boldsymbol{\mathcal{I}}^{\mathcal{G}} & \mathbf{0} & \mathbf{0} & \mathbf{0} \end{bmatrix}}_{\boldsymbol{F}_{pr}} \underbrace{\begin{bmatrix} \boldsymbol{I}_{\text{pu}}^{\mathcal{G}} \\ \boldsymbol{I}^{\mathcal{E}} \\ \boldsymbol{V}^{\mathcal{N}} \\ \boldsymbol{v} \end{bmatrix}}_{\boldsymbol{\nabla} H_{pr}(\boldsymbol{x}_{pr})} + \underbrace{\begin{bmatrix} \boldsymbol{\mathcal{I}}^{\mathcal{G}} \\ \mathbf{0} \\ \mathbf{0} \\ \mathbf{0} \end{bmatrix}}_{\boldsymbol{g}_p} \boldsymbol{u}_{pr} + \underbrace{\begin{bmatrix} \mathbf{1}V_{\text{nom}} \\ \mathbf{0} \\ -\boldsymbol{I}_{*,\text{cte}} \\ \mathbf{1}\lambda_{\text{ref}} \end{bmatrix}}_{\boldsymbol{E}_{pr}} \tag{4.4.8}$$

Studying the system and the characteristic matrices it can be stated that the system admits to the pH formalism: The interconnection matrix $\boldsymbol{J}_{pr} \in \mathbb{R}^{17\times17}$ is skew-symmetric, the dissipation matrix $\boldsymbol{R}_{pr} \in \mathbb{R}^{17\times17}$ is positive semi-definite and $\boldsymbol{Q}_{pr} \in \mathbb{R}^{17\times17}$ is symmetric positive definite.

$$\boldsymbol{J}_{pr} := \begin{bmatrix} \mathbf{0} & \mathbf{0} & -\boldsymbol{\mathcal{B}}^{\mathcal{G}^\top} & \boldsymbol{\mathcal{I}}^{\mathcal{G}} \\ \mathbf{0} & \mathbf{0} & -\boldsymbol{\mathcal{B}}_*^{\mathcal{E}^\top} & \mathbf{0} \\ \boldsymbol{\mathcal{B}}^{\mathcal{G}} & \boldsymbol{\mathcal{B}}_*^{\mathcal{E}} & \mathbf{0} & \mathbf{0} \\ -\boldsymbol{\mathcal{I}}^{\mathcal{G}} & \mathbf{0} & \mathbf{0} & \mathbf{0} \end{bmatrix} \quad \boldsymbol{R}_{pr} := \begin{bmatrix} \boldsymbol{R}_*^{\mathcal{G}} & \mathbf{0} & \mathbf{0} & \mathbf{0} \\ \mathbf{0} & \boldsymbol{R}_*^{\mathcal{E}} & \mathbf{0} & \mathbf{0} \\ \mathbf{0} & \mathbf{0} & \boldsymbol{G}_{*,cte}^{\mathcal{N}} & \mathbf{0} \\ \mathbf{0} & \mathbf{0} & \mathbf{0} & \mathbf{0} \end{bmatrix}$$

$$\boldsymbol{Q}_{pr} := \begin{bmatrix} (\boldsymbol{L}_*^{\mathcal{G}})^{-1} & \mathbf{0} & \mathbf{0} & \mathbf{0} \\ \mathbf{0} & (\boldsymbol{L}_*^{\mathcal{E}})^{-1} & \mathbf{0} & \mathbf{0} \\ \mathbf{0} & \mathbf{0} & (\boldsymbol{C}_*^{\mathcal{N}})^{-1} & \mathbf{0} \\ \mathbf{0} & \mathbf{0} & \mathbf{0} & (\boldsymbol{\tau})^{-1} \end{bmatrix}$$

Since the combination of the electrical network and the regulator admits to a pH representation, the incremental model of the system can be introduced to facilitate the stability analysis. Giving the following incremental pH system in (4.4.9b), where the constant terms is disregarded. By performing the identical procedure as in (4.2.5), it is discovered that the passive output of the incremental model, $\tilde{\boldsymbol{y}}_{pr}$, is equal to the passive output of the physical layer, $\tilde{\boldsymbol{y}}_p$. This is because the control variable, $\tilde{\boldsymbol{u}}_{pr}$, only appears in the expression for the generator voltages.

$$\tilde{\sum_{pr}} \begin{cases} \dot{\tilde{\boldsymbol{x}}}_{pr} = \boldsymbol{F}_{pr}\boldsymbol{\nabla}V_{pr}(\tilde{\boldsymbol{x}}_{pr}) + \boldsymbol{g}_{pr}\tilde{\boldsymbol{u}}_p \\ \tilde{\boldsymbol{y}}_{pr} = \boldsymbol{g}_{pr}^\top\boldsymbol{\nabla}V_{pr}(\tilde{\boldsymbol{x}}_{pr}) \end{cases} \tag{4.4.9a}$$

$$V_{pr}(\tilde{\boldsymbol{x}}_{pr}) = \frac{1}{2}\tilde{\boldsymbol{x}}_{pr}^\top\boldsymbol{Q}_{pr}\tilde{\boldsymbol{x}}_{pr} \tag{4.4.9b}$$

$$\dot{V}_{pr}(\tilde{\boldsymbol{x}}_{pr}) = -\boldsymbol{\nabla}^\top V_{pr}(\tilde{\boldsymbol{x}}_{pr})\boldsymbol{R}_{pr}\boldsymbol{\nabla}V_{pr}(\tilde{\boldsymbol{x}}_{pr}) + \tilde{\boldsymbol{y}}_{pr}^\top\tilde{\boldsymbol{u}}_{pr} \tag{4.4.9c}$$

$$\tag{4.4.9d}$$

The relationship $V_{pr}(\tilde{\boldsymbol{x}}_{pr}) > 0$ is valid because $\boldsymbol{Q}_{pr}$ is a positive definite matrix as in (4.4.9b) and $\dot{V}_{pr}(\tilde{\boldsymbol{x}}_{pr}) \leq \tilde{\boldsymbol{y}}_{pr}^\top\tilde{\boldsymbol{u}}_{pr}$ is valid because $\boldsymbol{R}_{pr} \geq 0$ in (4.4.9c) has semi-definite properties. Consequently, the open-loop system presented in this section admits to a pH representation and is passive with respect to the passive input and output. In conclusion, this specific part of the CP DC MG exhibits

a structure that does not introduce any problems within the pH representation for the combined system.

Steady State Conditions

In steady state, the regulator state equation yields the following: $\boldsymbol{\tau}\dot{\tilde{\boldsymbol{v}}} = \mathbf{1}\lambda_{\text{ref}} - \bar{\boldsymbol{I}}^{\mathcal{G}}_{\text{pu}} = \mathbf{0} \Rightarrow \mathbf{1}\lambda_{\text{ref}} = \bar{\boldsymbol{I}}^{\mathcal{G}}_{\text{pu}}$. This implies that the currents will drive towards the common set point and that all generator currents will be identical. Therefore, including the regulator state in the physical layer facilitates proportional current-sharing. However, in the absence of the cyber layer, there is no distributed communication between the generators, and the set point is not determined based on the average of the generator currents. In contrast, the network communication is centralized, meaning that each generator has information about a single common set point, and the regulator state drives each generator's current to be equal to this set point. A consequence of centralized communication is, as mentioned in section 1.1.3, that the system is more vulnerable to cyber-attacks and that it also loses the scalability in the system.

4.4.3 Analyzing the Cyber Layer With the Regulator State Included

In this part of the analysis, the interface of the cyber layer and regulator state is examined. It should be noted that this combination does not include the electrical network and would not be applicable in a practical setting. However, keep in mind that the purpose of these sections is primarily to investigate if there are any challenges related to the pH representation of the total DC MG.

The current ratios that appear in the regulator equation are represented by a constant vector $\boldsymbol{I}^{\mathcal{G}}_{\text{pu,ref}}$, similar to how the set point was replaced by a constant in the previous section 4.4.2. Furthermore, the regulator state is attempted to be included in the open-loop pH representation of the cyber layer below in (4.4.10).

$$\underbrace{\begin{bmatrix}\dot{\boldsymbol{\zeta}}\\ \dot{\boldsymbol{\lambda}}\\ \boldsymbol{\tau}\dot{\boldsymbol{v}}\end{bmatrix}}_{\dot{\boldsymbol{x}}_{cr}} = \underbrace{\begin{bmatrix}\mathbf{0} & -\boldsymbol{\mathcal{L}} & \mathbf{0}\\ \boldsymbol{\mathcal{L}} & -\left(\boldsymbol{K}_y + \boldsymbol{\mathcal{L}}\boldsymbol{K}_P\right)\boldsymbol{K}_I^{-1} & \mathbf{0}\\ \mathbf{0} & \mathbf{1}V_{\text{nom}}\boldsymbol{K}_I^{-1} & \mathbf{0}\end{bmatrix}}_{\boldsymbol{F}_{cr}} \underbrace{\begin{bmatrix}\boldsymbol{K}_y\boldsymbol{\zeta}\\ \boldsymbol{K}_I\boldsymbol{\lambda}\\ \boldsymbol{v}\end{bmatrix}}_{\nabla H_{cr}(\boldsymbol{x}_{cr})} + \underbrace{\begin{bmatrix}\mathbf{0}\\ \boldsymbol{K}_y\\ \mathbf{0}\end{bmatrix}}_{\boldsymbol{g}_{cr}} \boldsymbol{u}_{cr} + \underbrace{\begin{bmatrix}\mathbf{0}\\ \mathbf{0}\\ -\mathbf{1}V_{\text{nom}}\boldsymbol{\mathcal{I}}^{\mathcal{G}}\boldsymbol{I}^{\mathcal{G}}_{\text{pu,ref}}\end{bmatrix}}_{\boldsymbol{E}_{cr}} \tag{4.4.10}$$

Based on the representation above, the pH matrices can be derived as shown below. It can be observed that $\boldsymbol{R}_{cr}$ and $\boldsymbol{Q}_{cr}$ have a valid pH structure and are both positive definite matrices. However, $\boldsymbol{J}_{cr}$ is not skew-symmetric, and the system does not admit to a pH representation. As a result, it can be concluded that the challenges concerning the pH structure occur at the interface between the cyber layer and the regulator state. Hence, this section has no purpose in further conducting a stability analysis.

$$\boldsymbol{J}_{cr} := \begin{bmatrix}\mathbf{0} & -\boldsymbol{\mathcal{L}} & \mathbf{0}\\ \boldsymbol{\mathcal{L}} & \mathbf{0} & \mathbf{0}\\ \mathbf{0} & \mathbf{1}V_{\text{nom}}\boldsymbol{K}_I^{-1} & \mathbf{0}\end{bmatrix} \qquad \boldsymbol{R}_{cr} := \begin{bmatrix}\mathbf{0} & \mathbf{0} & \mathbf{0}\\ \mathbf{0} & \left(\boldsymbol{K}_y + \boldsymbol{\mathcal{L}}\boldsymbol{K}_P\right)\boldsymbol{K}_I^{-1} & \mathbf{0}\\ \mathbf{0} & \mathbf{0} & \mathbf{0}\end{bmatrix} \qquad \boldsymbol{Q}_{cr} := \begin{bmatrix}\boldsymbol{K}_y & \mathbf{0} & \mathbf{0}\\ \mathbf{0} & \boldsymbol{K}_I & \mathbf{0}\\ \mathbf{0} & \mathbf{0} & \boldsymbol{\tau}^{-1}\end{bmatrix}$$

The lack of a valid stability proof at the interface between the cyber layer and the regulator presents a challenge in obtaining a valid stability proof for the entire DC MG, which includes both and

the regulator state. The complexity of the controller, particularly the outer loop derived from the regulator, contributes to the challenges in obtaining a valid pH representation. The outer loop problem pertains to the regulation of the state, $\boldsymbol{I}_{\text{pu}}^{\mathcal{G}}$ to be equal another state, $\boldsymbol{\lambda}$. This problem will be further investigated in section 5.

Chapter 5

Proposing a Modified Controller With a Stability Certificate

From previous derivations in this master's thesis, it is evident that the proposed controller in Babak Abdolmaleki's and Gilbert Bergna-Diaz's paper [2] achieves the desired control objectives. Nevertheless, when the incremental model of the case-specific DC MG is interconnected with the controller, it fails to meet the requirements for obtaining a stability certificate. Specifically, a Lyapunov function of the incremental model is not identified. Ideally, the proposed controller should immediately result in a Lyapunov function. However, since this approach has yet to be successful, alternative methodologies need to be explored to obtain a stability certificate. This chapter investigates the mathematical framework known as *singular perturbations theory* as a potential solution to obtain a stability certificate by taking inspiration from another publication [39] by Abdolmaleki et al. The article utilizes singular perturbation theory to obtain a valid stability certificate for an AC MG.

This chapter only contains new contributions and is not related to the associated specialization project.

5.1 Singular Perturbations Theory for Time Scale Separation

Singular perturbation theory is a method to control a system of different scales, where the system equations are divided into equations representing the fast and slow dynamics [40]. The standard singular perturbation model is depicted below, where (5.1.1a) is the reduced model representing the slow dynamics, while (5.1.1b) is the boundary-layer model representing the fast dynamics. ϵ is the singular perturbation parameter, a small positive parameter [41].

$$\dot{x} = f(t, x, z, \epsilon) \tag{5.1.1a}$$

$$\epsilon \dot{z} = g(t, x, z, \epsilon) \tag{5.1.1b}$$

The separation of the system results in two stability analyses. Accordingly, it can be attempted to find two Lyapunov functions – one for the fast model and another for the slow model. Following the standard procedure of singular perturbation theory, a Lyapunov function of the composite system

within a given interval of ϵ can be approximated by the solutions of the slow and fast subsystems [41]. The parameter, ϵ, describes the relationship between the time constants corresponding to the fast and slow models, implying that it decides the relationship that ensures stability in the system.

Obtaining a Lyapunov function and a stability proof of the composite system employing singular perturbation theory is a comprehensive procedure and will not be formally conducted in this master's thesis. However, the proof will be derived under specific simplifications and assumptions. A more advanced proof will be left for further research.

5.2 Conducting an Analysis of the Modified Controller

As proven in the previous chapter 4, the interface between the cyber layer and regulator state causes problems obtaining a pH representation of the total CP DC MG. The concepts of singular perturbation theory from above can be utilized to derive a controller that provides a stability certificate for the interconnected cyber-physical DC MG. Note that the hyperbolic tangent and leakage functions remain excluded from the energy analysis for as long as the stability proof of the linear system is obtained.

In section 4.4.1, it was proved that the interconnection of the cyber and physical layers admits to the pH formalism. This important feature is carried forward in the pursuit of a controller in this chapter. Therefore, the system $\sum_T$ from section 4.4.1 is used as a starting point in the new proposal. Consequently, the output ports of both layers obtained in (4.2.5) and (4.3.4) are continued, and the interconnection matrix from (4.4.1) is further utilized in this system. This method facilitates the design of a controller considering the passive outputs, which is an important aspect of obtaining a stability certificate. Note that the equation for the physical layer (4.2.2) and the cyber layer (4.3.1) remain.

Nevertheless, the configuration in $\sum_T$ neglects the regulator state such that the proportional current-sharing provided by the regulator state is not satisfied. To ensure that this control objective is satisfied, the input of the physical layer is divided into $\boldsymbol{u}_{p,1}$ and $\boldsymbol{u}_{p,2}$ as presented below. The assurance of achieving the objective of proportional current-sharing occurs in the integrator term of the equation corresponding to the second input (5.2.1c), where the additional state, $\boldsymbol{x}$ is included. The integrator term in (5.2.1d) drives the currents to be equal to the set points, minimizing the error, $\boldsymbol{e}$, with the very purpose of the previously mentioned regulator state $\boldsymbol{v}$.

$$\boldsymbol{u}_p = \boldsymbol{u}_{p,1} + \boldsymbol{u}_{p,2} \tag{5.2.1a}$$

$$\boldsymbol{u}_{p,1} = -\boldsymbol{K}_I \boldsymbol{K}_y \boldsymbol{\lambda} \tag{5.2.1b}$$

$$\boldsymbol{u}_{p,2} = \boldsymbol{K}_{p,2}(\boldsymbol{\lambda} - \boldsymbol{I}_{pu}^{\mathcal{G}}) + \boldsymbol{x} \tag{5.2.1c}$$

$$\tau \dot{\boldsymbol{x}} = \boldsymbol{e} = \boldsymbol{\lambda} - \boldsymbol{I}_{pu}^{\mathcal{G}} \tag{5.2.1d}$$

However, what distinguishes this modified version of the controller from the original controller is that the time constant in the integrator, (5.2.1d), is assigned a significant value compared to the rest of the dynamics. This results in a separation between the fast and slow dynamics in the system. Specifically, the integrator is considered the slow dynamics, while the rest of the system is considered the fast dynamics. The separation of the system facilitates the use of singular perturbation theory to obtain a stability certificate. In this chapter, an analysis of the fast system with respect to the slow variables is conducted.

The increased time constant results in the relationship $\dot{\boldsymbol{x}} = \boldsymbol{e}/\tau \approx \boldsymbol{0}$, which implies that there is ap-

proximately no change in $\boldsymbol{x}$ and it can be treated as a constant in (5.2.1c). Since the corresponding time constant is larger than the rest of the dynamics in the system, it is assumed that the faster elements responsible for consensus have converged on a set point by the time $\boldsymbol{x}$ reaches steady state. Accordingly, the set point associated with the fast dynamics is considered a quasi-steady state value in the equation of the integrator. This implies that the set point is changing so slowly that it can be considered a constant. In other words, the other dynamics in the system reach steady state significantly faster than the integrator. The increased time constant also implies that the system's response becomes slow. However, the system's stability and steady state conditions are more critical than its response time.

Studying the expressions of $\boldsymbol{u}_{p,2}$, the current ratios are multiplied by the gain $\boldsymbol{K}_{p,2}$, which implies that increasing $\boldsymbol{K}_{p,2}$ will result in $\boldsymbol{I}_{\text{pu}}^{\mathcal{G}}$ influencing the output even more. For this reason, it is assumed that $\boldsymbol{K}_{p,2}$ is approximately zero. With $\boldsymbol{K}_{p,2} \approx \boldsymbol{0}$ and $\boldsymbol{x}$ constant, it implies that $\boldsymbol{u}_{p,2}$ is considered constant compared to the other dynamics in the system. Recall that constants are removed in the incremental model as discussed in 4.1.3. Consequently, $\boldsymbol{u}_{p,2}$ is removed in the energy and stability analysis of the incremental model, resulting in $\tilde{\boldsymbol{u}}_{p,2} = \boldsymbol{0}$. Therefore, the additional $\boldsymbol{u}_{p,2}$ will not impact the stability proof.

The incremental storage functions of the physical and cyber layers are used as Lyapunov candidates to illustrate that $\boldsymbol{u}_{p,2}$ is not affecting the stability proof of the interconnected cyber-physical DC MG, $\sum_T$, from section 4.4.1. Firstly, $\boldsymbol{Q}_T$ is as previously presented and is a positive definite matrix such that $V_T(\tilde{\boldsymbol{x}}_T) > 0$. Secondly, the derivatives of the Lyapunov candidates are studied to evaluate if $\dot{V}_T(\tilde{\boldsymbol{x}}_T) \leq 0$ still holds. The result from (4.2.7a) is reproduced with an updated $\tilde{\boldsymbol{u}}_p$ below in (5.2.2a), while (5.2.2b) is identical to the result in (4.3.6).

$$\dot{V}_p(\tilde{\boldsymbol{x}}_p) \leq \tilde{\boldsymbol{y}}_p^\top \tilde{\boldsymbol{u}}_p = \tilde{\boldsymbol{y}}_p^\top \tilde{\boldsymbol{u}}_{p,1} + \tilde{\boldsymbol{y}}_p^\top \tilde{\boldsymbol{u}}_{p,2} \tag{5.2.2a}$$

$$\dot{V}_c(\tilde{\boldsymbol{x}}_c) \leq \tilde{\boldsymbol{y}}_c^\top \tilde{\boldsymbol{u}}_c \tag{5.2.2b}$$

As illustrated in (5.2.3a), the Lyapunov candidate for the interconnected system is a summation of the Lyapunov functions of the two layers. The two relationships from (5.2.2a) and (5.2.2b) that apply for these functions yields as follows in (5.2.3b). The interconnection matrix from (4.4.1) results in the passive outputs and inputs as presented in section 4.4.1. However, $\boldsymbol{u}_{p,2}$ is considered constant and gets eliminated in the incremental model as shown in (5.2.3c). Furthermore, the input ports are substituted by the passive output ports, and the skew-symmetric parts of the system cancel out. Consequently, the relationship in (5.2.3d) is valid, and the incremental model of the total DC MG is a Lyapunov candidate, which satisfies the asymptotically stable requirements when LaSalle's invariance principle is applied [36].

$$\dot{V}_T(\tilde{\boldsymbol{x}}_T) = \dot{V}_c(\tilde{\boldsymbol{x}}_c) + \dot{V}_p(\tilde{\boldsymbol{x}}_p) \tag{5.2.3a}$$

$$\leq \tilde{\boldsymbol{y}}_c^\top \tilde{\boldsymbol{u}}_c + \tilde{\boldsymbol{y}}_p^\top \tilde{\boldsymbol{u}}_{p,1} + \tilde{\boldsymbol{y}}_p^\top \tilde{\boldsymbol{u}}_{p,2} \tag{5.2.3b}$$

$$= \underbrace{\tilde{\boldsymbol{y}}_c^\top \tilde{\boldsymbol{y}}_p - \tilde{\boldsymbol{y}}_p^\top \tilde{\boldsymbol{y}}_c}_{=\boldsymbol{0}} + \underbrace{\tilde{\boldsymbol{y}}_p^\top \tilde{\boldsymbol{u}}_{p,2}}_{=\boldsymbol{0}} \tag{5.2.3c}$$

$$\dot{V}_T(\tilde{\boldsymbol{x}}_T) \leq 0 \tag{5.2.3d}$$

The derivations above demonstrate that the additional integrator does not affect the above stability proof using principles from singular perturbation theory. Consequently, a stability certificate for the fast system of the modified controller is obtained. Nevertheless, this analysis is the first step towards conducting the complex singular perturbation analysis for the interconnected system.

Furthermore, the complicated procedure of analyzing the slow dynamics and obtaining a Lyapunov candidate for the composite system within a specified interval of ϵ are needed to complete the proof. However, due to time limitation, we decided to leave this missing part of the analysis for future work and only then we could potentially conclude that the system will be robust to stability-related challenges under all circumstances. Additionally, the value of the time constant in (5.2.1d) that guarantees the stability of the composite system can be derived by ϵ in such further analysis.

That being said, from a practical perspective, it is possible to disconnect the integrator to maintain stable conditions in situations where ustable behavior begins to appear. To a certain extent, this practical option to disconnect the integrator when instability arises compensates for the lack of a formal proof of the slow system. As demonstrated in section 4.4.1, disconnecting the slow dynamics enables the system to meet the criteria for a stability certificate. However, as seen in Figure 4.2, the period of disconnection of the integrator comes at the expense of the control objectives concerning proportional current-sharing.

This analysis highlights the difficulties in achieving a perfect stability proof while meeting the control objectives. Furthermore, the master's thesis has emphasized that it is complicated to achieve both, especially in systems that include outer loops. Therefore, the control and electrical engineers must find a sufficient golden mean between the stability and control objective requirements. In contrast to the controller proposed in [1] and investigated in [3], it has been clear that the improvement of the control objectives in [2] comes at the cost of compromised stability. To summarize, obtaining a stability proof for this system is challenging, and certain simplifications have been made to obtain a stability certificate.

5.3 Simulations of the Modified Controller

The DC MG with the modified controller is implemented in Simulink, utilizing parameters specified in Table 3.1, 3.2 and 3.3. The gains are set to $k_I = 0.001$, $k_y = 1.2$, $k_p = 0.9$ and $k_{p,2} = 0.0001$. The events and the 50% load change specified in Table 3.4 is applied to the system, identical to the initial simulations conducted in section 3.4. The exact value of the time constant necessary to guarantee a stability proof has yet to be determined. Therefore, the system is simulated for three values of τ to demonstrate the difference in small and large time constants. Note that the saturation is disregarded in the controller for these simulations.

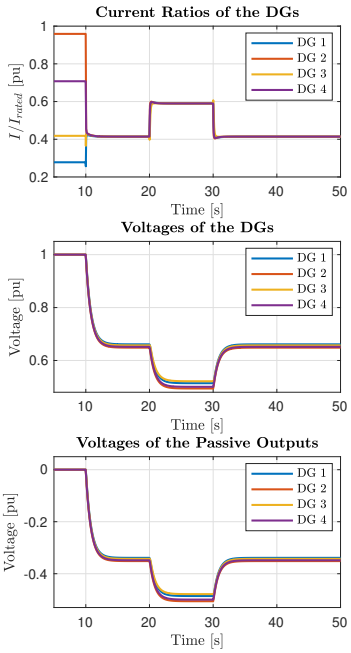

Figure 5.1: $\tau = 1$.

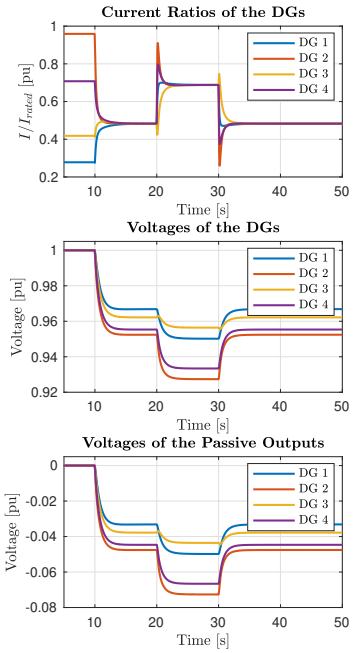

Figure 5.2: $\tau = 10$.

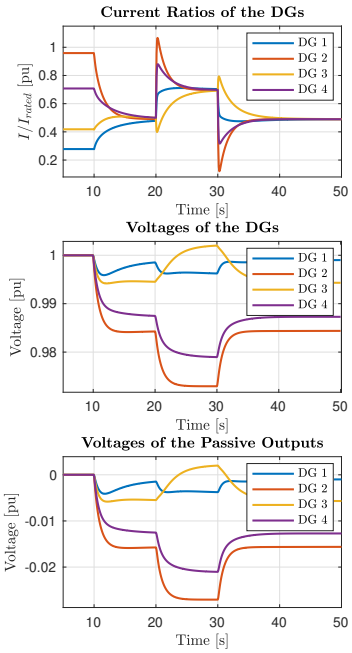

Figure 5.3: $\tau = 50$.

As observed in the figures 5.1 and 5.2, it is evident that the systems with time constants of $\tau = 1$ and $\tau = 10$ have relatively rapid responses, reaching steady state within ten seconds. However, this does not apply to the system with a time constant equal to $\tau = 50$, as depicted in Figure 5.3 which struggles to reach steady state before the step in load. In conclusion, a larger time constant results in a slower response, as predicted in section 5.2. This slow response may be the case for the case-specific system if the time constant eventually derived from ϵ is sufficiently large.

5.3.1 Including the Saturation Function and Leakage Coefficient

Simulations are conducted to examine the behavior of the modified controller when the saturation and leakage functions are included. Therefore, the leakage coefficient is added to (5.2.1d) as for the regulator state equation in (3.2.1b). Since we have not achieved a proper stability proof of the DC MG incorporated with this controller, the time constant is yet to be determined. Consequently, we choose to set it as $\tau = 10$ for illustration purposes. The gains are tuned to $k_I = 0.001$, $k_y = 10$, $k_p = 50$ and $k_{p,2} = 0.0001$. The 50% load change is implemented at $t = 30s$ and removed at $t = 70s$ in these simulations. The time interval differs from Table 3.4 because it will take longer for this system to reach steady state conditions due to the large time constant. First, the voltage band is set to the strict interval of $[V_{\min}, V_{\max}] = [0.99 \text{ pu}, 1.01 \text{ pu}]$ and the parameters are as presented in Table 3.1, 3.2 and 3.3. The simulation results for this DC MG are as depicted in Figure 5.4. Lastly, the leakage coefficient is included, and the voltage band is expanded to the interval of $[V_{\min}, V_{\max}] = [0.95 \text{ pu}, 1.05 \text{ pu}]$, while the load and transmission line parameters are modified as in section 3.4.5. The simulation results for these specifications are given in Figure 5.5.

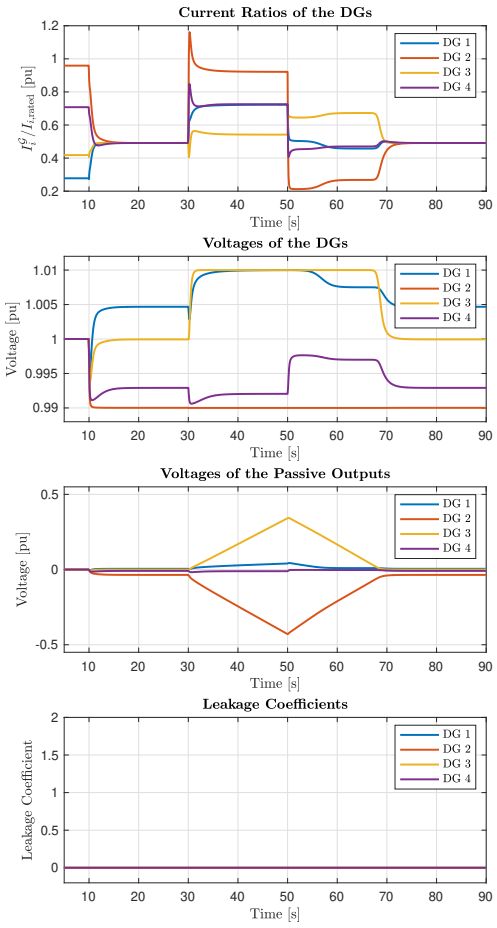

Figure 5.4: $[V_{\min}, V_{\max}] = [0.99 \text{ pu}, 1.01 \text{ pu}]$. The leakage coefficient is not included.

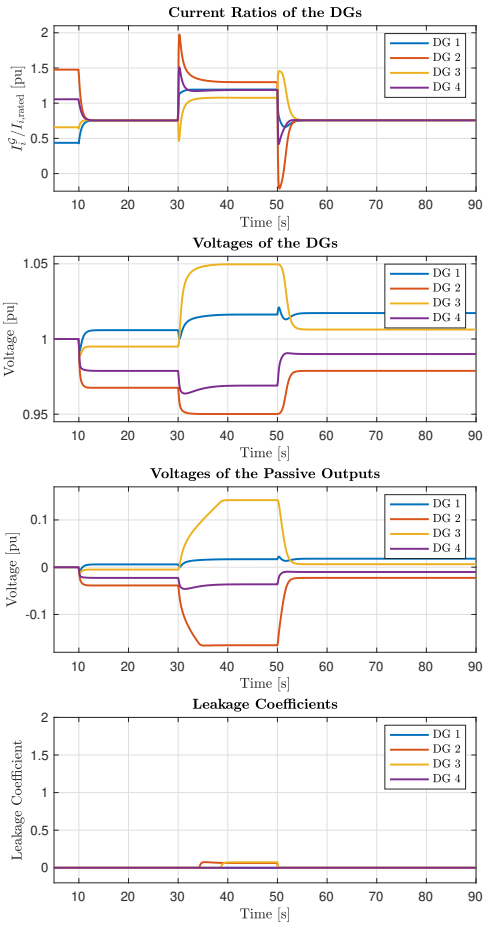

Figure 5.5: $[V_{\min}, V_{\max}] = [0.95 \text{ pu}, 1.05 \text{ pu}]$. Parameters from Table 3.1 and updated TL and load parameters. The leakage coefficient is included.

Upon comparing these two results with the corresponding simulation result of the original controller in Figure 3.1 and Figure 3.4 from section 3.4, it becomes apparent that there are notable similarities between them. The small values of k_I and $k_{p,2}$ tone down the effect of the new elements in the modified controller, contributing to the minor differences in the simulation results. However, incorporating the modified controller into the DC MG results in a longer response time and poorer transient response is poorer, as observed in the simulations presented in this section. As previously mentioned, stability properties are prioritized over performance and response time in this master's thesis. Considering these objectives, the modified controller's results are promising and give good prospects for future work.

Chapter 6

Conclusion and Further Work

In this thesis, we have provided an accessible introduction to large signal stability analysis through a systematic analysis of complex control concepts. The primary focus has been on the possibility and challenges of the application of PI consensus to DC MGs, focusing on achieving proportional current-sharing and voltage containment as key control objectives. Moreover, we have also aimed to achieve a scalable stability certificate for the system under investigation.

6.1 Conclusion

Initially, the electrical and control networks were presented, providing system equations and an introduction to graph theory. Moreover, this part of the thesis presented a case-specific example that was used for learning practices throughout mathematical derivations and simulations in the thesis.

Furthermore, the optimization problem that forms the basis for the controller was derived with Thesis Objective 1 in mind, aiming at an accessible presentation of complex topics. The optimization problem utilizes the consensus algorithm to achieve proportional current-sharing in a distributed manner. By solving the optimization problem via the KKT conditions, a common consensus-based set point for the DGs was obtained. The set points were equal to their respective current ratios and an additional term. Consequently, it was emphasized that the optimization problem provided a sub-optimal value for the set points due to the non-identical current ratios in the optimal solution. However, it was demonstrated that this term is only present in case of voltage saturation and represents the optimal solution under such operating conditions. Therefore, proportional current-sharing is achieved as long as the voltages are within operating limits and as accurately as possible during the saturation of voltages. Consequently, the thesis emphasizes the difficulty of obtaining both proportional current-sharing and desired voltage regulation as stated by [21] in the introduction in section 1.1.3.

The optimization problem forms the basis for the Proportional-Integral Dynamic Consensus Estimators presented in [2], which constitutes the cyber controller. Studying the steady state conditions of these estimators illustrates that the optimal set point is the average of all the DG's current ratios in the microgrid and ensures that a consensus is obtained at the set points. In conclusion, the estimators fulfill the optimization problem and achieve the objectives in steady state.

The thesis' investigation of the nonlinear local controller proposed in [2] provided a detailed overview of each control element, arguing why they are included in the control equations. It was

demonstrated that the nonlinear leakage coefficient had a solid connection to the additional term included in the shape of the set points. Additionally, it was illustrated through simulations that the leakage term efficiently functioned as an anti-wind up technique. The simulations also depicted that the controller successfully achieves its control objectives when connected to the case-specific DC MG.

Furthermore, the port-Hamiltonian representation for both the physical layer and cyber layer was obtained, which was promising regarding the large signal stability analysis. However, when the two layers were interconnected, challenges in the port-Hamiltonian structure preservation occurred at the interface between the cyber layer and the regulator state, as the *mathematical* interconnection between them is unfortunately not power preserving. As a result, Thesis Objective 2 of identifying these challenges was accomplished. To reduce the system's complexity until this issue is resolved in future work, the voltage saturation was neglected in the energy modeling in this thesis. Furthermore, a Lyapunov function for the incremental model of DC MG neglecting the regulator was obtained, such that a scalable stability certificate could be achieved. Although successful from a stability viewpoint, this system configuration could not achieve proportional current-sharing. Instead, it achieved proportional voltage-sharing, leaving an interesting topic of study for future work.

Eventually, we used the energy preserving interconnection between the physical and cyber layers in the attempt to design a suitable controller that could ensure a stability certificate for the total system and achieve Thesis Objective 3. Additionally, we took inspiration from singular perturbation theory to justify using time-scale separation arguments as a potential solution to obtain a scalable stability certificate. The dynamics of the controller from [2] were divided into slow and fast components, with the regulator state considered to have slow dynamics, which reduces the complexity of the equations as it is considered constant compared to the fast dynamics. When the energy analysis of the fast dynamics was conducted, a stability certificate was obtained because of energy preserving interconnection. However, the slow dynamics should also be analyzed to complete the stability proof using time-scale separation principles. Only then can we conclude that the system will be robust to stability-related challenges in all scenarios. However, it was argued that the slow dynamics could be disconnected from the system in practical situations to preserve stable conditions.

6.2 Further Work

As outlined in Limitation of Scope in section 1.2, simplifications were made in this thesis by using ZI loads and zero-order converters in the modeling of the physical network. Therefore, further research could explore the implementation of the nonlinear ZIP loads and advanced converters. Additionally, the master's thesis disregards transient analysis as performance was not the primary focus of this thesis.

Moreover, simplifications in regard to the energy and stability analysis were made due to the complicated structure of the combined system. This is due to the interface of the cyber layer and the regulator state that has been challenging in terms of a pH representation. Specifically, the outer-loop regulating a state to be equal to another state is the root to the problem. Obtaining a valid pH representation of the incremental model in further research could contribute to the pursuit of a scalable stability certificate for the interconnected DC MG. However, this process is not straightforward as it is not clear how to obtain a Lyapunov candidate.

Lastly, the thesis obtained a stability certificate for the fast dynamics of the modified controller proposed in chapter 5. However, a comprehensive proof based on singular perturbation theory that could potentially guarantee stability under all circumstances is left for further work.

Bibliography

[1] Babak Abdolmaleki and Gilbert Bergna-Diaz. 'Distributed Control and Optimization of DC Microgrids: A Port-Hamiltonian Approach'. In: *IEEE Access* 10 (2022), pp. 64222–64233. DOI: 10.1109/ACCESS.2022.3183209.

[2] Babak Abdolmaleki and Gilbert Bergna-Diaz. 'A Nonlinear Control Framework for Optimal Load-sharing and Voltage Containment in DC Networks'. In: *IEEE Transactions on Power Systems* (2022), pp. 1–4. DOI: 10.1109/TPWRS.2022.3216162.

[3] Cornelia Skaga. *Energy Control of Complex Cyber-Physical Microgrids: Robustness against Cyber Attacks*. Master's thesis. Department of Electric Power Engineering, NTNU – Norwegian University of Science and Technology, June 2022.

[4] National Oceanic and Atmospheric Administration. *Greenhouse gases continued to increase rapidly in 2022*. 2023. URL: https://www.noaa.gov/news-release/greenhouse-gases-continued-to-increase-rapidly-in-2022#:~:text=Atmospheric%5C%20CO2%5C%20is%5C%20now,more%5C%20had%5C%20never%5C%20been%5C%20recorded.

[5] Klima- og miljødepartementet. *Meld. St. 21*. 2023. URL: https://www.regjeringen.no/no/dokumenter/meld-st-21-2011-2012/id679374/?ch=2#:~:text=Etter%5C%20den%5C%20industrielle%5C20revolusjonen%5C%20har,niv%C3%A5et%5C%20p%C3%A5%5C%20en%5C%20million%5C%20%C3%A5r.

[6] United Nations Climate Change. *The Paris Agreement. What is the Paris Agreement?* 2023. URL: https://unfccc.int/process-and-meetings/the-paris-agreement.

[7] United Nations Climate Change. *Nationally Determined Contributions (NDCs). The Paris Agreement and NDCs*. 2023. URL: https://unfccc.int/process-and-meetings/the-paris-agreement/nationally-determined-contributions-ndcs.

[8] International Energy Agency. *Greenhouse Gas Emissions from Energy Data Explorer*. 2021. URL: https://www.iea.org/data-and-statistics/data-tools/greenhouse-gas-emissions-from-energy-data-explorer.

[9] International Energy Agency. *Net Zero by 2050. A Roadmap for the Global Energy Sector*. 2021. URL: https://www.iea.org/reports/net-zero-by-2050.

[10] International Energy Agency. *Unlocking the Potential of Distributed Energy Resources*. 2022. URL: https://www.iea.org/reports/unlocking-the-potential-of-distributed-energy-resources.

[11] IEEE. 'IEEE Draft Recommended Practice for Electrical System Design Techniques to Improve Electrical Safety'. In: *P1814/D14, January 2018* (2018), pp. 1–122. DOI: 10.1109/IEEESTD.2018.8295083.

[12] Adam Hirsch, Yael Parag and Josep Guerrero. 'Microgrids: A review of technologies, key drivers, and outstanding issues'. In: *Renewable and Sustainable Energy Reviews* 90 (2018), pp. 402–411. ISSN: 1364-0321. DOI: https://doi.org/10.1016/j.rser.2018.03.040. URL: https://www.sciencedirect.com/science/article/pii/S136403211830128X.

[13] Jackson John Justo et al. 'AC-microgrids versus DC-microgrids with distributed energy resources: A review'. In: *Renewable and Sustainable Energy Reviews* 24 (2013), pp. 387–405. ISSN: 1364-0321. DOI: https://doi.org/10.1016/j.rser.2013.03.067. URL: https://www.sciencedirect.com/science/article/pii/S1364032113002268.

[14] Luis Eduardo Zubieta. 'Are Microgrids the Future of Energy?: DC Microgrids from Concept to Demonstration to Deployment'. In: *IEEE Electrification Magazine* 4.2 (2016), pp. 37–44. DOI: 10.1109/MELE.2016.2544238.

[15] Yang Han et al. 'Review of Power Sharing, Voltage Restoration and Stabilization Techniques in Hierarchical Controlled DC Microgrids'. In: *IEEE Access* 7 (2019), pp. 149202–149223. DOI: 10.1109/ACCESS.2019.2946706.

[16] Duy-Hung Dam and Hong-Hee Lee. 'A Power Distributed Control Method for Proportional Load Power Sharing and Bus Voltage Restoration in a DC Microgrid'. In: *IEEE Transactions on Industry Applications* 54.4 (2018), pp. 3616–3625. DOI: 10.1109/TIA.2018.2815661.

[17] Tung-Lam Nguyen et al. 'Multi-Agent System with Plug and Play Feature for Distributed Secondary Control in Microgrid—Controller and Power Hardware-in-the-Loop Implementation'. In: *Energies* 11.12 (2018). ISSN: 1996-1073. DOI: 10.3390/en11123253. URL: https://www.mdpi.com/1996-1073/11/12/3253.

[18] Florian Dörfler, John W. Simpson-Porco and Francesco Bullo. 'Breaking the Hierarchy: Distributed Control and Economic Optimality in Microgrids'. In: *IEEE Transactions on Control of Network Systems* 3.3 (2016), pp. 241–253. DOI: 10.1109/TCNS.2015.2459391.

[19] Yinliang Xu et al. 'Optimal Distributed Control for Secondary Frequency and Voltage Regulation in an Islanded Microgrid'. In: *IEEE Transactions on Industrial Informatics* 15.1 (2019), pp. 225–235. DOI: 10.1109/TII.2018.2795584.

[20] Arshad Nawaz, Jing Wu and Chengnian Long. 'Mitigation of circulating currents for proportional current sharing and voltage stability of isolated DC microgrid'. In: *Electric Power Systems Research* 180 (2020), p. 106123. ISSN: 0378-7796. DOI: https://doi.org/10.1016/j.epsr.2019.106123. URL: https://www.sciencedirect.com/science/article/pii/S0378779619304420.

[21] Sebastian Trip et al. 'Distributed Averaging Control for Voltage Regulation and Current Sharing in DC Microgrids'. In: *IEEE Control Systems Letters* 3.1 (2019), pp. 174–179. DOI: 10.1109/LCSYS.2018.2857559.

[22] Nabil Mohammed and Mihai Ciobotaru. 'Fast and accurate grid impedance estimation approach for stability analysis of grid-connected inverters'. In: *Electric Power Systems Research* 207 (2022), p. 107831. ISSN: 0378-7796. DOI: https://doi.org/10.1016/j.epsr.2022.107831. URL: https://www.sciencedirect.com/science/article/pii/S037877962200061X.

[23] Pulkit Nahata et al. 'A passivity-based approach to voltage stabilization in DC microgrids with ZIP loads'. In: *Automatica* 113 (2020), p. 108770. ISSN: 0005-1098. DOI: https://doi.org/10.1016/j.automatica.2019.108770. URL: https://www.sciencedirect.com/science/article/pii/S0005109819306338.

[24] Kamilla B. Folgerø. *Networked Control of Microgrids: Robustness Against Cyberattacks*. Specialisation Project in TET4510. Department of Electric Power Engineering, NTNU – Norwegian University of Science and Technology, Dec. 2022.

[25] Iván Patrao et al. 'Microgrid architectures for low voltage distributed generation'. In: *Renewable and Sustainable Energy Reviews* 43 (2015), pp. 415–424. ISSN: 1364-0321. DOI: https://doi.org/10.1016/j.rser.2014.11.054. URL: https://www.sciencedirect.com/science/article/pii/S1364032114009939.

[26] M. Iswarya et al. 'A perspective on graph theory-based stability analysis of impulsive stochastic recurrent neural networks with time-varying delays'. In: (2019). DOI: 10.1186/s13662-019-2443-3.

[27] Francesco Bullo. 'Lectures on Network Systems'. In: *https://ucsb.app.box.com/v/LecturesNetworkSystems*. 2022, p. 151. URL: %5Cnewline%20https://ucsb.app.box.com/v/LecturesNetworkSystems.

[28] M. Pipattanasomporn, H. Feroze and S. Rahman. 'Multi-agent systems in a distributed smart grid: Design and implementation'. In: *2009 IEEE/PES Power Systems Conference and Exposition*. 2009, pp. 1–8. DOI: 10.1109/PSCE.2009.4840087.

[29] Daniele Ferreira et al. 'Overview of Consensus Protocol and Its Application to Microgrid Control'. In: *Energies* 15.22 (2022). ISSN: 1996-1073. URL: https://www.mdpi.com/1996-1073/15/22/8536.

[30] J. Romberg. 'Notes on The Karush-Kuhn-Tucker (KKT) conditions'. In: (2017). URL: https://www.math.cuhk.edu.hk/course_builder/2122/math4230/More%5C%20on%5C%20KKT.pdf.

[31] Antonio Filieri et al. 'Software Engineering Meets Control Theory'. In: *2015 IEEE/ACM 10th International Symposium on Software Engineering for Adaptive and Self-Managing Systems*. 2015, pp. 71–82. DOI: 10.1109/SEAMS.2015.12.

[32] Randy A. Freeman, Peng Yang and Kevin M. Lynch. 'Stability and Convergence Properties of Dynamic Average Consensus Estimators'. In: *Proceedings of the 45th IEEE Conference on Decision and Control*. 2006, pp. 338–343. DOI: 10.1109/CDC.2006.377078.

[33] Didier Marx et al. 'Large Signal Stability Analysis Tools in DC Power Systems With Constant Power Loads and Variable Power Loads—A Review'. In: *IEEE Transactions on Power Electronics* 27.4 (2012), pp. 1773–1787. DOI: 10.1109/TPEL.2011.2170202.

[34] Arjan van der Schaft and Dimitri Jeltsema. *Port-Hamiltonian Systems Theory: An Introductory Overview*. 2014.

[35] Karim Cherifi, Hannes Gernandt and Dorothea Hinsen. *The difference between port-Hamiltonian, passive and positive real descriptor systems*. 2022. DOI: 10.48550/ARXIV.2204.04990. URL: https://arxiv.org/abs/2204.04990.

[36] H.K. Khalil. *Nonlinear Control*. Pearson Education Limited, 2014. ISBN: 9781292060507.

[37] K.J Åström and R. M Murray. *Feedback Systems - An Introduction for Scientists and Engineers*. Princeton University Press, 2012. ISBN: 9780691135762.

[38] Richard Perryman, Joshua A. Taylor and Bryan Karney. 'Port-Hamiltonian based control of water distribution networks'. In: *Systems & Control Letters* 170 (2022), p. 105402. ISSN: 0167-6911. DOI: https://doi.org/10.1016/j.sysconle.2022.105402. URL: https://www.sciencedirect.com/science/article/pii/S0167691122001797.

[39] Babak Abdolmaleki, John W. Simpson-Porco and Gilbert Bergna-Diaz. *Distributed Optimization for Reactive Power Sharing and Stability of Inverter-Based Resources Under Voltage Limits*. 2023. arXiv: 2302.09241 [eess.SY].

[40] Pietro Lorenzetti and George Weiss. 'Saturating PI Control of Stable Nonlinear Systems Using Singular Perturbations'. In: *IEEE Transactions on Automatic Control* 68.2 (2023), pp. 867–882. DOI: 10.1109/TAC.2022.3147167.

[41] H.K. Khalil. *Nonlinear Systems*. Pearson Education Limited, 2014. ISBN: 9781784490133.

[42] D. Spanos, R. Olfati-Saber and R. Murray. 'Dynamic Consensus for Mobile Networks'. In: 2005. URL: http://users.cms.caltech.edu/~murray/preprints/som05-ifac.pdf.

Appendices

A.1 The Laplacian Matrix and Consensus

The following section is reproduced from the associated specialization project [24]. It explains the Laplacian matrix used throughout the master's thesis and its important properties that can be taken advantage of in control theory. The Laplacian of a graph is a central object in the study of distributed consensus dynamics [42]. A system can have consensus if every agent in the system has agreed upon a common value [29]. In distributed networks, the system has consensus if every pair of neighbors i and j converge to the same value. This gives the following relation between the local states at each agent: $x_i = x_j$, i.e., as in (A.1.1).

$$\lim_{t\to\infty} (x_i(t) - x_j(t)) = 0 \tag{A.1.1}$$

The Laplacian consensus dynamics of the ith DG, in a system, is given as in (A.1.2), where a_{ij} represent the elements in the adjacency matrix [42].

$$\dot{x}_i = -\sum_{j\in N_i} a_{ij} \left(x_i(t) - x_j(t)\right) \tag{A.1.2}$$

This implies that the DGs only need information about their neighbors to update their state, i.e., following a distributed topology. The neighbors of the ith DG are given in the set N_i. The expression (A.1.2) can be expressed as below in (A.1.3).

$$\dot{x}_i = -\left(\sum_{j\in N_i} a_{ij}x_i(t) - \sum_{j\in N_i} a_{ij}x_j(t)\right) \tag{A.1.3}$$

When (A.1.3) is written in matrix notation, the following relation in (A.1.4) is obtained.

$$\dot{\mathbf{x}} = -\left(\boldsymbol{\mathcal{D}} - \boldsymbol{\mathcal{A}}\right)\mathbf{x}(t) = -\boldsymbol{\mathcal{L}}\mathbf{x}(t) \tag{A.1.4}$$

Based on an undirected graph like $\mathcal{M}_c$, the Laplacian matrix above becomes a symmetric positive semi-definite matrix. This also implies that the Laplacian consensus dynamics are stable and must converge in steady-state [42]. Therefore, when an undirected graph is related to the system modeling, the sum of all DG's states will be unchanged over time, as pointed out below [29].

$$
\begin{aligned}
&\frac{d}{dt}\left(\sum_{i=1}^{n} x_i(t)\right) = 0 \\
&\Rightarrow \sum_{i=1}^{n} x_i(t) = \text{constant} \\
&\Rightarrow -\sum_{j\in N_i} a_{ij}\left(x_i(t) - x_j(t)\right) = 0 \\
&\Rightarrow x_i(t) = x_j(t)
\end{aligned}
$$

The above relation implies that the dynamics of the Laplacian will bring any initial condition to a consensus and maintain the sum of the initial states, $x_i(0)$ [42]. Further, the state of each DG converges to the same average value as below in (A.1.6) [29].

$$
\alpha = \frac{1}{n}\sum_{i=1}^{n} x_i(0) \tag{A.1.6}
$$

The sum of each row in the Laplacian matrix is equal to zero. Thus, the Laplacian matrix has the property of $\boldsymbol{\mathcal{L}\alpha} = 0$, where $\boldsymbol{\alpha} = [\alpha, \alpha, ..., \alpha]^\top$. This property is being taken advantage of in designing the controller because it is desirable that generators converge to a common consensus value to satisfy specific control objectives.

The sum of the elements in each column is also zero, giving the following relationship $\mathbf{1}^\top = \mathbf{0}$.[29] This property is used to illustrate that the set-points converge to the optimal shape in steady state.

A.2 Deriving the KKT Condition

This section contains reused material from the associated specialization project [24], where the optimal shape of $\bar{\lambda}_i$ was derived from the derivative of the Lagrangian function in (A.2.1) with respect to each set-point as in (A.2.2) following the KKT conditions. The derivations have the purpose of giving a thorough derivation of the complicated optimization problem presented in [2].

$$
\mathbb{L}(\bar{\lambda}_i, \bar{\zeta}_i) = \frac{1}{2}\sum_{i=1}^{n^{\mathcal{G}_i}} (\bar{\lambda}_i - \bar{I}^{\mathcal{G}}_{i,\text{pu}})^2 + \sum_{i=1}^{n^{\mathcal{G}_i}} \bar{\zeta}_i \underbrace{\sum_{j\in N_{\mathcal{G}_i}} a_{ij}(\bar{\lambda}_j - \bar{\lambda}_i)}_{\bar{z}_i} \tag{A.2.1}
$$

$$
\frac{\partial \mathbb{L}(\bar{\lambda}_i, \bar{\zeta}_i)}{\partial \bar{\lambda}_i} = 0 \tag{A.2.2}
$$

The derivatives of the two terms in (A.2.1) will be obtained separately as the latter term's derivative is complicated and needs further explanation. However, the derivative of the first term is rather straightforward and given in (A.2.3) below.

$$
\frac{\partial}{\partial \bar{\lambda}_i}\left(\frac{1}{2}\sum_{i=1}^{n^{\mathcal{G}_i}} (\bar{\lambda}_i - \bar{I}^{\mathcal{G}}_{i,\text{pu}})^2\right) = \bar{\lambda}_i - \bar{I}^{\mathcal{G}}_{i,\text{pu}} \tag{A.2.3}
$$

The derivative of the latter term in (A.2.1) is complicated and will be derived by applying it to the case-specific CP MG from Figure 2.4. Firstly, the $\bar{z}_i s$ for the system will be explained and

listed. The number of terms in $\bar{z}_i$ is determined by the number of neighbors that generator i has. As an example, DG1 only communicates with DG2 according to $N_{\mathcal{G}_1} = \{2\}$. Consequently, $\bar{z}_1$ only consists of one term. All $\bar{z}_i$s relevant for the case-specific CP MG are listed below in (A.2.4), where $\bar{z}_i$ from equation (A.2.1) is used in the calculations.

$$\bar{z}_i = \sum_{j \in N_{\mathcal{G}_i}} a_{ij}(\bar{\lambda}_j - \bar{\lambda}_i) \rightarrow \begin{cases} \bar{z}_1 & = a_{12}(\bar{\lambda}_2 - \bar{\lambda}_1) \\ \bar{z}_2 & = a_{21}(\bar{\lambda}_1 - \bar{\lambda}_2) + a_{23}(\bar{\lambda}_3 - \bar{\lambda}_2) + a_{24}(\bar{\lambda}_4 - \bar{\lambda}_2) \\ \bar{z}_3 & = a_{32}(\bar{\lambda}_2 - \bar{\lambda}_3) + a_{34}(\bar{\lambda}_4 - \bar{\lambda}_3) \\ \bar{z}_4 & = a_{42}(\bar{\lambda}_2 - \bar{\lambda}_4) + a_{43}(\bar{\lambda}_3 - \bar{\lambda}_4) \end{cases} \tag{A.2.4}$$

The following statements are valid when j is the neighbor of i and the communication graph is undirected, i.e, $a_{ij} = a_{ji}$:

- $\frac{\partial}{\partial \bar{\lambda}_i} \bar{z}_i = \sum\limits_{j \in N_{\mathcal{G}_i}} -a_{ij}$.
- $\frac{\partial}{\partial \bar{\lambda}_i} \bar{z}_j = \sum\limits_{j \in N_{\mathcal{G}_i}} a_{ij}, \forall\ j \neq i$
- $\sum\limits_{\substack{j=1 \\ j \neq i}}^{n^{\mathcal{G}_i}} = \sum\limits_{j \in N_{\mathcal{G}_i}}$

All the relevant $\bar{z}_i$s are identified and the derivative of the latter term in (A.2.1) is obtained in (A.2.5a). Using the statements above, the general shape of the derivative will result in expression (A.2.5d).

$$\frac{\partial}{\partial \bar{\lambda}_i} \left(\sum_{i=1}^{n^{\mathcal{G}_i}} \bar{\zeta}_i \bar{z}_i \right) = \frac{\partial}{\partial \bar{\lambda}_i} \left(\bar{\zeta}_1 \bar{z}_1 + \bar{\zeta}_2 \bar{z}_2 + \bar{\zeta}_3 \bar{z}_3 + \bar{\zeta}_4 \bar{z}_4 \right) \tag{A.2.5a}$$

$$= \frac{\partial}{\partial \bar{\lambda}_i} \left(\bar{\zeta}_i \bar{z}_i + \sum_{\substack{j=1 \\ j \neq i}}^{n^{\mathcal{G}_i}} \bar{\zeta}_j \bar{z}_j \right) = \frac{\partial}{\partial \bar{\lambda}_i} \left(\bar{\zeta}_i \bar{z}_i + \sum_{j \in N_{\mathcal{G}_i}} \bar{\zeta}_j \bar{z}_j \right) \tag{A.2.5b}$$

$$= \sum_{j \in N_{\mathcal{G}_i}} \bar{\zeta}_i(-a_{ij}) + \sum_{j \in N_{\mathcal{G}_i}} \bar{\zeta}_j a_{ij} \tag{A.2.5c}$$

$$= \sum_{j \in N_{\mathcal{G}_i}} a_{ij} \left(\bar{\zeta}_j - \bar{\zeta}_i \right) \tag{A.2.5d}$$

To prove the final shape of the derivative in (A.2.5d), the expression in (A.2.5a) will be derivated with respect to $\bar{\lambda}_i$ for all $i = 1, ..., n^{\mathcal{G}_i}$.

Generator 1, i = 1

In this case, i represents DG 1, and j represents the generators that are neighbors with DG 1. This DG has only one neighbor, thus $\bar{z}_j = \{\bar{z}_2\}$ and the derivative in (A.2.5a) with respect to $\bar{\lambda}_1$ gives only two summation terms as derived below. This is because $\bar{\lambda}_1$ is only present in $\bar{z}_1$ and $\bar{z}_2$.

$$\frac{\partial}{\partial \bar{\lambda}_1}\left(\sum_{i=1}^{n^{\mathcal{G}_i}} \bar{\zeta}_i \bar{z}_i\right) = \bar{\zeta}_1(-a_{12}) + \bar{\zeta}_2 a_{21} + 0 + 0$$

$$= \sum_{j \in N_{\mathcal{G}_1}} \bar{\zeta}_1(-a_{1j}) + \sum_{\substack{j=1 \\ j \neq i}}^{n^{\mathcal{G}_i}} \bar{\zeta}_j \sum_{j \in N_{\mathcal{G}_2}} a_{j1}$$

$$= \sum_{j \in N_{\mathcal{G}_1}} \bar{\zeta}_1(-a_{1j}) + \sum_{j \in N_{\mathcal{G}_1}} \bar{\zeta}_j a_{j1}$$

$$= \sum_{j \in N_{\mathcal{G}_1}} a_{1j}\left(\bar{\zeta}_j - \bar{\zeta}_1\right)$$

Generator 2, i = 2

In this case, i represents DG 2, and j represents the generators that are neighbors with DG 2. This DG has three neighbors, thus $\bar{z}_j = \{\bar{z}_1, \bar{z}_3, \bar{z}_4\}$ and the derivative in (A.2.5d) with respect to $\bar{\lambda}_2$ gives four summation terms, since $\bar{\lambda}_2$ is present in all $\bar{z}_i$s. This is because DG 2 is connected to all the DGs in the case-specific DC MG as shown in Figure 2.4.

$$\frac{\partial}{\partial \bar{\lambda}_2}\left(\sum_{i=1}^{n^{\mathcal{G}_i}} \bar{\zeta}_i \bar{z}_i\right) = \bar{\zeta}_1 a_{12} + \bar{\zeta}_2(-a_{21} - a_{23} - a_{24}) + \bar{\zeta}_3 a_{32} + \bar{\zeta}_4 a_{42}$$

$$= \sum_{j \in N_{\mathcal{G}_2}} \bar{\zeta}_2(-a_{2j}) + \sum_{\substack{j=1 \\ j \neq i}}^{n^{\mathcal{G}_i}} \bar{\zeta}_j \sum_{j \in N_{\mathcal{G}_2}} a_{j2}$$

$$= \sum_{j \in N_{\mathcal{G}_2}} \bar{\zeta}_2(-a_{2j}) + \sum_{j \in N_{\mathcal{G}_2}} \bar{\zeta}_j a_{j2}$$

$$= \sum_{j \in N_{\mathcal{G}_2}} a_{2j}\left(\bar{\zeta}_j - \bar{\zeta}_2\right)$$

Generator 3, i = 3

In this case, i represents DG 3, and j represents the generators that are neighbors with DG 3. This DG has two neighbors, thus $\bar{z}_j = \{\bar{z}_2, \bar{z}_4\}$ and the derivative in (A.2.5d) with respect to $\bar{\lambda}_3$ gives three summation terms. This is because $\bar{\lambda}_3$ is present in $\bar{z}_2$, $\bar{z}_3$ and $\bar{z}_4$.

$$\frac{\partial}{\partial \bar{\lambda}_3}\left(\sum_{i=1}^{n^{\mathcal{G}_i}} \bar{\zeta}_i \bar{z}_i\right) = \bar{\zeta}_2 a_{23} + \bar{\zeta}_3(-a_{32} - a_{34}) + \bar{\zeta}_4 a_{43} + 0$$

$$= \sum_{j \in N_{\mathcal{G}_3}} \bar{\zeta}_3(-a_{3j}) + \sum_{\substack{j=1 \\ j \neq i}}^{n^{\mathcal{G}_i}} \bar{\zeta}_j \sum_{j \in N_{\mathcal{G}_3}} a_{j3}$$

$$= \sum_{j \in N_{\mathcal{G}_3}} \bar{\zeta}_3(-a_{3j}) + \sum_{j \in N_{\mathcal{G}_3}} \bar{\zeta}_j a_{j3}$$

$$= \sum_{j \in N_{\mathcal{G}_3}} a_{3j}\left(\bar{\zeta}_j - \bar{\zeta}_3\right)$$

Generator 4, i = 4

In this case, i represents DG 4, and j represents the generators that are neighbors with DG 4.

This DG has two neighbors, thus $\bar{z}_j = \{\bar{z}_2, \bar{z}_3\}$ and the derivative in (A.2.5d) with respect to $\bar{\lambda}_4$ gives three summation terms. This is because $\bar{\lambda}_4$ is present in $\bar{z}_2$, $\bar{z}_3$ and $\bar{z}_4$.

$$\begin{aligned}\frac{\partial}{\partial \bar{\lambda}_4}\left(\sum_{i=1}^{n^{\mathcal{G}_i}} \bar{\zeta}_i \bar{z}_i\right) &= \bar{\zeta}_2 a_{24} + \bar{\zeta}_3 a_{34} + \bar{\zeta}_4(-a_{42} - a_{43}) + 0 \\ &= \sum_{j \in N_{\mathcal{G}_4}} \bar{\zeta}_4(-a_{4j}) + \sum_{\substack{j=1 \\ j \neq i}}^{n^{\mathcal{G}_i}} \bar{\zeta}_j \sum_{j \in N_{\mathcal{G}_4}} a_{j4} \\ &= \sum_{j \in N_{\mathcal{G}_4}} \bar{\zeta}_4(-a_{4j}) + \sum_{j \in N_{\mathcal{G}_4}} \bar{\zeta}_j a_{j4} \\ &= \sum_{j \in N_{\mathcal{G}_4}} a_{4j}\left(\bar{\zeta}_j - \bar{\zeta}_4\right)\end{aligned}$$

From the above derivations, it is clear that the general relationship in (A.2.5d) holds. This relationship, together with the derivative of the first term as given in (A.2.3), makes it possible to solve (A.2.2) as derived in (A.2.10).

$$\frac{\partial \mathbb{L}(\bar{\lambda}_i, \bar{\zeta}_i)}{\partial \bar{\lambda}_i} = \bar{\lambda}_i - \bar{I}^{\mathcal{G}}_{i,\mathrm{pu}} + \sum_{j \in N_{\mathcal{G}_i}} a_{ij}\left(\bar{\zeta}_j - \bar{\zeta}_i\right) = 0 \tag{A.2.10a}$$

$$\bar{\lambda}_i = \bar{I}^{\mathcal{G}}_{i,\mathrm{pu}} + \sum_{j \in N_{\mathcal{G}_i}} a_{ij}\left(\bar{\zeta}_i - \bar{\zeta}_j\right) \tag{A.2.10b}$$

The optimal shape for each $\bar{\lambda}_i$ in the case-specific CP MG is given below in (A.2.11).

$$\bar{\lambda}_i = \bar{I}^{\mathcal{G}}_{i,\mathrm{pu}} + \sum_{j \in N_{\mathcal{G}_i}} a_{ij}\left(\bar{\zeta}_i - \bar{\zeta}_j\right) \rightarrow \begin{cases} \bar{\lambda}_1 &= \bar{I}^{\mathcal{G}}_{1,\mathrm{pu}} + a_{12}(\bar{\zeta}_1 - \bar{\zeta}_2) \\ \bar{\lambda}_2 &= \bar{I}^{\mathcal{G}}_{2,\mathrm{pu}} + a_{21}(\bar{\zeta}_2 - \bar{\zeta}_1) + a_{23}(\bar{\zeta}_2 - \bar{\zeta}_3) + a_{24}(\bar{\zeta}_2 - \bar{\zeta}_4) \\ \bar{\lambda}_3 &= \bar{I}^{\mathcal{G}}_{3,\mathrm{pu}} + a_{32}(\bar{\zeta}_3 - \bar{\zeta}_2) + a_{34}(\bar{\zeta}_3 - \bar{\zeta}_4) \\ \bar{\lambda}_4 &= \bar{I}^{\mathcal{G}}_{4,\mathrm{pu}} + a_{42}(\bar{\zeta}_4 - \bar{\zeta}_2) + a_{43}(\bar{\zeta}_4 - \bar{\zeta}_3) \end{cases} \tag{A.2.11}$$

A.3 Energy Modeling of the Cyber-Physical DC Micro Grid

This section is reproduced from the associated specialization project [24] and aims to illustrate the challenge that occurred in the pH representation of the CP DC MG with the regulator state and both layers connected.

As a first step, the controller is simplified by disregarding the non-linear hyperbolic tangent function, as shown in equation (A.3.1a). In addition, the leakage function, which is only activated when the voltage needs to saturate, will also be ignored. This simplification will allow us to avoid any complications caused by the non-linearity of the hyperbolic tangent function.

$$u_{i,p} = v_i \tag{A.3.1a}$$

$$\tau \dot{v}_i = V_{\mathrm{nom}}(\lambda_i - I^{\mathcal{G}}_{i,\mathrm{pu}}) \tag{A.3.1b}$$

The physical layer and cyber layer were represented in matrix notation in (4.2.3) and (4.3.2), respectively. Combined with the ODE for the regulator state, v_i, the total cyber-physical MG in matrix notation can be obtained with these two equations as in (A.3.2).

$$\underbrace{\begin{bmatrix} \boldsymbol{L}_*^{\mathcal{G}}\dot{\boldsymbol{I}}_{\text{pu}}^{\mathcal{G}} \\ \boldsymbol{L}_*^{\mathcal{E}}\dot{\boldsymbol{I}}^{\mathcal{E}} \\ \boldsymbol{C}_*^{\mathcal{N}}\dot{\boldsymbol{V}}^{\mathcal{N}} \\ \dot{\boldsymbol{\zeta}} \\ \dot{\boldsymbol{\lambda}} \\ \boldsymbol{\tau}\dot{\boldsymbol{v}} \end{bmatrix}}_{\dot{\boldsymbol{x}}_T} = \underbrace{\begin{bmatrix} -\boldsymbol{R}_*^{\mathcal{G}} & \mathbf{0} & -\boldsymbol{\mathcal{B}}^{\mathcal{G}\top} & \mathbf{0} & \mathbf{0} & \boldsymbol{\mathcal{I}}^{\mathcal{G}} \\ \mathbf{0} & -\boldsymbol{R}_*^{\mathcal{E}} & -\boldsymbol{\mathcal{B}}_*^{\mathcal{E}\top} & \mathbf{0} & \mathbf{0} & \mathbf{0} \\ \boldsymbol{\mathcal{B}}^{\mathcal{G}} & \boldsymbol{\mathcal{B}}_*^{\mathcal{E}} & -\boldsymbol{G}_{*,\text{cte}}^{\mathcal{N}} & \mathbf{0} & \mathbf{0} & \mathbf{0} \\ \mathbf{0} & \mathbf{0} & \mathbf{0} & \mathbf{0} & -\boldsymbol{\mathcal{L}} & \mathbf{0} \\ \boldsymbol{K}_y & \mathbf{0} & \mathbf{0} & \boldsymbol{\mathcal{L}} & -\left(\boldsymbol{K}_y + \boldsymbol{\mathcal{L}}\boldsymbol{K}_P\right)\boldsymbol{K}_I^{-1} & \mathbf{0} \\ -\boldsymbol{\mathcal{I}}^{\mathcal{G}}V_{\text{nom}} & \mathbf{0} & \mathbf{0} & \mathbf{0} & V_{\text{nom}}\boldsymbol{K}_I^{-1} & \mathbf{0} \end{bmatrix}}_{\boldsymbol{F}_T} \underbrace{\begin{bmatrix} \boldsymbol{I}_{\text{pu}}^{\mathcal{G}} \\ \boldsymbol{I}^{\mathcal{E}} \\ \boldsymbol{V}^{\mathcal{N}} \\ \boldsymbol{K}_y\boldsymbol{\zeta} \\ \boldsymbol{K}_I\boldsymbol{\lambda} \\ \boldsymbol{v} \end{bmatrix}}_{\boldsymbol{\nabla} H_T(\boldsymbol{x}_T)} + \underbrace{\begin{bmatrix} \mathbf{1}V_{\text{nom}} \\ \mathbf{0} \\ -\boldsymbol{I}_{*,\text{cte}} \\ \mathbf{0} \\ \mathbf{0} \\ \mathbf{0} \end{bmatrix}}_{\boldsymbol{E}_T} \tag{A.3.2}$$

From the correlation, $\boldsymbol{\nabla} H_T(\boldsymbol{x}_T) = \boldsymbol{Q}_T\boldsymbol{x}_T$, it can be observed that $\boldsymbol{Q}_T$ is a symmetric positive matrix that consists of the inverse of inductances, capacitances, a time constant, and positive gains. This implies that $\boldsymbol{Q}_T$ has desirable properties for use in the analysis of the system.

$$\boldsymbol{Q}_T := \begin{bmatrix} (\boldsymbol{L}_*^{\mathcal{G}})^{-1} & \mathbf{0} & \mathbf{0} & \mathbf{0} & \mathbf{0} & \mathbf{0} \\ \mathbf{0} & (\boldsymbol{L}_*^{\mathcal{E}})^{-1} & \mathbf{0} & \mathbf{0} & \mathbf{0} & \mathbf{0} \\ \mathbf{0} & \mathbf{0} & (\boldsymbol{C}_*^{\mathcal{N}})^{-1} & \mathbf{0} & \mathbf{0} & \mathbf{0} \\ \mathbf{0} & \mathbf{0} & \mathbf{0} & \boldsymbol{K}_y & \mathbf{0} & \mathbf{0} \\ \mathbf{0} & \mathbf{0} & \mathbf{0} & \mathbf{0} & \boldsymbol{K}_I & \mathbf{0} \\ \mathbf{0} & \mathbf{0} & \mathbf{0} & \mathbf{0} & \mathbf{0} & (\boldsymbol{\tau})^{-1} \end{bmatrix}$$

However, $\mathbf{F}_T$ from (A.3.2) is not a symmetrical positive semi-definite matrix. Consequently, a pH representation of the CP DC MG is not obtained.

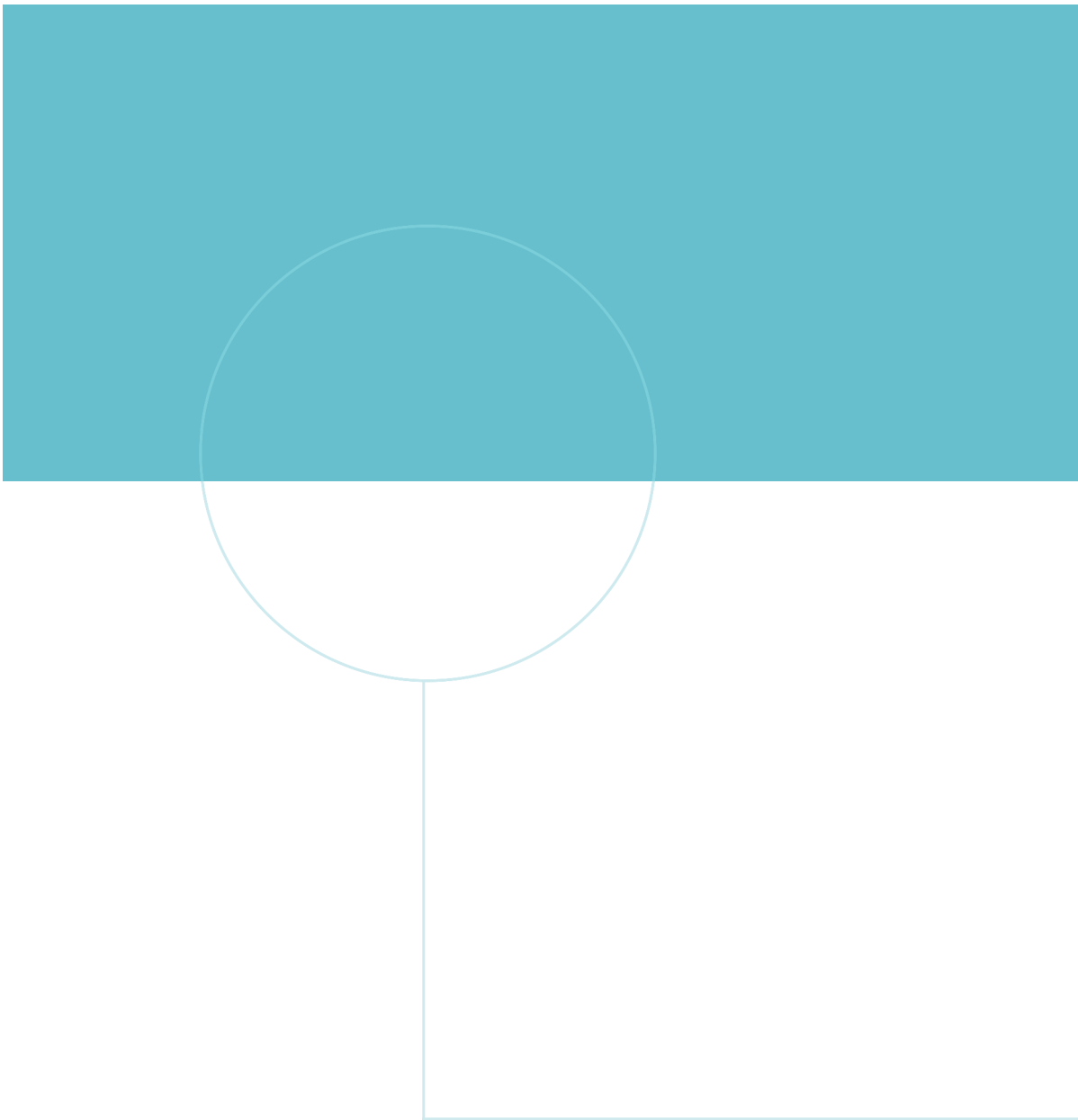

NTNU

Norwegian University of
Science and Technology